

---

# **Magnesium alloys for temporary implant applications: stress corrosion cracking and biocompatible coating**

A thesis submitted to Monash University as fulfilment for the degree of

Doctor of Philosophy

**2013**

**Lokesh Kumar Choudhary**

Supervised by:

Prof. R. K. Singh Raman

**Department of Mechanical and Aerospace Engineering**

Monash University, Clayton, Australia

---

**Notice 1**

Under the Copyright Act 1968, this thesis must be used only under the normal conditions of scholarly fair dealing. In particular no results or conclusions should be extracted from it, nor should it be copied or closely paraphrased in whole or in part without the written consent of the author. Proper written acknowledgement should be made for any assistance obtained from this thesis.



---

## *Declaration Statement*

---

This thesis or any its portions thereof, does not contain material that has been submitted or accepted for the award of another degree, diploma or qualification of this or any other university or institution of learning.

To the best of the candidate's knowledge and belief, this thesis does not contain any material that has been previously published or written by another person except where full and due reference is made to the original author(s) within the text, figures or tables.

Lokesh K. Choudhary



*Dedicated to my family*



---

## *Acknowledgements*

---

I am extremely thankful to my supervisor, Prof. R. K. Singh Raman, for providing me with an opportunity to work in his research group and offering constant guidance, support and encouragement during my PhD. I also take this opportunity to express my gratitude and acknowledge his trust, in my ability to perform this research and for involving me in several other research projects, during my candidature.

I would like to thank Prof. Peter J. Uggowitzer, Laboratory of Materials Physics and Technology, ETH Zurich, Switzerland for generously providing me the necessary alloys to carry out my experimental work effectively. The support and help of Prof. J. F. Nie, Department of Materials Engineering, Monash University, Australia and Dr. Mainak Majumder, Department of Mechanical & Aerospace Engineering, Monash University, Australia during various stages of my research are also highly appreciated.

I am thankful to the Department of Mechanical and Aerospace Engineering for providing me all the research facilities, infrastructure and scholarships. I greatly appreciate the help of cheerful and supportive staff, specifically, Helen Frost, Nicole Bodestaff and Stelios Kostanidinis in administration, and Hugh Venables, Nat Deroose, Narendra Babu, Santhosh Babu and Alex Bain in the workshop. I am grateful to the Department of Chemical Engineering, Monash University for giving me access to the Corrosion Laboratory for carrying out experimental work. I would also like to express my gratitude towards knowledgeable and kind staff at the Monash Centre for Electron Microscopy (MCEM) for helping me with sample preparation and providing the necessary infrastructure to perform electron microscopy.





A special thanks to Mahesh for always being there during all the tough times endured throughout my PhD. I am sincerely thankful to Parama for the cheerful time and constant help. The coating work of this project would not have been possible without her support. I was also lucky to have wonderful group members/alumni who provided a very friendly and cordial atmosphere in the lab. I would like to thank group alumni Rajeev, Abhishek and Sarvesh for not only the numerous thought provoking discussions and helpful suggestions throughout my PhD but also the fun times we had outside the university. I would also like to thank my colleagues including Saad-Al-Saadi, Dr. Muhammed Khalissi, Sachie Welikala, Nilesh Raykar, Bharat Padekar, Swati, Amrita Majumder, Abhishek Tiwari, Sajjad Jafari and Joelle Hofstetter for creating a lively atmosphere and having fruitful discussions at the workplace.

During the course of my PhD, I was fortunate to supervise a great number of undergraduate students. I enjoyed working with them very much. I am very grateful for the valuable contributions of Robert Goldwasser, Jeremy Szmerling, Marc Bloom, Aaron Freedman, Kirilly Wagstaff, Amanda Gorman, Richard Arthur and Christiaan Orozco.

I wholeheartedly thank my friends Rashmi, Varun, Rahul, Debadi, Ali, Vats, John, Jamie, Pranav and others who I may have missed, for not only keeping me entertained throughout my stay in Australia but also providing support and encouragement at times of need. Their presence around greatly helped me on the long and hard road to my PhD. Special thanks to my wingmates for always providing constant support and fun.

Finally, I am thankful to the most important people in my life, my family and most importantly my parents and brother, for always being there. I will never be able to repay their unconditional love and care.

February 2013



---

## *Abstract*

---

Magnesium (Mg) alloys have emerged as potential candidate materials for construction of biodegradable temporary implant devices particularly due to advantages of favourable mechanical properties, biodegradability and biocompatibility. However, the poor corrosion resistance of Mg alloys in the physiological environment presents a major challenge to their use as biodegradable temporary implants. Furthermore, complex interaction of mechanical loading and aggressive physiological environment may often pose a considerable risk of premature failure of implant devices before expected service life due to the phenomenon of environmentally assisted cracking, i.e. stress corrosion cracking (SCC) and corrosion fatigue. Therefore, it is essential to evaluate the mechanical integrity of Mg alloys before they can be put to actual use. Accordingly, this study has attempted to establish a mechanistic understanding of SCC of one of the most common magnesium alloys, AZ91D and a few novel aluminium-free magnesium alloys, ZX50, WZ21 and WE43 in the simulated body environment. The SCC susceptibility of the alloys in a simulated human body fluid was established by slow strain rate tensile (SSRT) testing using smooth specimens under different environmental conditions that could mechanistically confirm the occurrence of SCC. However, to assess the life of the implant devices that often possess fine micro-cracks, SCC susceptibility of notched specimens of AZ91D was investigated by circumferential notch tensile (CNT) testing to generate important design data (i.e. threshold stress intensity for SCC ( $K_{ISCC}$ ) and SCC crack growth rate). The SCC susceptibility of the alloys was confirmed by fractographic features of transgranular and/or intergranular cracking. This study also investigated the role of novel biocompatible graphene-calcium carbonate coating in improving the corrosion/SCC resistance of AZ91D alloy as well as in promoting the in-situ biomineralization of bone apatite in the physiological environment.



---

# Contents

---

<b>1. Introduction</b>	1
<b>2. Literature review</b>	5
2.1 Implant devices	5
2.2 Magnesium alloys as biodegradable temporary implant	9
2.3 Corrosion of Mg/Mg-based alloys: in general	14
2.3.1 Thermodynamics of corrosion of magnesium	14
2.3.2 Stability and protectiveness of surface film	16
2.3.3 Electrochemical processes	17
2.4 Corrosion of Mg alloys in the physiological environment	21
2.4.1 Galvanic corrosion	21
2.4.2 Localized/pitting corrosion	24
2.4.3 Stress corrosion cracking (SCC)	26
2.5 Phenomenology of SCC of magnesium alloys	27
2.5.1 Influence of alloying elements	27
2.5.2 Characterization of SCC using different techniques	29
2.5.3 Mechanism of SCC in Mg alloys	36
2.6 SCC of magnesium alloys: in biomaterials perspective	40
2.7 Prevention of SCC	42
2.8 Biocompatible coatings for corrosion/SCC resistance	43
2.8.1 Calcium-phosphate (Ca-P) coatings	44
2.8.2 Novel graphene-calcium carbonate coating	45
2.9 Research problems and objectives	47
<b>3. Experimental principles and procedures</b>	51
3.1 Test materials and environment	51
3.2 Stress corrosion cracking testing	54
3.2.1 Slow strain rate tensile (SSRT) testing	54
3.2.2 Circumferential notch tensile (CNT) testing	57



3.2.3	Fractography .....	64
3.3	Electrochemical characterizations .....	65
3.3.1	Potentiodynamic polarization .....	66
3.3.2	Electrochemical impedance spectroscopy (EIS).....	67
3.4	Post corrosion analysis .....	68
<b>4.</b>	<b>Stress corrosion cracking of AZ91D and Mg-Zn-Ca alloys under dynamic and static loadings in the physiological environment*</b> .....	<b>69</b>
4.1	Introduction .....	69
4.2	Experimental .....	70
4.3	Results and discussion.....	71
4.3.1	SCC of AZ91D under dynamic and static loadings.....	71
4.3.2	SCC of Mg - 3 wt. % Zn - 1 wt. % Ca (Mg <sub>3</sub> Zn <sub>1</sub> Ca) alloy.....	85
4.4	Conclusions .....	91
<b>5.</b>	<b>SCC of aluminium-free biodegradable magnesium alloys in the physiological environment</b> .....	<b>93</b>
5.1	Introduction .....	93
5.2	Experimental procedures.....	94
5.3	Results and discussion.....	95
5.3.1	Microstructure .....	95
5.3.2	Slow strain rate tensile (SSRT) testing .....	96
5.3.3	Fractography.....	99
5.3.4	Cathodic charging SSRT experiments.....	102
5.4	Conclusions .....	105
<b>6.</b>	<b>Novel graphene-calcium carbonate coating on AZ91D for resistance to localized corrosion and assisted degradation in mechanical property</b> .....	<b>107</b>
6.1	Introduction .....	107
6.2	Experimental .....	109
6.2.1	Material and test environment .....	109
6.2.2	Coating method.....	110
6.2.3	Coating characterization .....	111
6.2.4	Electrochemical testing.....	111





6.2.5	Post-corrosion analysis .....	111
6.2.6	Mechanical integrity of coated specimens.....	112
6.3	Results and discussion.....	112
6.3.1	Coating characterization .....	112
6.3.2	Electrochemical corrosion .....	116
6.3.3	Post-corrosion morphologies .....	123
6.3.4	Mechanical integrity of the coating .....	127
6.4	Conclusions .....	130
<b>7.</b>	<b>Overall conclusions and future work .....</b>	<b>133</b>
7.1	Overall conclusions.....	133
7.2	Future work .....	135
<b>8.</b>	<b>Bibliography .....</b>	<b>137</b>



---

## *List of Figures*

---

<b>Fig. 2.1.</b> Most common implant devices used in load bearing applications: (a) shoulder implant (b) knee prostheses (c) hip implant and (d) coronary stent [51].....	6
<b>Fig. 2.2.</b> Radiographs of hip implants showing changes in bone mass resulting from stress shielding around an implant: (a) bone loss at the proximal region, and (b) proximal bone loss (indicated in the circled regions at the edge of the prosthesis) is accompanied by increased bone deposition (indicated by the rectangle) in the distal region of the implant [40] .....	7
<b>Fig. 2.3.</b> Gradual loss of mechanical integrity of a temporary or biodegradable implant while the surrounding tissue is regaining mechanical strength [54].....	8
<b>Fig. 2.4.</b> Pourbaix diagram for Mg-water system at 25 °C [81].....	15
<b>Fig. 2.5.</b> The negative difference effect of Mg [64, 83] .....	18
<b>Fig. 2.6.</b> Effect of impurities and alloying elements on corrosion rate of Mg alloys in 3 wt % NaCl [6] .....	22
<b>Fig. 2.7.</b> Schematic representation of dual role of secondary phase of Mg alloys in corrosion [66].....	23
<b>Fig. 2.8.</b> Localized/pitting corrosion observed in different Mg alloys: (a) AZ61 [98], (b) AZ91 [16], and (c) Mg-Zn-Mn-Ca [99].....	25
<b>Fig. 2.9.</b> Stress vs. time to failure curves for various Mg-Al alloys in 40 g/L NaCl + 40 g/L Na <sub>2</sub> CrO <sub>4</sub> [67, 113] .....	28
<b>Fig. 2.10.</b> The effect of strain rate on the maximum nominal stress to fracture the specimens exposed to dry air or solutions containing 5 g l <sup>-1</sup> NaCl and various amounts of K <sub>2</sub> CrO <sub>4</sub> [113].....	31
<b>Fig. 2.11.</b> Typical plot of stress intensity factor vs. crack growth rate [125] .....	33
<b>Fig. 2.12.</b> Compact tension (CT) specimen (all dimensions are in inches) [101].....	34
<b>Fig. 2.13.</b> CNT specimen (all dimensions are in mm) [131] .....	35
<b>Fig. 2.14.</b> (a) Continuous crack propagation by dissolution following film rupture, and (b) cleavage type fracture ahead of embrittled zone [35] .....	36
<b>Fig. 2.15.</b> Fracture surfaces of ZE41: (a) in 0.5 wt. % NaCl - predominant intergranular and isolated transgranular (arrows) cracking, and (b) in distilled water - corrosion along the grain boundaries [18] .....	37
<b>Fig. 2.16.</b> Fracture surface for AZ91 specimen tested in distilled water under CERT conditions showing: (a) fine parallel markings (i) and (b) cleavage through $\beta$ particles [111] .....	38
<b>Fig. 3.1.</b> Geometry and dimensions of a SSRT specimen.....	54



<b>Fig. 3.2.</b> Schematic of the experimental set-up of SSRT rig.....	55
<b>Fig. 3.3.</b> Eccentricity of the final ligament after fatigue pre-cracking [124] .....	58
<b>Fig. 3.4.</b> (a) Profile projector and (b) eccentricity measurement of the final ligament [124] ...	59
<b>Fig. 3.5.</b> Determination of $K_{ISCC}$ of base metal and simulated heat affected zone (SHAZ) of grade 250 steel in 30 % caustic solution at 100 °C (asymptote to the time to failure axis in $K_I$ vs. time to failure plot gives the $K_{ISCC}$ value) .....	63
<b>Fig. 3.6.</b> Representative fractographs of (a) ductile failure due to mechanical overloading [36], (b) exclusive transgranular SCC [133], and (c) exclusive intergranular SCC [134] .....	65
<b>Fig. 3.7.</b> Schematic diagram of the experimental set-up for electrochemical experiments.....	66
<b>Fig. 4.1.</b> Microstructure (SEM back-scattered electron image) of AZ91D alloy.....	71
<b>Fig. 4.2.</b> Stress vs. strain curves for AZ91D in <i>m</i> -SBF solution and air at the strain rates: (a) $5.0 \times 10^{-7} \text{ s}^{-1}$ , (b) $3.1 \times 10^{-7} \text{ s}^{-1}$ and (c) $1.2 \times 10^{-7} \text{ s}^{-1}$ .....	72
<b>Fig. 4.3.</b> Representative fractographs of the AZ91D tested in air: (a) overall fracture surface, (b) the fracture surface showing dimples and occasional instances of brittle fracture.....	73
<b>Fig. 4.4.</b> Fractograph of the AZ91D specimen tested in <i>m</i> -SBF solution at 37 °C at the strain rate, $1.2 \times 10^{-7} \text{ s}^{-1}$ : (a) overall fracture surface (arrows indicate pitting at the circumference), (b) evidence of transgranular cracking (indicated by arrow) and (c) fractograph showing crack branching.....	74
<b>Fig. 4.5.</b> Fractograph of the AZ91D specimen tested in <i>m</i> -SBF solution at 37 °C at the strain rate, $5.0 \times 10^{-7} \text{ s}^{-1}$ : (a) overall fracture surface, (b) evidence of transgranular cracking.....	75
<b>Fig. 4.6.</b> Stress vs. time plots of AZ91D alloy tested at a strain rate of $2.2 \times 10^{-7} \text{ s}^{-1}$ : (a) in air, (b) in <i>m</i> -SBF solution, (c) pre-immersed in <i>m</i> -SBF for 28h and then immediately strained in air, and (d) continuously charged at 200 mV cathodic to open circuit potential in <i>m</i> -SBF during the test .....	76
<b>Fig. 4.7.</b> Fractograph of the specimen failed in <i>m</i> -SBF at a strain rate of $2.2 \times 10^{-7} \text{ s}^{-1}$ : (a) overall fracture surface, and (b) evidence of transgranular cracking .....	77
<b>Fig. 4.8.</b> SEM fractographs for the specimens: (a) immersed in <i>m</i> -SBF solution for 28 h and then strained in air, and (b) continuously cathodically charged and simultaneously pulled in <i>m</i> -SBF .....	78
<b>Fig. 4.9.</b> $K_I$ vs. $t_f$ plot of AZ91D alloy tested in <i>m</i> -SBF at 37 °C.....	79
<b>Fig. 4.10.</b> SEM fractographs of the specimen tested at $K_I = 6.8 \text{ MPa m}^{1/2}$ : (a) the overall fracture surface showing machined notch, fatigue pre-crack, SCC and mechanical failure zones, (b) fractograph showing fatigue pre-cracked and SCC zones (arrow indicating the crack propagation direction), and (c) mechanical failure zone showing the dimples .....	81



<b>Fig. 4.11.</b> SEM fractographs of the specimen tested at $K_I = 11.7 \text{ MPa m}^{1/2}$ : (a) the overall fracture surface showing machined notch, fatigue pre-crack, SCC and mechanical failure zones, (b) fatigue pre-cracked area, (c) fractograph showing transition from fatigue pre-cracked area to SCC zone (arrow indicating the crack propagation direction), and (d) mechanical failure zone showing the dimple formation.....	82
<b>Fig. 4.12.</b> Crack growth rate ( $da/dt$ ) vs. $K_I$ plot for AZ91D alloy in <i>m</i> -SBF at 37 °C .....	83
<b>Fig. 4.13.</b> Back scattered SEM microstructure of as-cast Mg3Zn1Ca alloy .....	85
<b>Fig. 4.14.</b> Stress vs. strain curves for the Mg3Zn1Ca alloy at the strain rate of: (a) $5.0 \times 10^{-7} \text{ s}^{-1}$ and (b) $1.2 \times 10^{-7} \text{ s}^{-1}$ .....	86
<b>Fig. 4.15.</b> Typical fractograph of the Mg3Zn1Ca alloy tested in air: (a) overall fracture surface and (b) fracture surface showing dimples as the primary feature.....	87
<b>Fig. 4.16.</b> Fractograph of the Mg3Zn1Ca alloy tested in <i>m</i> -SBF solution at 37 °C at the strain rate, $5.0 \times 10^{-7} \text{ s}^{-1}$ : (a) overall fracture surface, (b) fractograph showing transgranular cracking (arrows).....	88
<b>Fig. 4.17.</b> Fractograph of the Mg3Zn1Ca specimen tested in <i>m</i> -SBF solution at 37 °C at the strain rate $1.2 \times 10^{-7} \text{ s}^{-1}$ : (a) overall fracture surface, (b) fractograph showing transgranular cracking .....	88
<b>Fig. 4.18.</b> Stress vs. time plots of Mg3Zn1Ca alloy in: (a) air (b) <i>m</i> -SBF at open circuit potential (OCP) and (c) <i>m</i> -SBF under continuous cathodic charging at 200 mV (vs. SCE) negative to OCP at the strain rate of $2.2 \times 10^{-7} \text{ s}^{-1}$ .....	90
<b>Fig. 4.19.</b> Potentiodynamic polarization scans for the AZ91D and Mg3Zn1Ca alloy in the <i>m</i> -SBF solution at 37 °C.....	91
<b>Fig. 5.1.</b> Optical microstructure of as-received extruded magnesium alloys: (a) WZ21, (b) WE43 and (c) ZX50 .....	95
<b>Fig. 5.2.</b> Typical stress vs. strain plots in <i>m</i> -SBF and air, and under cathodic charging condition at the strain rate of $3.1 \times 10^{-7} \text{ s}^{-1}$ for alloys: (a) ZX50, (b) WZ21 and (c) WE43....	97
<b>Fig. 5.3.</b> Fractograph of WE43 specimen tested in air: (a) overall fracture surface, and (b) evidence of dimple formation.....	99
<b>Fig. 5.4.</b> Fractograph of the ZX50 alloy tested in the <i>m</i> -SBF solution at 37 °C: (a) overall fracture surface, (b) transgranular cracking in the SCC zone (dark arrow indicates crack propagation direction and bright arrows indicate areas of transgranular cracking) and (c) mechanical failure zone showing the dimples.....	100
<b>Fig. 5.5.</b> Fractograph of the WZ21 alloy tested in the <i>m</i> -SBF at 37 °C: (a) overall fracture surface, (b) evidence of transgranular cracking .....	101
<b>Fig. 5.6.</b> Fractograph of the WE43 alloy tested in the <i>m</i> -SBF at 37 °C: (a) overall fracture surface, (b) evidence of transgranular cracking and intergranular cracking .....	101
<b>Fig. 5.7.</b> Evolution of cathodic current density for WZ21 and WE43 during cathodic charging SSRT experiments.....	103





<b>Fig. 6.1.</b> Surface appearance of: (a) graphene-CaCO <sub>3</sub> coating and (b) only-CaCO <sub>3</sub> coating, on AZ91D.....	113
<b>Fig. 6.2.</b> (a) Overall SEM morphology of graphene-CaCO <sub>3</sub> coating, (b) a higher magnification SEM image showing the wrapping of vaterite microsphere by a graphene network, (c) cross sectional microscopy of graphene-CaCO <sub>3</sub> coating on AZ91D, and (d) SEM morphology of only- CaCO <sub>3</sub> (calcite) coating formed on AZ91D alloy in absence of the graphene network.....	114
<b>Fig. 6.3.</b> XRD scans of graphene-CaCO <sub>3</sub> and only-CaCO <sub>3</sub> coated specimens as compared to the AZ91D substrate .....	115
<b>Fig. 6.4.</b> (a) FTIR and (b) Raman spectra of graphene-CaCO <sub>3</sub> coated specimen .....	116
<b>Fig. 6.5.</b> Evolution of Nyquist plots for the graphene-CaCO <sub>3</sub> coated AZ91D in <i>m</i> -SBF for different durations .....	117
<b>Fig. 6.6.</b> (a) Bode impedance and (b) Bode phase plots for the graphene-CaCO <sub>3</sub> coated specimen after different immersion periods in <i>m</i> -SBF (immersion period was 2 h for bare AZ91D) .....	118
<b>Fig. 6.7.</b> The EEC used for simulation of experimental EIS data.....	119
<b>Fig. 6.8.</b> Curve fitting of experimental and simulated Bode plots for the graphene-CaCO <sub>3</sub> coated specimen after: (a) 2 h of immersion and (b) 120 h of immersion in <i>m</i> -SBF .	120
<b>Fig. 6.9.</b> Temporal evolution of different parameters for the graphene-CaCO <sub>3</sub> coated specimen after different immersion periods in <i>m</i> -SBF .....	121
<b>Fig. 6.10.</b> Evolution of (a) Nyquist plots and (b) Bode impedance plots for the only-CaCO <sub>3</sub> coated AZ91D after different immersion periods in <i>m</i> -SBF at 37 °C.....	122
<b>Fig. 6.11.</b> Potentiodynamic polarization scans for the graphene-CaCO <sub>3</sub> coated and bare specimens tested in <i>m</i> -SBF at 37 °C.....	123
<b>Fig. 6.12.</b> Macrographs of: (a) graphene-CaCO <sub>3</sub> coated specimen after 120 h of immersion in <i>m</i> -SBF, (b) only-CaCO <sub>3</sub> coated specimen after 72 h of immersion in <i>m</i> -SBF, and (c) bare AZ91D after 120 h of immersion.....	124
<b>Fig. 6.13.</b> Post-corrosion SEM morphology of: (a) graphene-CaCO <sub>3</sub> coated specimen after 24 h of immersion in <i>m</i> -SBF (b) graphene-CaCO <sub>3</sub> coated specimen after 120 h of immersion in <i>m</i> -SBF, and (c) only-CaCO <sub>3</sub> coated specimen after 72 h of immersion .....	125
<b>Fig. 6.14.</b> Evolution of polarization resistance of graphene-CaCO <sub>3</sub> and only-CaCO <sub>3</sub> coated specimens in comparison to the bare AZ91D in <i>m</i> -SBF solution after different immersion durations.....	126
<b>Fig. 6.15.</b> Macrographs of the gauge length of the coated and uncoated tensile specimens before and after immersion in <i>m</i> -SBF solution .....	128
<b>Fig. 6.16.</b> Ultimate tensile strengths for the uncoated specimen pulled in air, pre-immersed uncoated specimen pulled in air, pre-immersed coated specimen pulled in air .....	129



---

## *List of Tables*

---

Table 2.1: Mechanical properties of traditional and Mg alloys as compared to human bone [5].....	11
Table 2.2: Chemical potential of Mg and its components in various states at 25 °C [66, 80].....	15
Table 3.1: Chemical composition of AZ91D .....	51
Table 3.2: Nominal chemical composition (in wt. %) of Mg alloys used in this study.....	52
Table 3.3: Chemical composition of <i>m</i> -SBF solution compared with Hanks' solution, original SBF prepared by Kokubo and the inorganic portion of human blood plasma .....	53
Table 3.4: Different strain rates corresponding to the different motor speeds of the SSRT rig.....	55
Table 4.1: Experimentally determined $K_I$ data satisfying the validity requirement.....	80
Table 4.2: SCC susceptibility indices for AZ91D and Mg3Zn1Ca alloys.....	89
Table 5.1: Summary of mechanical properties of ZX50, WZ21 and WE43 alloys at the strain rate of $3.1 \times 10^{-7} \text{ s}^{-1}$ (duplicate tests).....	96
Table 5.2: $I_{\text{SCC}}$ indices for WZ21 and ZX50 alloys tested at a strain rate of $3.1 \times 10^{-7} \text{ s}^{-1}$ .....	98



# Chapter 1

## 1. Introduction

Traditional biomedical metallic materials such as stainless steels, cobalt-chromium alloys and titanium alloys have been widely used in implant applications because of their superior strength, ductility and corrosion resistance [1]. However, when these traditional alloys are used as temporary implant devices, e.g. plates, screws, cardiovascular stents and wires, a second surgery is required to remove the implants after tissues have healed. Besides the cost of this surgical procedure and inconvenience to patients, traditional alloys also cause local inflammation due to potential release of cytotoxic ions [2-4]. It would be very advantageous if a temporary implant material that degrades in the physiological environment after the completion of healing process could be identified, as this would obviate the need for the second surgical procedure [1, 5]. In this regard, magnesium (Mg) alloys have emerged as potential candidates for construction of biodegradable temporary implant devices because they can naturally degrade in the physiological environment due to their high electrochemical activity (standard reduction potential of Mg is  $-2.4$  V vs. standard hydrogen electrode (SHE) [6]). Unlike traditional implant materials, the mechanical properties of Mg are suitable for implant applications: they possess low density ( $\rho$ ) =  $1.74\text{--}2.0$  g cm<sup>-3</sup> and elastic modulus ( $E$ ) =  $41\text{--}45$  GPa, both of which are similar to these properties of human bones [1]. Hence the problem of stress shielding, which is caused due to the mismatch in the elastic modulus between natural bone and implant, can be mitigated if Mg and its alloys are deployed as implant materials [1, 7, 8]. More importantly, Mg is also vital in human metabolism processes and has been shown to increase the rate of bone formation [9-11].

In spite of the highly advantageous properties of Mg and its alloys, they have rarely been used as human body implants. The major drawback in the use of Mg alloys as implants is their

tendency to corrode very quickly in the physiological environment (that has a pH = 7.4–7.6) [1, 8, 12-16], thereby losing their mechanical integrity before the end of desired service life. Implant devices often experience considerable loading during service. The synergistic presence of mechanical loading combined with the corrosive environment of human body fluid may pose serious complications involving sudden fracture of implants due to stress corrosion cracking (SCC). SCC is an embrittlement phenomenon that can occur even at stresses below yield strength, leading to a premature brittle failure. Brittle cracks generally initiate at locations with sharp contours such as the root of a corrosion pit. Pre-existing macro/microscopic flaws (such as those developed during fabrication) can also markedly increase the probability of premature SCC-induced failures. SCC is therefore a serious concern when deploying implant devices comprising Mg alloys because: (a) common temporary implant devices (such as screws, stents, pins and plates) possess sharp contours and (b) Mg alloys readily suffer pitting in chloride solutions (pits are common crack initiators) [16, 17]. Indeed, Mg alloys have been reported to be susceptible to SCC in chloride solutions [18, 19], but it is also relevant to note that the traditional metallic implants (stainless steels and titanium alloys) have suffered premature, sudden and catastrophic SCC fracture in the physiological environment during service periods [20, 21].

Most studies on the deployment of Mg alloys as implant materials have aimed at improving their corrosion resistance in the physiological environment [22-25]. The literature on mechanical integrity/SCC behaviour of Mg alloys in the human body environment is generally limited to a few preliminary investigations [16, 26, 27]. Therefore, this study aims to establish a mechanistic understanding of SCC of rapidly corroding magnesium alloys (AZ91D and Mg3Zn1Ca) using slow strain rate tensile (SSRT) testing under different electrochemical conditions in the physiological environment of modified-simulated body fluid (*m*-SBF). However, for an alloy conducive to SCC, it is extremely important to determine the likelihood of an existing flaw (micro-crack, pit, sharp contour etc.) to grow as a stress corrosion crack,

i.e. threshold stress intensity for SCC ( $K_{ISCC}$ ) as well as the crack growth rate, for predicting life of an implant device when exposed to corrosive environments. In this study, a simple and recent fracture mechanics-based technique has been employed for determination of  $K_{ISCC}$  of AZ91D in the *m*-SBF solution (Chapter 4).

It is highly unlikely that AZ91D alloy will be used for implant applications because it contains a considerable amount of aluminium (Al), which is known to cause various neurological disorders such as dementia and Alzheimer's disease [28]. Accordingly, there has been an increasing interest in Al-free magnesium alloys as construction material of implant devices for short-to-medium term applications [29-32]. However, it has not yet been established whether these alloys possess the desired resistance to cracking under the simultaneous influence of mechanical loading and corrosive human body fluid. In this study, Al-free biodegradable magnesium alloys ZX50, WZ21 and WE43, specially designed for cardiovascular stent and temporary orthopaedic implant applications [32-34], have been evaluated for their resistance to SCC in the physiological environment (Chapter 5).

Localized corrosion and/or pitting of Mg alloys in aqueous environments have been suggested as prime factors in causing SCC [35, 36]. This thesis also reports an economical route for depositing a graphene-calcium carbonate ( $\text{CaCO}_3$ ) coating on a Mg alloy, which is aimed at achieving uniform and homogenous degradation (avoidance of localized corrosion/pitting, thus possibly the enhanced mechanical integrity) and improving biocompatibility. Thorough analytical and electrochemical investigations have been performed for a comprehensive understanding of degradation kinetics of the coating. Further, the role of the coating in providing improved biocompatibility and mechanical integrity of a Mg alloy in *m*-SBF solution has been discussed and explained (Chapter 6).





## **Chapter 2**

### **2. Literature review**

#### **2.1 Implant devices**

Human longevity has considerably improved in last century with significant advances in the field of medical science. The most notable improvements include development of implant devices since clinical cases requiring medical implants are increasing with desire for an active lifestyle and aging of the population. Implants are artificial devices used in the human body for repairing fractured bones and restoration of any impaired physical functions [37, 38]. Implant devices support the living tissues until full regeneration or healing is completed. Common use of implant devices can be varied based on the following requirements [39]:

1. To aid in healing process of tissues by using plates, rods and screws for the stabilization of fractured bones;
2. To improve the function of an organ or other parts of the body;
3. To correct a deformity, such as abnormal spinal curvature; and
4. To replace a damaged, diseased or worn part of the anatomy such as damaged arthritic joints or malfunctioning heart valves.

Since implant devices are employed in the physiological environment, they must satisfy certain requirements, which include: (1) excellent biocompatibility, requiring an adequate biological response, (2) sufficient mechanical properties, i.e. strength to hold or support the injured body part/tissues, and (3) excellent resistance to corrosion and fatigue, without releasing potentially harmful degradation by-products into the physiological system [40, 41].

A few most common implant devices used in orthopaedic and cardiovascular applications include shoulder implants (Fig. 2.1a), knee prostheses (Fig. 2.1b), hip implants (Fig. 2.1c) and stents (Fig. 2.1d). Most of the orthopaedic fracture fixation and cardiovascular implants for load bearing applications are manufactured using alloys, viz., stainless steels, cobalt chromium (Co-Cr) and titanium (Ti) alloys [5, 39-43]. The traditional implants of stainless steels, Ti and Co-Cr alloys are commonly used in medical applications primarily owing to their excellent mechanical and corrosion properties [1]. These materials for construction of implant devices are also expected not to cause any cytotoxicity [44]. However, there are considerable reports to suggest that the presence of these traditional implant devices may have adverse effects on adjacent human tissues due to release of toxic ions or corrosion products in the physiological system [2-4, 45-48]. Also, conventional metallic stents used in cardiovascular surgeries can cause thrombogenicity, permanent physical irritation, chronic inflammatory local reactions [14, 49]. Moreover, when these traditional alloys are used as temporary implant devices, such as plates, screws and wires, a second surgery is often required to remove the implant after tissues have healed, thereby increasing healthcare costs and patient morbidity [1, 50]. The removal of these permanent implant devices becomes essential after the healing process completes since they remain as an obstruction in the human body and also have an inability to adapt with growth of the human body.

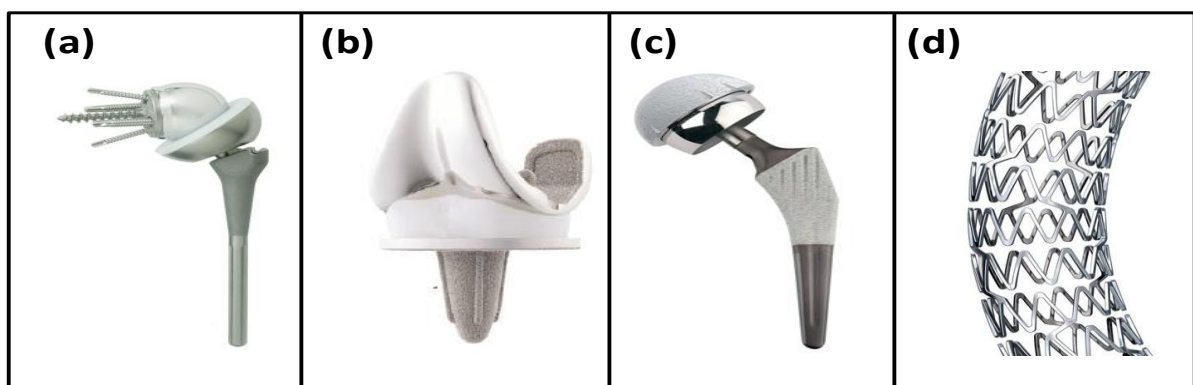


**Fig. 2.1.** Most common implant devices used in load bearing applications: (a) shoulder implant (b) knee prostheses (c) hip implant and (d) coronary stent [51]

Additionally, difference in the mechanical properties of the present implant materials and the bone can cause stress-shielding effects, leading to a reduction in strength of the adjacent tissue/bone [40, 52, 53]. It is suggested that the bone develops and remodels in response to the experienced load and requires a minimal time-averaged stress in order to maintain its mass [40]. If the stress falls below this threshold level, bone will be lost. If the stress increases beyond this threshold, bone will be added until the stress experienced returns to desired level.

Stress shielding occurs when the stress in bone is reduced below its maintenance threshold as a result of the very high mechanical properties of an implanted structure. Fig. 2.2a shows a radiograph of a femur in which significant bone loss has occurred around the proximal end of the implant (indicated by circled areas), with stress shielding being one of the underlying causes [40]. In many hip implant designs, while the stress in the bone in the proximal region of the implant is reduced, an increase in stress is seen in distal regions. This results in deposition of additional bone due to increased stress transfer in distal region, as shown in Fig. 2.2b.

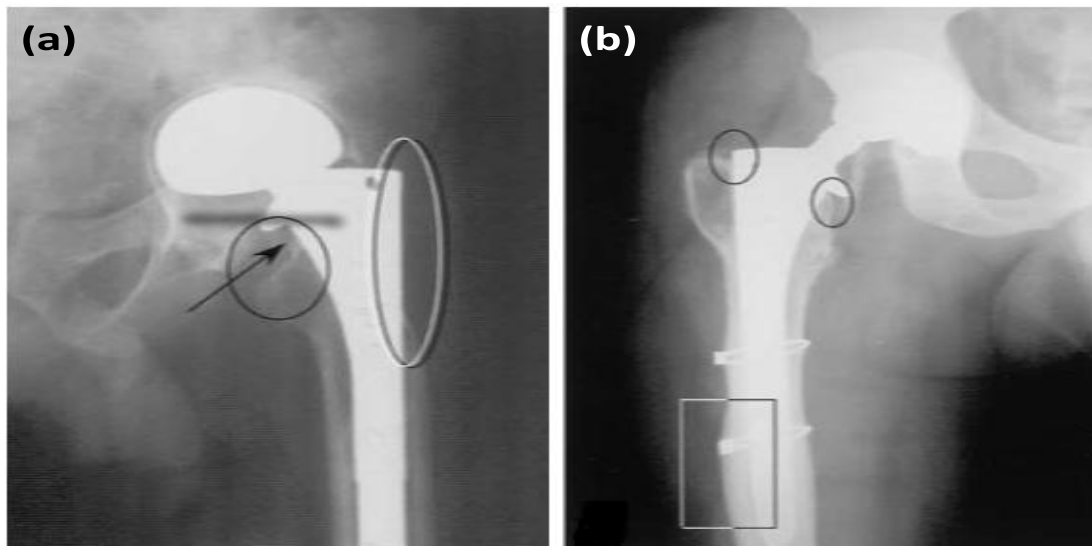


**Fig. 2.2.** Radiographs of hip implants showing changes in bone mass resulting from stress shielding around an implant: (a) bone loss at the proximal region, and (b) proximal bone loss (indicated in the circled regions at the edge of the prosthesis) is accompanied by increased bone deposition (indicated by the rectangle) in the distal region of the implant [40]

The drawbacks/problems associated with the traditional temporary implant materials could be overcome with the use of biodegradable implant materials. Hence, a continuous effort has been made in exploring the possible materials for use as biodegradable temporary implant devices. During tissue healing process, temporary biomaterial can gradually lose its mechanical property by continuing degradation process (Fig. 2.3) [54]. Degradable implants thereby prevent the need for a second operation for patients after tissues have completely healed.

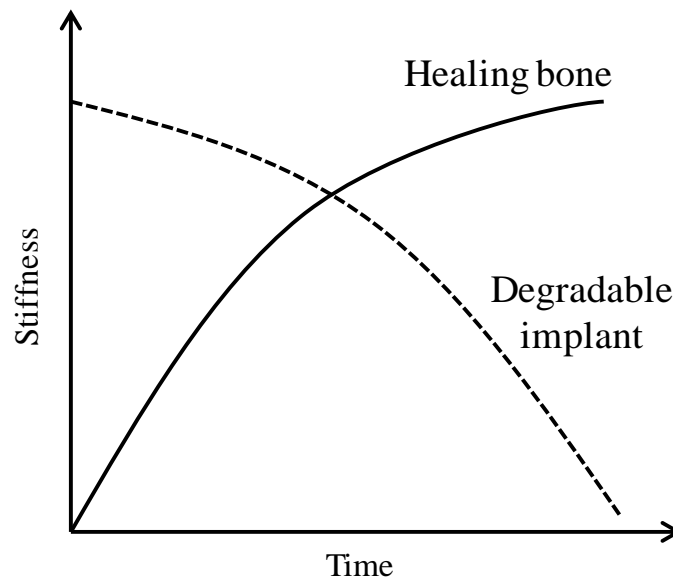


**Fig. 2.3.** Gradual loss of mechanical integrity of a temporary or biodegradable implant while the surrounding tissue is regaining mechanical strength [54]

In recent times, polymer-based biodegradable and bioresorbable implant devices are commercially available with poly-glycolic acid (PGA), poly-lactic acid (PLA) and poly-dioxanone (PDO) being the most commonly used absorbable materials [55, 56]. However, the use of biodegradable polymers in load bearing applications has been limited owing to their inadequate mechanical properties [1]. Nevertheless, biodegradable metallic materials have an advantage of desirable mechanical properties (such as favourable mechanical strength and fracture toughness) over existing biodegradable materials (i.e. polymers, ceramics or bioactive glasses) in load bearing implant applications [5, 57]. Accordingly, the requirement of a

biodegradable material with improved mechanical properties and controlled degradation in the body without releasing any harmful by-products into physiological system has led to increased research interest on magnesium (Mg) and its alloys.

## **2.2 Magnesium alloys as biodegradable temporary implant**

Magnesium (Mg) and its alloys have been researched extensively because of their extraordinary potential in engineering and structural applications [57]. Besides being one of the lightest engineering alloys, they also have high strength-to-weight ratio [57, 58]. They possess a great future in automotive, aerospace and defence industries giving the advantage of reduced mass, while offering good mechanical and physical properties, thus improving the fuel consumption efficiency.

In recent times, Mg and its alloys have also attracted a significant research interest as materials for construction of biodegradable temporary implant devices in biomedical applications. This interest is particularly due to a few of their beneficial properties including excellent biocompatibility, favourable mechanical properties and biodegradability [1]. The advantages of using Mg and its alloys as biodegradable materials are discussed below in detail.

### **Advantages:**

#### **1. Biocompatibility and osteogenesis**

As discussed earlier, the current biomaterials, i.e. Ti alloys, Ni-based alloys, Co-Cr alloys and stainless steels, may exhibit detrimental response to the adjacent tissues due to possible release of toxic metallic ions and/or particles through corrosion or wear processes, thus reducing biocompatibility and causing tissue loss and potential health risks [2-4, 45-48]. In contrast, Mg is biocompatible [1, 7, 59, 60] and has been shown to facilitate new bone formation [59, 61]. Mg ions are the fourth most abundant cations in the human body

(human body:  $\text{Ca} > \text{K} > \text{Na} > \text{Mg}$ ) [9]. The average adult body contains approximately 21–28 g (about 1 mole) of Mg, with approximately half of it stored in bone tissues [62]. The normal dietary requirement of Mg for an adult is 300–400 mg/day [1]. Mg is also essential for human metabolism as a cofactor for many enzymes [9, 10], and for normal neurological and muscular functions [63]. Unlike traditional implant materials, the degradation products of Mg are not toxic to the human physiology. In fact, Mg ions that are produced as a result of degradation are reported to aid the growth and healing of tissues [1]. Further, any excess Mg is harmlessly excreted in the urine [10].

## **2. Biodegradability and avoidance of second surgery**

As mentioned earlier, a second surgery is generally required to remove the implants after completion of tissue healing in the application of commonly used metallic materials for temporary implant purpose, which adds to extra troubles to patients and additional costs. However, Mg is highly electrochemically active and corrodes in aqueous environments, including physiological solutions [6, 64–66]. In the use of Mg alloys as temporary implants, the susceptibility of Mg to rapid electrochemical dissolution (corrosion) can be advantageously exploited, i.e. the Mg alloy will dissolve away after performing its function. Thus, the use of Mg alloys in temporary implant applications may obviate the need for second surgery.

## **3. Favourable mechanical properties: less likelihood of stress shielding**

Mechanical properties of Mg and its alloys (Table 2.1) are quite suitable for implant applications, viz., low density ( $\rho$ ) = 1.74–2.0 g cm<sup>-3</sup>, and elastic modulus ( $E$ ) = 41–45 GPa, both of which are closer to these properties of human bones ( $\rho$  = 1.8–2.1 g cm<sup>-3</sup> and  $E$  = 3–20 GPa) [1, 5]. Therefore, stress shielding related problems can be greatly reduced with the use of Mg alloys as orthopaedic/cardiovascular implants, most critically in high load bearing areas.

Table 2.1: Mechanical properties of traditional and Mg alloys as compared to human bone [5]

Property	Natural bone	Mg alloys	Ti alloys	Co-Cr alloys	Stainless steels
Density (g/cm <sup>3</sup> )	1.8-2.1	1.74-2.0	4.4-4.5	8.3-9.2	7.9-8.1
Elastic modulus (GPa)	3-20	41-45	110-117	230	189-205
Yield strength (MPa)	130-180	85-190	758-1117	450-1000	170-310

#### 4. Machinability and dimensional stability

Mg alloys are mechanically easier to machine, and stable final dimensions are easy to achieve [58]. As a result, the intricate shapes of implant devices (such as stents and screws), that are often required in medical applications, can be easily produced. Easy machinability is also convenient for producing devices for patients of different age, heights, weights etc., which have to be tailored individually to fit each patient. In addition, Mg and its alloys are much cheaper as compared to traditional implant materials.

#### 5. High damping capacity

Mg has excellent damping capacity (ability to absorb vibrations) [67]. In implant applications, this can be very important in high load bearing applications where the shock and vibration absorbing properties are critical criteria.

Based on above discussion, it could be said that functional bioresorbable implants based upon Mg and its alloys may bring paradigm changes in the biomedical industry as they provide the mechanical benefits of a metal combined with the degradable and biological advantages displayed by polymers and synthetic biomaterials [68]. However, there are some serious challenges to address before successful implementation of Mg-based materials in temporary implant applications.



## **Drawbacks:**

### **1. Rapid degradation**

It is anticipated that Mg and its alloys may be applied as lightweight, degradable, load bearing orthopaedic and cardiovascular implants, which could remain in the body temporarily and maintain mechanical integrity over a time scale of 12–18 weeks while the bone tissue heals [68]. But main drawback is that the Mg and its alloys corrode very rapidly in the physiological environment [1, 6, 13, 68-72]. Because of high corrosion rate, Mg-based implant devices may lose their mechanical integrity before completion of the tissue/bone healing. However, continuous efforts are being made for improving the corrosion rate of Mg alloys by controlling the impurities [73] and by application of coatings [74].

### **2. Toxicity of alloying elements**

Magnesium does not pose any toxicity/biocompatibility issues, as discussed earlier. However, the use of pure Mg as biodegradable implant material will be impractical because of lack of strength, and hence the alloying of Mg for developing high strength Mg alloys to be used as biomedical implants becomes inevitable. However, some of the common alloying elements for Mg alloys (such as aluminium) are toxic to the human body and their excessive release may be a critical factor in selection of alloying elements [75]. In fact, even the elements normally present in the body (e.g. Zn, Ca and Mn) can also be toxic if the release rate is too high. Consequently, non-toxicity would be a primary factor while choosing the alloying elements for designing biodegradable Mg alloys.

### **3. Hydrogen evolution**

Hydrogen gas ( $H_2$ ) evolution is concurrent with corrosion of Mg/Mg-based alloys [12, 24, 64, 70, 76, 77], which can cause various problems. Gas pockets may form adjacent to the implants that can cause separation of tissue and/or tissue layers [12]. The evolved

hydrogen can also interfere with the healing process and lead to necrosis of surrounding tissues [78]. In the worst case scenario, gas bubbles could block the blood stream, causing death of patients [50].

The critical tolerated rate of hydrogen evolution, which is reported to be  $< 0.01$  mL/cm<sup>2</sup>/day, can be used to screen out biodegradable Mg alloy candidates based upon in-vitro studies [12]. But it is also noted that each alloy must be investigated in-vivo in relation to its intended function. In some of the in-vivo studies, it was reported that the evolved hydrogen was present as gas pockets for the first week after surgery but disappeared after 2–3 weeks [33, 59]. Therefore, it is reasonable to infer that the hydrogen evolution during Mg alloy degradation will not present a serious problem, provided that the corrosion rate of the Mg-based implant device is controlled (i.e., hydrogen evolution rate  $< 0.01$  mL/cm<sup>2</sup>/day) [12].

#### **4. Mechanical integrity**

As Mg and its alloys corrode very rapidly, they may lose their mechanical integrity before accomplishing the tissue/bone healing task. These implant devices also experience considerable loading during service. As a result of the combined effect of mechanical loading and corrosive physiological environment, they may suffer premature failure due to environmentally assisted cracking, viz., stress corrosion cracking (SCC) and corrosion fatigue (CF) [27, 79].

In general, each of the drawbacks discussed above (rapid degradation, toxicity of alloying elements, hydrogen evolution and mechanical integrity) has its origin in the high corrosion rate of Mg alloys in the physiological environment. In view of this, it is important to understand the underlying reasons for the high corrosion rate of Mg and its alloys in aqueous environments such as physiological solution, which are discussed in Section 2.3.

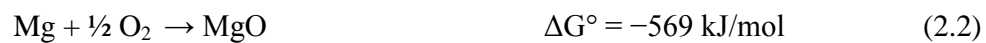
## 2.3 Corrosion of Mg/Mg-based alloys: in general

Mg alloys are prone to accelerated corrosion in aqueous environments. The main reasons for high corrosion rate can primarily be attributed to (i) less protective  $\text{Mg}(\text{OH})_2$  film that develop on Mg alloys, and (ii) galvanic corrosion induced due to the presence of secondary phase precipitates/impurities [66]. This section briefly describes the electrochemical characteristics of Mg and the thermodynamics of Mg corrosion in aqueous environments.

### 2.3.1 Thermodynamics of corrosion of magnesium

Magnesium is electrochemically highly active and has a standard reduction potential of  $-2.4$  V vs. standard hydrogen electrode (SHE) at  $25^\circ\text{C}$ , which is the lowest among all engineering metals [65, 66]. However, for practical purposes, actual corrosion potential of Mg in contact with dilute chloride solutions is  $-1.7$  V [6, 64]. This difference between the theoretical standard potential and actual corrosion potential is due to the formation of a surface film of  $\text{Mg}(\text{OH})_2$  or  $\text{MgO}$  [6].

Mg is thermodynamically very unstable and has a very high tendency to spontaneously transform into its oxidized states in aqueous environments, which can be explained on the basis of very negative free energy of the oxidation of Mg (Equations 2.1-2.3) [66]:



Due to negative free energy of these reactions, exposure of Mg to environments containing water leads to rapid oxidation, thereby resulting in instantaneous formation of an oxide or hydroxide surface film. The thermodynamic data in Table 2.2 suggest that Mg will rapidly oxidize into  $\text{Mg}(\text{OH})_2$  in preference to  $\text{MgO}$  since the chemical potential ( $\mu_o$ ) of  $\text{Mg}(\text{OH})_2$  is more negative than  $\text{MgO}$ .

Table 2.2: Chemical potential of Mg and its components in various states at 25 °C [66, 80]

Species	Oxidation state	$\mu_o$ (kcal/mol)
Mg	0	0
$Mg^+$	+1	-61
$Mg^{2+}$	+2	-109
$Mg(OH)_2$	+2	-199
MgH	-1	+34
$MgH_2$	-2	-8

Thermodynamic stability of Mg can be predicted by Pourbaix diagram ( $E$ -pH diagram), shown in Fig. 2.4 [81]. The numbered lines (1, 2 and 3) separate the regions of corrosion (dissolved cations, e.g.  $Mg^{2+}$ ), immunity (unreacted metal, Mg), and passivation (corrosion products, e.g.  $Mg(OH)_2$ ).

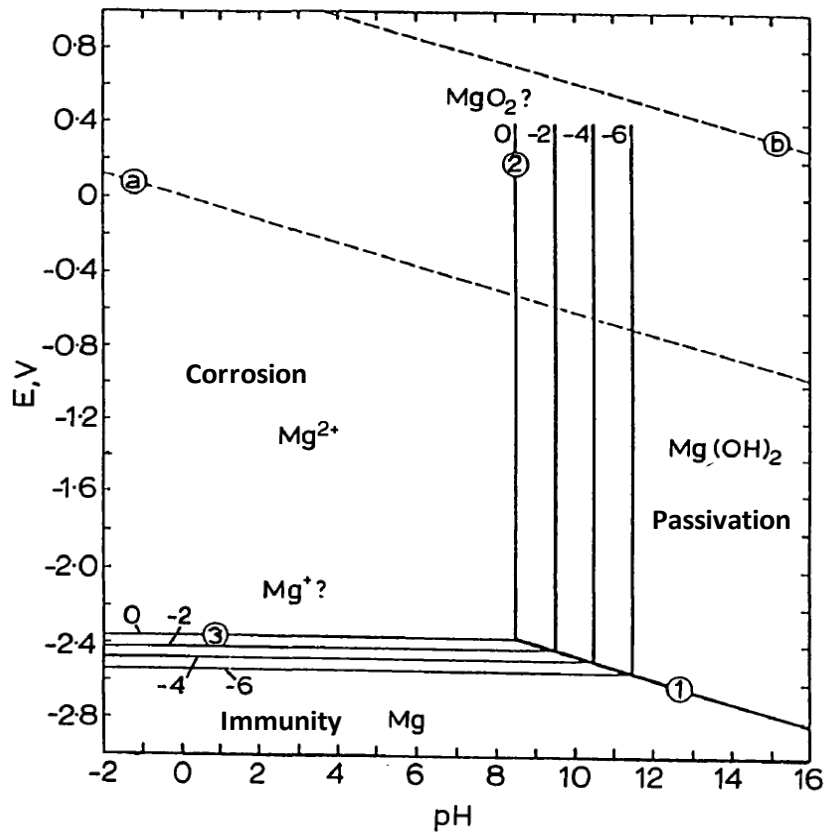


Fig. 2.4. Pourbaix diagram for Mg-water system at 25 °C [81]

The Pourbaix diagram (Fig. 2.4) also clearly shows the presence of oxidized Mg ions in most of the  $E$ -pH regions. This leads to a very large corrosion domain, a narrow negative potential region of immunity (much more negative than its equilibrium potential) and a possible high alkaline ( $\text{pH} > 10.5$ ) passive range [64, 81, 82]. It should be noted that the  $E$ -pH diagrams can only predict the thermodynamic stability or tendency for corrosion of Mg in water, and do not provide any information about the kinetics of the reactions, detailed reaction steps or the intermediate reaction steps [82]. Moreover, the effect of chemical composition of solution on the corrosion reactions/rates cannot be identified with  $E$ -pH diagrams. For example, it cannot predict the different corrosion rates of Mg in two aqueous solutions with same pH but different NaCl concentrations [66].

### **2.3.2 Stability and protectiveness of surface film**

As discussed in Section 2.3.1, Mg readily forms oxide/hydroxide films when exposed to aqueous environments. In most of the cases, corrosion of metallic materials is governed by the characteristics of its surface films [64]. Accordingly, it is necessary to characterize the surface film formed on the alloys for understanding the corrosion mechanism.

Based on thermodynamics data (Table 2.2, Fig. 2.4), the surface film on Mg is believed to be composed of MgO in dry environments and  $\text{Mg}(\text{OH})_2$  in aqueous environments. However, under normal atmospheric conditions, surface films on Mg may contain both MgO and  $\text{Mg}(\text{OH})_2$  [82].

Even though a surface film of Mg oxide or hydroxide develops, the film does not provide any appreciable corrosion resistance in aqueous environments. The explanation for poor protection provided by the surface films can be explained on the basis of the Pilling-Bedworth (P-B) ratio, which is volume ratio of metal oxide to metal. The P-B ratio of  $\text{MgO}/\text{Mg}$  is smaller than 1, therefore the oxide film cracks, causing inadequate corrosion protection under normal dry

conditions [58, 66]. However, the P-B ratio may not be the primary factor to explain poor corrosion behaviour of Mg in aqueous environments. In fact, the P-B ratio of  $\text{Mg}(\text{OH})_2$  (that forms in aqueous environments) to Mg is actually greater than 1 [58]. Thus, there must be another mechanism for the poor protection of Mg by hydroxide film in aqueous solutions. This is explained on the basis of  $E$ -pH diagram (Fig. 2.4). As evident from Fig. 2.4, the  $\text{Mg}(\text{OH})_2$  is thermodynamically unstable in an acidic, neutral or weak alkaline solution, hence, offering a very limited corrosion protection for the substrate under normal circumstances. Moreover, it has also been reported that presence of aggressive ions (chlorides) in the solution can significantly accelerate the corrosion of Mg. In presence of such ions, the  $\text{Mg}(\text{OH})_2$  converts into  $\text{MgCl}_2$ , which is highly soluble in water than  $\text{Mg}(\text{OH})_2$ , thus leading to an accelerated corrosion attack of Mg [66].

### 2.3.3 Electrochemical processes

#### 2.3.3.1 Anodic processes: negative difference effect (NDE)

The general anodic dissolution reaction of Mg in an aqueous solution is described as follows [64]:



However, the detailed anodic dissolution of Mg is suggested to undergo an intermediate step involving unipositive  $\text{Mg}^+$  [66]. But  $\text{Mg}^+$  is not stable and can rapidly transform into a more stable  $\text{Mg}^{2+}$  through either of the three possible mechanisms namely, anodic oxidation, disproportionation reaction and direct hydration [66].

Mg also exhibits a very unique anodic phenomenon known as the negative difference effect (NDE) [83, 84]. In recent times, there has been a significant interest in understanding the NDE effect for Mg corrosion. Normally, the rate of anodic reaction increases and the cathodic

reaction decreases with an increase of applied potential in anodic direction. Also, the rate of both the anodic ( $I_a$ ) and cathodic ( $I_c$ ) partial reactions are similar and equal to  $I_o$  at corrosion potential,  $E_{corr}$ .

Fig. 2.5 represents the schematic of experimental representation of NDE. When a potential ( $E_{appl}$ ) is applied in anodic directions (more positive than  $E_{corr}$ ), the rate of normal anodic partial reaction (i.e. current density) would be assumed to increase along the curve marked  $I_a$  to the value of  $I_{Mg,e}$ , and simultaneously, the cathodic partial reaction would decrease along the curve  $I_c$  to the value of  $I_{H,e}$ . However, in the case of Mg, both the anodic corrosion rate and also cathodic hydrogen evolution rate increases with increasing potential, as shown by the dashed lines marked by  $I_{Mg}$  and  $I_H$  in Fig. 2.5 [64, 83].

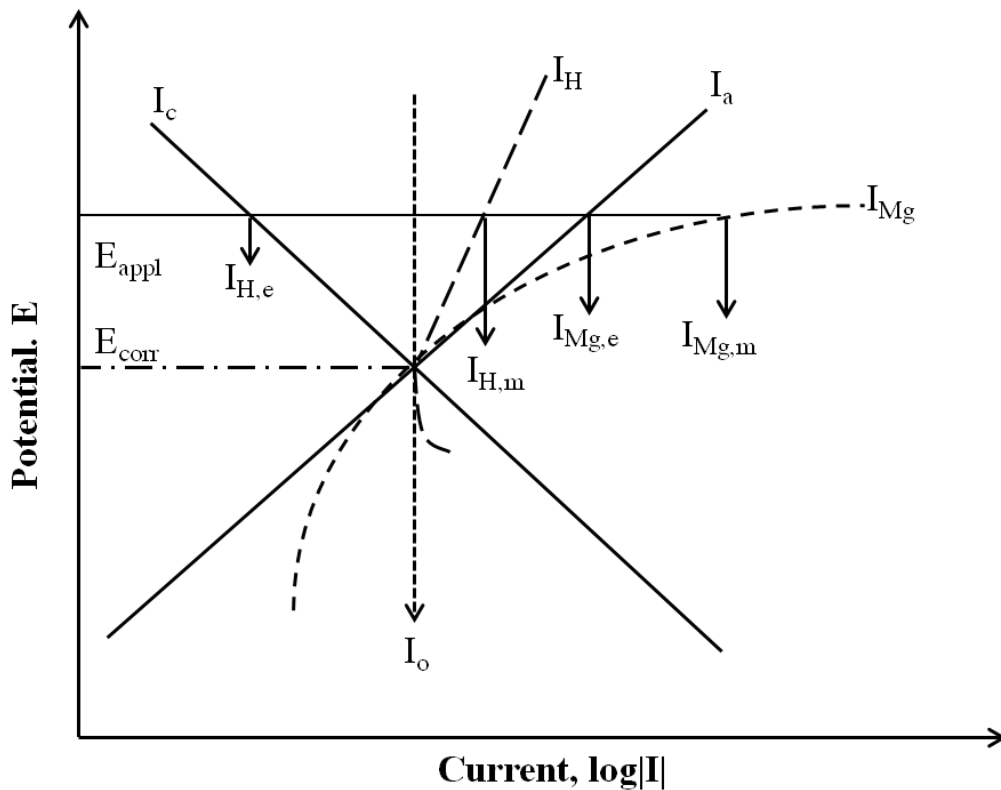


**Fig. 2.5.** The negative difference effect of Mg [64, 83]

For an applied potential,  $E_{appl}$ , the actual anodic reaction rate would be  $I_{Mg,m}$ , which is significantly greater than the expected anodic current ( $I_{Mg,e}$ ). Similarly, the actual cathodic

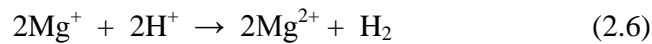
reaction rate ( $I_{H,m}$ ) is significantly greater than the expected cathodic current ( $I_{H,e}$ ). In general, the difference ( $\Delta$ ) between  $I_o$  (current density at  $E_{corr}$ ) and  $I_c$  at  $E_{appl}$  would be positive for most of the metals like iron, steels, zinc etc. However, this difference (defined by Equation 2.5) is negative for Mg because  $I_{H,m}$  is greater than  $I_o$ , and this phenomenon is called negative difference effect (NDE).

$$\Delta = I_o - I_{H,m} \quad (2.5)$$

The essential feature of NDE is that the cathodic hydrogen evolution reaction rate increases with an increase of electrode potential in the anodic direction. There is not a single consensus on mechanism for the NDE. Till now, four models for explaining the NDE in Mg and its alloys have been proposed, but each of these models is able to explain some aspects of the NDE, and fail to deal with other aspect [64].

#### **Model 1: monovalent magnesium ion model [80, 85]**

As calculated valence of dissolved magnesium was reported to be in the range from 1.33 to 1.66, it can be assumed that the  $Mg^+$  ions may be involved as an intermediate species in the anodic dissolution process and react chemically to evolve hydrogen according to the following reaction presented in Equation 2.6 [85, 86].



If the rate of univalent Mg ion production increases with increasing Mg dissolution rate, this mechanism would account for the observation of increasing rates of hydrogen evolution (Equation 2.6) with increased applied current or potential under certain conditions. However, there is no direct evidence of existence of  $Mg^+$  ion in the literature. In addition, several recent studies have established that the Mg dissolves with a stoichiometry of 2 without any intermediate reaction step involving unipositive  $Mg^+$  [87, 88].



**Model 2: partially protective surface film [89, 90]**

This mechanism attributes the NDE to the breakdown of a partially protective film on the magnesium surface during anodic dissolution. The film is assumed to be disrupted with increasing external current or potential. However, no evidence was provided for the surface film being partially protective.

**Model 3: particles undermining model [91]**

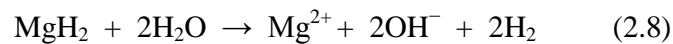
This mechanism explains the NDE in terms of the undermining and falling away of second phase particles during corrosion, especially at a higher anodic current density or potential, which may result in a mass loss greater than that due to only electrochemical dissolution. However, the NDE phenomenon is also observed in pure Mg, thus invalidating the particle undermining mechanism [92].

**Model 4: magnesium hydride model [80, 93]**

Magnesium can be reduced to hydride by the following electrochemical reaction:



The  $\text{MgH}_2$  is not stable in contact with water and reacts chemically to form hydrogen (Equation 2.8):



This mechanism is based on thermodynamic data which predicts the stability of  $\text{MgH}_2$ . However, Equation 2.8 is a cathodic reaction and should accordingly decrease in rate with applied anodic potential. Hence, the hydrogen evolution rate should decrease with an increase of potential, thus contradicting the basic principle of NDE.

### 2.3.3.2 Cathodic processes

Oxygen and hydrogen evolution are two typical cathodic reactions in most of the cases for corroding metal in an aqueous environment [65, 94]. However, in the case of Mg and its alloys, the hydrogen evolution reaction dominates the cathodic process [64, 69]. This domination can be explained on the basis of very negative equilibrium potential of Mg as compared to the hydrogen potential [65], and therefore the hydrogen reaction is strongly cathodically polarized. It has been generally accepted that the oxygen does not play any significant role in cathodic kinetics during the corrosion of Mg and its alloys [6, 64]. Accordingly, the main cathodic reactions for Mg alloys can be as follows [66]:



## 2.4 Corrosion of Mg alloys in the physiological environment

Mg and its alloys have been reported to suffer considerably rapid corrosion in the body environment that contains aggressive ions such as chlorides, carbonates, phosphates and sulphates in addition to presence of proteins and glucose [17]. When used as biomaterials, Mg alloys will face a number of different forms of corrosion as follows:

### 2.4.1 Galvanic corrosion

When two metals with different electrochemical potentials are in physical contact (electrically) and are exposed to an ion conducting fluid (such as serum or physiological solution), galvanic corrosion will occur [65]. The problem of galvanic corrosion is one of the major obstacles in successful use of Mg alloys in aggressive chloride containing environments. Mg makes an active anode when in contact with most metals owing to its high electrochemical activity and corrodes preferentially [6, 64].

Mg alloys are also not uniform in terms of their composition, microstructure and even crystalline orientation. These differences can result in various electrochemical activities within a Mg alloy, thereby generating galvanic couples on a micro-scale. The following two factors generally influence the formation of micro-galvanic cells in Mg alloys.

#### a) Impurities

The most Mg alloys contain iron (Fe), nickel (Ni), cobalt (Co) and copper (Cu) as impurities [6, 64], usually introduced during casting processes. These impurity metals are highly cathodic to Mg and can cause severe galvanic corrosion [6, 64]. Even small amounts of these impurities can dramatically increase the corrosion rate of Mg alloys, as shown in Fig. 2.6 [6].

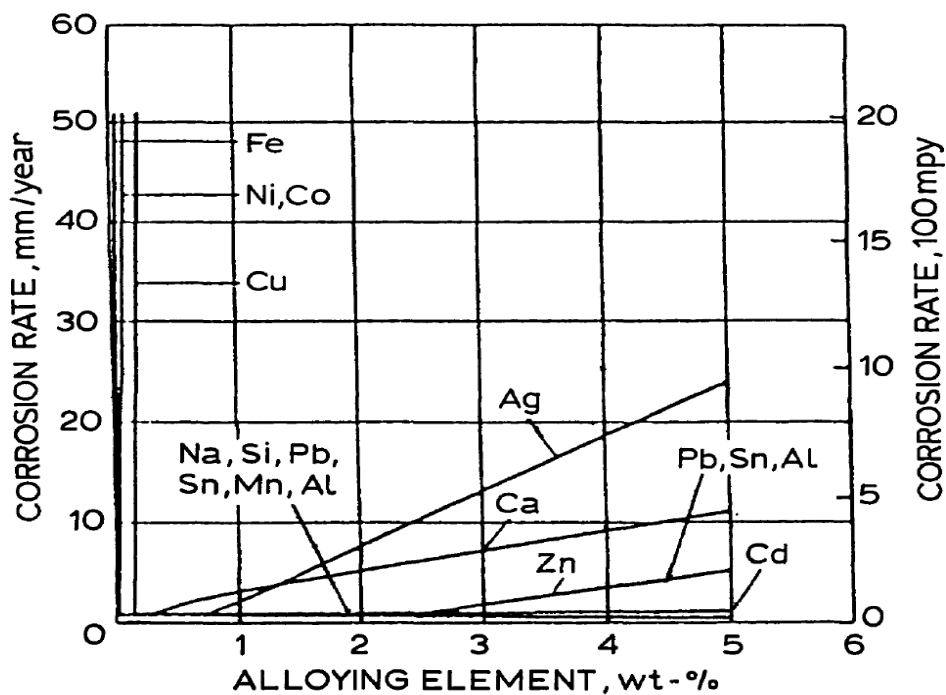


**Fig. 2.6.** Effect of impurities and alloying elements on corrosion rate of Mg alloys in 3 wt. % NaCl [6]

It is well known that a decrease in impurity content can improve corrosion resistance of Mg and its alloys [6]. The detrimental effect of impurities will be negligible below their tolerance limits, which can be associated with their solubility limits in Mg alloys. When these impurities are below a critical concentration (e.g. their solubility in the matrix phase), they are present in

the form of solutes in Mg solid solutions, and no micro-galvanic cells between the impurities and Mg matrix can be formed. The tolerance limits for Fe, Cu and Ni are 170, 1000, and 5 ppm, respectively [6].

## b) Secondary phases

Most of the Mg-containing intermetallic phases are more noble as compared to the Mg matrix. These intermetallic/secondary phases can play a dual role in the corrosion of Mg alloys: 1) they can act as micro-cathodes to accelerate the corrosion of the matrix, and 2) they can act as a barrier to the progress of corrosion front and retard corrosion in Mg alloys (Fig. 2.7) [66].

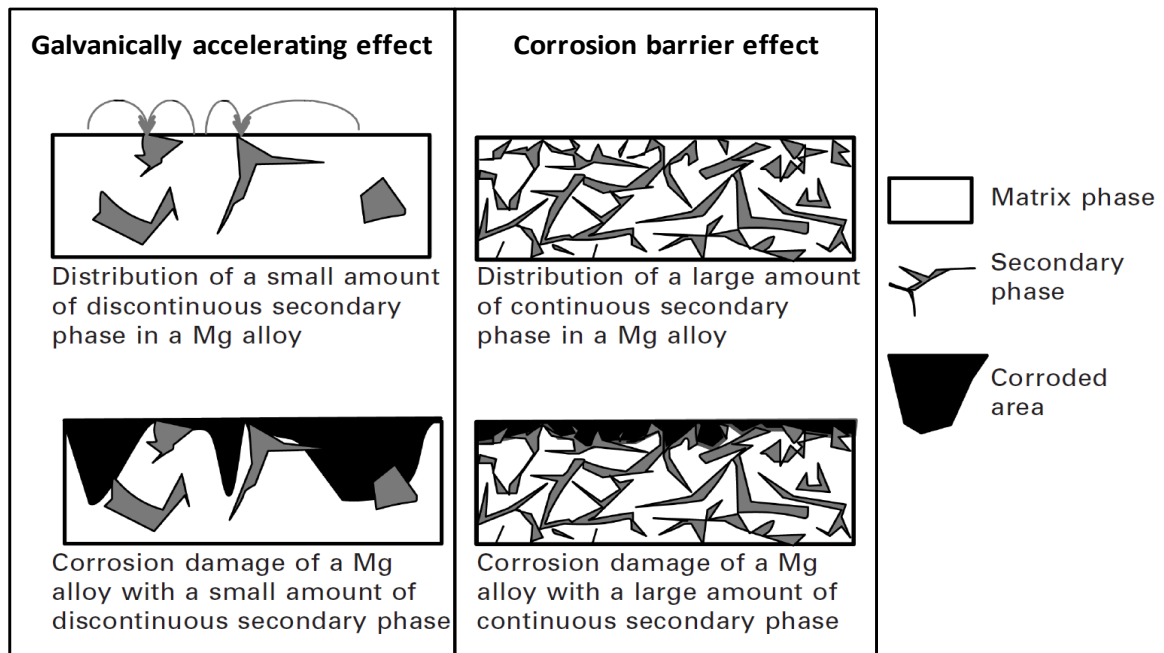


**Fig. 2.7.** Schematic representation of dual role of secondary phase of Mg alloys in corrosion [66]

For example,  $\beta$ -phase in common AZ alloys can either play a role in forming a corrosion barrier to retard corrosion or a galvanic cathode to accelerate corrosion, depending on the amount, distribution and continuity of the  $\beta$ -phase. A fine distribution of  $\beta$ -phase can form a continuous layer and be efficient in providing the corrosion barrier, whereas the presence of a small amount of discontinuous  $\beta$ -phase accelerates the micro-galvanic corrosion [66].

In the case of biodegradable Mg alloys, the problem of severe galvanic corrosion has been reported in several previous studies [13, 15, 16, 30, 70, 95, 96], which was attributed to the formation of micro-galvanic cells due to the presence of cathodic secondary precipitates/impurities as compared to anodic Mg alloy-matrix.

#### **2.4.2 Localized/pitting corrosion**

The biggest concern about the corrosion of Mg alloys is localized or non-uniform attack, which is normally attributed to the micro-galvanic effect or electrochemical in-homogeneity [64, 72, 97]. Mg may undergo pitting corrosion at its free corrosion potential,  $E_{\text{corr}}$ , when exposed to chloride ion containing medium [89]. Moreover, the presence of impurities, secondary phases and different alloying elements in the matrix can cause un-even distribution of micro-anodes and micro-cathodes in Mg alloys, leading to the non-uniform or localized corrosion damage.

The localized corrosion and pitting has been also observed during in-vitro and in-vivo corrosion studies of Mg alloys for biomedical applications [59]. By in-vitro and in-vivo investigations, Witte et al. [59, 61] found that the pitting corrosion occurred on both LAE442 (Mg- 4 wt. % Li – 4 wt. % Al – 2 wt. % rare earth) and AZ91D. While AZ91D was severely attacked by localized corrosion/pitting, LAE442 showed a more uniform corrosion attack with scattered areas of pitting. Several other studies have also established the susceptibility of AZ series Mg alloys to localized corrosion/ pitting in simulated body fluid (SBF). Zhou et al. [98] observed the localized corrosion along the residual  $\beta$ -Mg<sub>17</sub>Al<sub>12</sub> phase at the grain boundaries as well as found some pits within the grains (as indicated by arrows in Fig. 2.8a), after 8 h of exposure to simulated body fluid. Similarly, Kannan et al. [16] reported localized corrosion/pitting in AZ91 (Fig. 2.8b) after electrochemical testing in SBF. Similar localized corrosion and pitting were observed by Zhang and co-workers [99] in Mg-Zn-Mn-Ca alloys, which was attributed to the tendency of Mg<sub>2</sub>Ca network at the grain boundary to dissolve

preferentially after electrochemical testing in Hanks' solution (Fig. 2.8c). Recently, severe susceptibility towards localized corrosion/pitting was reported for a high-strength Mg alloy, ZX50 (specifically designed for temporary implant applications in osteosynthesis), during both in-vitro and in-vivo studies [32, 33, 100].

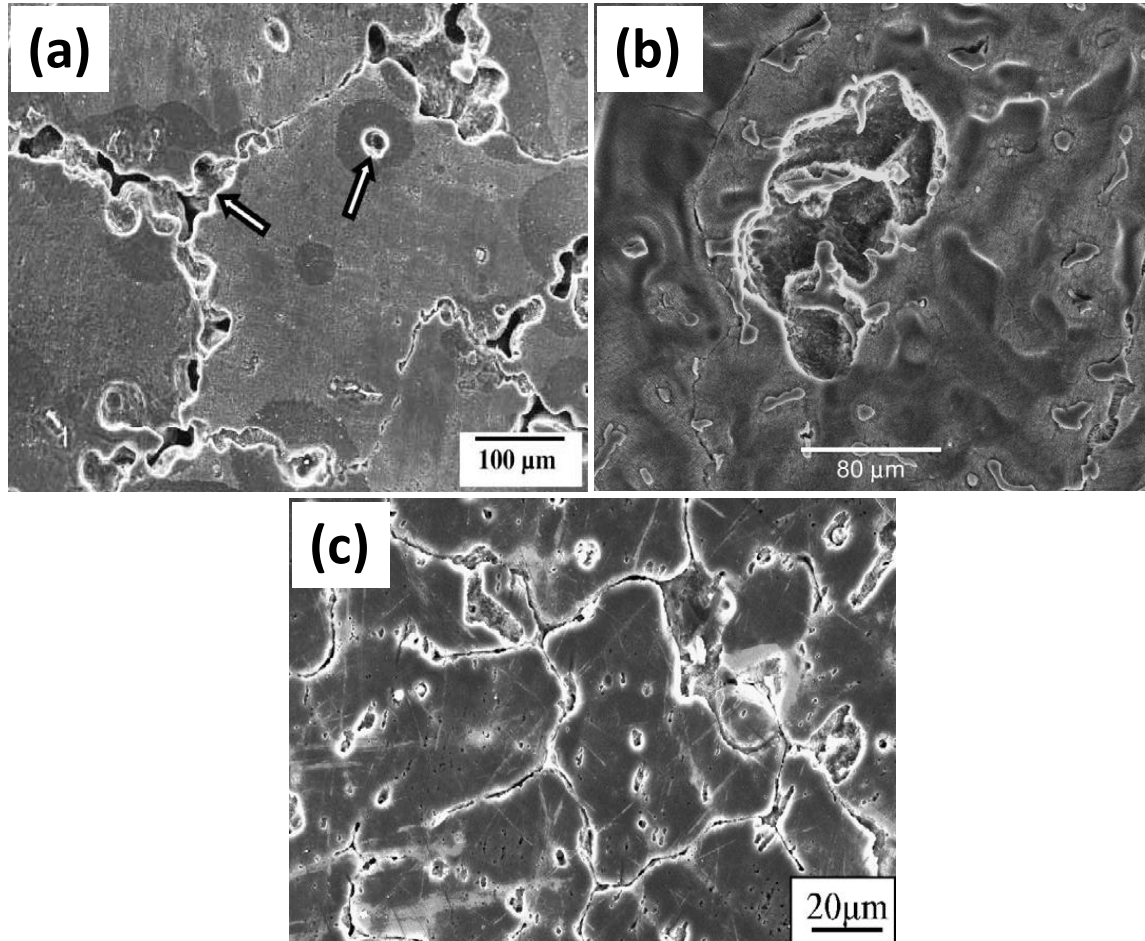


**Fig. 2.8.** Localized/pitting corrosion observed in different Mg alloys: (a) AZ61 [98], (b) AZ91 [16], and (c) Mg-Zn-Mn-Ca [99]

### **2.4.3 Stress corrosion cracking (SCC)**

A considerable fraction of research on Mg alloys has focused on improving their general mechanical properties, creep resistance and corrosion properties. The aspect that has received relatively less attention is their resistance to stress corrosion cracking (SCC).

SCC is a dangerous, complicated and insidious form of corrosion, and can cause catastrophic and unexpected failure of structural components [101]. It is sub-critical crack propagation in a brittle manner due to combined and interdependent effects of corrosion and tensile stress. SCC involves an optimum interaction of three parameters: (1) mechanical loading providing tensile stress, (2) a susceptible alloy, and (3) an environment causing corrosion at an acceptable rate [35, 102, 103]. Consequently, SCC is relatively less frequent, though failures can be very costly and destructive when they occur. Unlike other types of corrosion, surface may appear virtually un-attacked in the case of SCC. Only a few fine cracks (invisible to naked eye) initiate and propagate, which can lead to the brittle SCC failures [35]. The most fundamental and detrimental feature of SCC is that a ductile material that would have undergone considerable elongation before fracture may suffer embrittlement in the presence of the corrosive environment.

Mg and its alloys are also reported to be susceptible to SCC in common service environments [104-110]. It is estimated that approximately 10 to 60 Mg alloy components in aerospace applications alone suffered SCC failures each year during 1960 and 1970 [35]. It is suggested that the occurrence of SCC may be on increase since Mg alloys are now increasingly used in structural and automotive applications under load bearing and harsh environmental conditions. Increased SCC incidences may also be expected because of increased stresses as a result of smaller section sizes of the components in a bid to decrease weight. The details of phenomenology and mechanistic understanding of SCC of Mg alloys have been presented in the Section 2.5.

## **2.5 Phenomenology of SCC of magnesium alloys**

SCC mechanisms are generally dominated by mechanical or electrochemical processes, and often specific to certain combinations of alloy and environment. Transgranular stress corrosion cracking (TGSCC) is the common mode of SCC in Mg alloys [19, 35, 111, 112], but instances of intergranular stress corrosion cracking (IGSCC) has also been reported [18]. In the case of Mg alloys, it is generally accepted that the SCC processes usually involve hydrogen embrittlement (HE), with the source of hydrogen being cathodic reaction of the bare metal [36, 107, 113], but there is a little consensus on an unified SCC mechanism. This section briefly discusses the influence of alloying elements on SCC, techniques for characterization of SCC and possible operating mechanisms of SCC, in the case of Mg alloys.

### **2.5.1 Influence of alloying elements**

Most pure metals are immune to SCC; however, pure Mg has been reported to be susceptible to SCC [36, 114-116]. Stampella et al. [36] performed a range of slow strain rate testing experiments on commercial and high purity Mg in Na<sub>2</sub>SO<sub>4</sub> under different environmental conditions to establish the SCC mechanism. Both commercially pure and high purity Mg were reported to be susceptible to SCC at room temperature in deaerated, pH 10, 10<sup>-3</sup> M Na<sub>2</sub>SO<sub>4</sub>. They reported corrosion pits to be the necessary precursors for hydrogen embrittlement and cracking. Pits provided bare, active, film-free sites, which permitted cathodically generated hydrogen to enter the metal. In both commercial and high purity Mg, the fracture surfaces in Na<sub>2</sub>SO<sub>4</sub> appeared to be predominantly brittle, with transgranular regions exhibiting typical quasi cleavage morphology. In contrast, the specimens tested in air exhibited dimpled fracture surfaces as a characteristic of ductile failure by microvoid nucleation, growth and coalescence.

Meletis and co-workers [116] studied the SCC of 99.9 % pure Mg in 3.3 wt % NaCl + 2 wt % K<sub>2</sub>CrO<sub>4</sub>, and reported failure in the solution with 2.3 % of strain in comparison to 5.1 % of



strain in air, i.e. 55 % reduction in strain in solution as compared to air. Fracture surfaces also revealed TGSCC with specific features of cleavage-like fracture, which initiated at corrosion pits and was accompanied by H evolution.

Magnesium alloys are also reported to be susceptible to SCC in aqueous environments [18, 19, 104, 105, 107, 110, 117-120]. The alloying elements play a crucial role in either beneficial or detrimental manner on SCC of an alloy. The roles of most common alloying elements (Al, Zn and Mn) and impurity (Fe) on SCC of Mg alloys are discussed below.

### **Influence of aluminium (Al):**

All aluminium-containing magnesium alloys (such as AZxx (containing Al and Zn) and AMxx (containing Al and Mn)) have been reported to be susceptible to SCC to some extent in distilled water and chloride-containing solutions [35]. The susceptibility to SCC (represented as the minimum stress to cause SCC) was generally found to increase with increasing Al concentration, as shown in Fig. 2.9 [67].

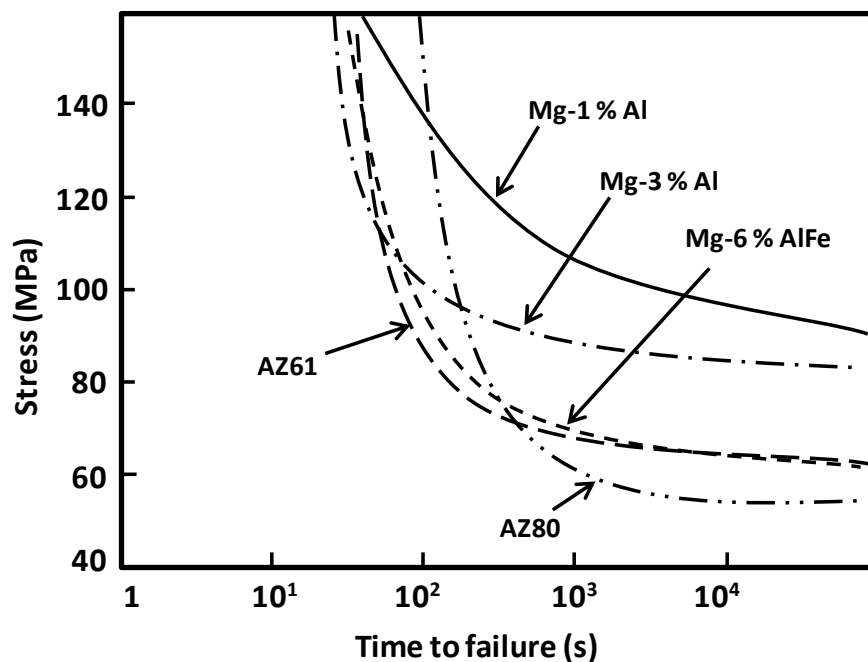


**Fig. 2.9.** Stress vs. time to failure curves for various Mg-Al alloys in 40 g/L NaCl + 40 g/L Na<sub>2</sub>CrO<sub>4</sub> [67, 113]

**Influence of Zn:**

Zinc also induces SCC susceptibility in Mg alloys [67]. It is also reported that magnesium-zinc alloys that are alloyed with zirconium or rare earths (but no aluminium) have intermediate SCC resistance [35].

**Influence of Mn:**

Mg-Mn alloys are among the alloys with high resistance to SCC, and generally considered to be immune when loaded up to the yield strength in common test environments [121].

**Influence of Fe:**

Iron that is found in commercial Mg alloys as an impurity is known to reduce the corrosion resistance by promoting micro-galvanic corrosion. The effect of iron on SCC of Mg alloys remains unclear. Perryman [122] reported that higher Fe content in Mg alloys decreased the SCC resistance in distilled water, whereas Timonova [123] reported that Fe had no effect on SCC of Mg-Al-Zn-Mn alloys.

**2.5.2 Characterization of SCC using different techniques**

There is no generalized approach that could provide a complete insight into prediction and mechanistic understanding of SCC. Combinations of a few techniques can qualitatively and quantitatively establish the susceptibility of different metals/alloys to SCC. The main techniques for characterization of SCC are slow strain rate tensile (SSRT) testing, U-bend testing, C-bend testing, compact tension (CT) testing, double cantilever beam (DCB) testing [101], circumferential notch tensile (CNT) testing [124] etc. A brief description of some of these testing methods is provided in this section.

### **2.5.2.1 Slow strain rate tensile (SSRT) testing**

The slow strain rate tensile (SSRT) testing is an uni-axial tensile test conducted at extremely low cross-head speeds in presence of a corrosive environment [101, 125]. These tests will invariably produce fracture either by SCC or mechanical failure or both. Slow straining ensures the opportunity for an environment to interact with crack-tip and also the presence of continuing plastic strain, which encourages the initiation and growth of stress corrosion cracks. The SCC susceptibility is evaluated in terms of the time taken for failure to occur, the extension at failure and/or appearance of fracture surfaces. SSRT is an accelerated laboratory testing and generate data in a relatively short time. Also, SSRT usually gives conservative results owing to the severity of the tests [126].

Strain rate is a critical parameter in the SSRT testing of Mg alloys. For specific combination of alloy and environment, SCC occurs in a narrow window of strain rates [127]. Wearmouth et al. [128] investigated the role of strain rate for Mg-7Al alloy in aqueous chloride-chromate solution, and attributed the role of strain to rupture any surface film for allowing localized dissolution or H ingress. Ebtehaj et al. [113] also investigated the influence of strain rate on SCC susceptibility of as-cast Mg-9Al alloy. They proposed that the film integrity was maintained at low strain rates, which prevented H ingress into the matrix, and failure occurred in ductile fashion. As the strain rate was increased, the film repassivation decreased and thus allowing H ingress more freely, causing embrittlement of the matrix. At relatively higher strain rates, ductile tearing occurred before embrittlement because of insufficient time available for H ingress. This explained the maximum SCC susceptibility at intermediate strain rates, as shown in Fig. 2.10 [113].

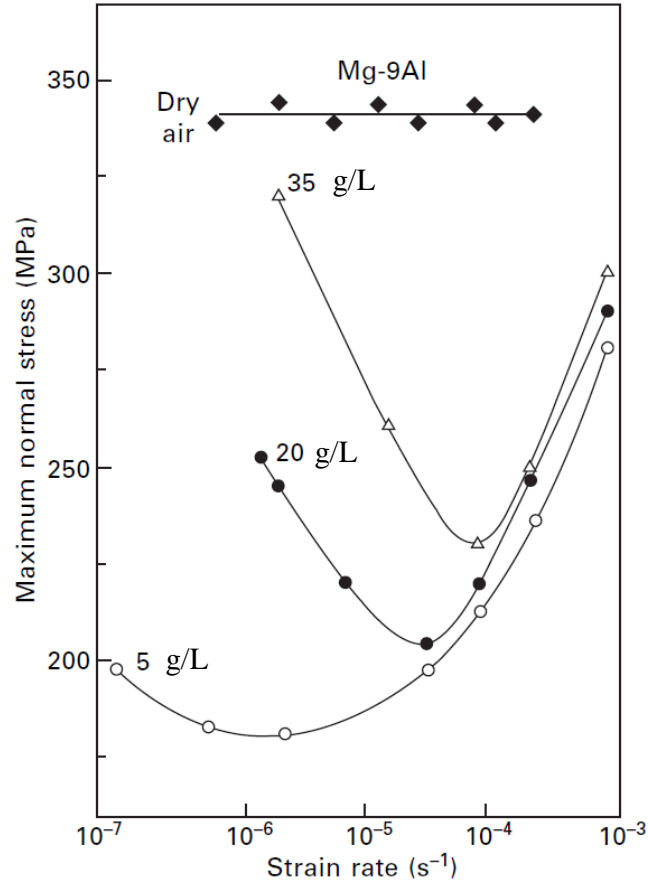


**Fig. 2.10.** The effect of strain rate on the maximum nominal stress to fracture the specimens exposed to dry air or solutions containing 5 g l<sup>-1</sup> NaCl and various amounts of K<sub>2</sub>CrO<sub>4</sub> [113]

In contrast to the maximum SCC susceptibility of Mg-Al alloy at intermediate strain rates in NaCl + K<sub>2</sub>CrO<sub>4</sub> solution (Fig. 2.10) shown by Ebtehaj et al. [113], Winzer et al. [104] found the maximum susceptibility of a Mg-Al alloy tested in distilled water at lowest strain rate. This was characterized by a greater decrease in UTS and elongation-to-failure in distilled water as compared to the laboratory air in low strain rate regime. The occurrence of maximum SCC susceptibility at intermediate strain rates, as reported by Ebtehaj et al. [113], is attributed to the passivating characteristic of the alloy in the chromate containing solution used in their study. The corrosion film developed in this passivating environment required higher strain rate to sustain SCC, whereas a less passivating solution in Winzer and co-workers' [104] study produced corrosion film that could be disrupted at lower strain rate and caused SCC.

### 2.5.2.2 Fracture mechanics based approach to SCC

The fracture mechanics based approach is used for quantitative determination of the important design parameters for materials susceptible to SCC. This type of study is of particular importance for the structural components for determination of safe service stress level in harsh conditions (for example, aerospace and automotive parts).

In general, damage tolerant design method principles are applied for performing these studies, which assume that structure/component contains initial cracks. The concept of fracture mechanics is then used to characterise the conditions for propagation of cracks from these initial flaws. Usually, SCC can occur at stresses below general yield strength and propagate in elastic body; hence, linear elastic fracture mechanics (LEFM) principles are applied for determining the crack tip stress intensity factor ( $K_I$ ) [125].

According to the LEFM approach, the  $K_I$  at the crack tip can be given by Equation 2.11.

$$K_I = Y \sigma (\pi a)^{1/2} \quad (2.11)$$

where  $Y$  is a geometrical factor,  $\sigma$  is the applied stress and  $a$  is the crack length.

For a given material/environmental condition, the typical schematic of relationship between stress intensity vs. crack growth rate is shown in Fig. 2.11 [125]. The value of  $K_I$  at which the first measurable crack extension occurs is characterized by threshold stress intensity for stress corrosion cracking ( $K_{ISCC}$ ). Consequently, there will not be any crack propagation at stress intensities lower than the  $K_{ISCC}$ . The practical meaning of  $K_{ISCC}$  lies in the fact that below this stress intensity factor, crack growth rates become insignificantly low (i.e.  $< 10^{-12}$  m/s) [35, 129].

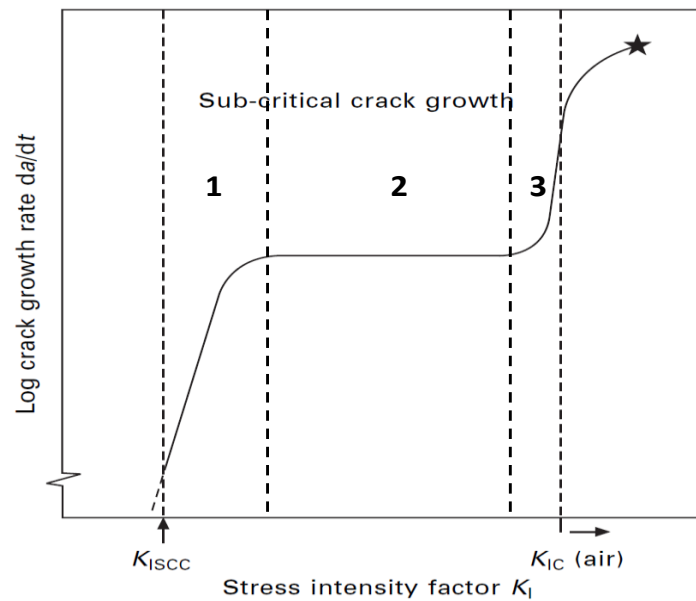


**Fig. 2.11.** Typical plot of stress intensity factor vs. crack growth rate [125]

The plot in Fig. 2.11 is specifically characterised by three zones: the region I (crack initiation and crack propagation), region II (steady state crack propagation) and region III (failure by overloading). During region I, the crack growth increases rapidly as the stress intensity is increased from the  $K_{ISCC}$ . The crack velocity is reasonably constant in region II and largely independent of the stress intensity factor. As the stress intensity factor approaches  $K_{IC}$  (i.e., fracture toughness - the critical stress intensity of the specimen tested in air at which it fails), pure mechanical rupture (ductile) dominates over sub-critical crack extension caused by SCC, and rapid crack growth occurs.

Determinations of  $K_{ISCC}$  and crack growth rate data for life prediction of components/structure are of primary importance for various industries including nuclear, automotive etc. Depending upon the component geometries, different fracture mechanics approaches have been used till now for determination of the  $K_{ISCC}$ . Compact tension (CT) testing and circumferential notch tensile (CNT) testing are among the common fracture mechanics testing approaches.

### a. Compact tension (CT) testing

Compact Tension (CT) testing is a popular technique to measure the  $K_{ISCC}$  and crack growth rates in presence of stress raising defects, which are normally provided by a pre-crack. CT testing requires application of an external constant load. The advantage of the CT testing is that the stress parameters can be quantified with confidence since this technique is based on visual observation and crack opening displacement monitoring (measured through a low power travelling microscope). The main disadvantages of the CT testing are higher cost and the requirement of bulky specimens to satisfy the valid plane strain conditions for LEFM application [125]. The Fig. 2.12 shows a schematic and geometry of a typical CT specimen.

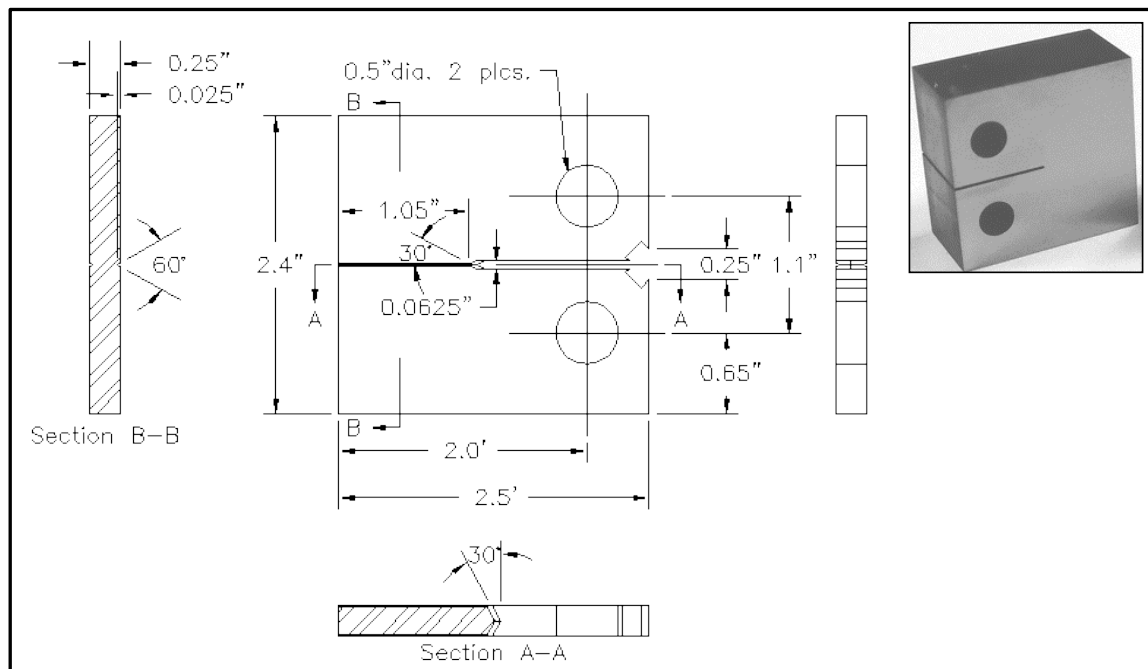


**Fig. 2.12.** Compact tension (CT) specimen (all dimensions are in inches) [101]

### b. Circumferential notch tensile (CNT) testing

A recent and relatively new fracture mechanics-based approach for determination of the  $K_{ISCC}$  using CNT specimens (Fig. 2.13) has been developed and validated at Monash University [124, 130-135]. The diameter of the CNT specimen is 9.5 mm with a 60° “V” groove in the middle, which gives a minimum notch root diameter of 7 mm.

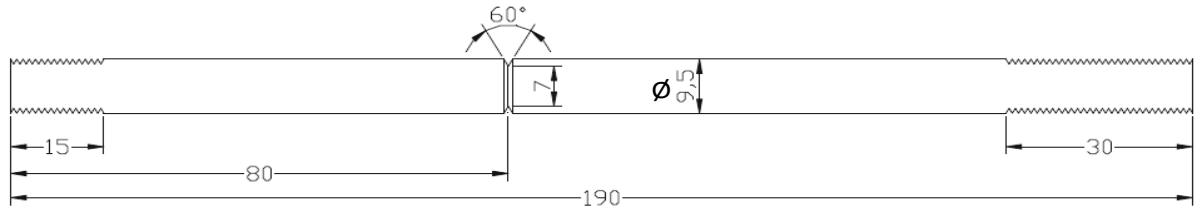


**Fig. 2.13.** CNT specimen (all dimensions are in mm) [131]

A fatigue pre-crack is developed ahead of the notch of a CNT specimen, by subjecting it to a controlled rotating bending fatigue load, which results in a typical final ligament diameter of about 5 mm. The pre-cracked CNT specimen is then subjected to a constant load in corrosive environment, until the specimen fails. Using the relationship between  $K_I$  and time-to-failure ( $t_f$ ), threshold stress intensity factor ( $K_{ISCC}$ ) is determined. An accurate determination of  $K_I$  is the key to successful application of the technique [124].

The data generated using the CNT testing are claimed to be within  $\pm 3\%$  of the data generated using the ASTM standardized CT testing [136-138]. However, CNT technique offers many other advantages over conventional CT testing method, as discussed below:

#### 1. *Smaller specimen size*

CNT technique uses specimens with smaller cross section. It is therefore possible to apply quite high stress levels using moderate loads. This also avoids requirement of heavy machinery and complicated loading system in case of CNT technique as compared to the CT testing. Moreover, it was found that the plane strain conditions are satisfied using 9.5 mm diameter cylindrical specimens in comparison of CT specimens requiring widths up to 80 mm [130].

#### 2. *Less material requirement*

Owing to smaller and simpler geometry of the CNT specimens (Fig. 2.13), considerably less amount of material is required in machining the CNT specimens as compared to the bulky and complex CT specimens (Fig. 2.12). In addition, it is possible to determine the SCC design parameters for narrow zones or thin components, such as heat affected zone, simply due to the



possibility of CNT testing using smaller cross section of the specimens. The necessary length of the CNT specimens could be achieved by using extension rod(s), which further reduces the requirement of material in the CNT testing (since area of interest is only the notch and nearby area). Also, cost of the CNT testing can be reduced by a factor of 10 as compared to the CT testing due to the smaller specimen size and less material requirement [139].

### 3. Time efficient

SCC testing is very time consuming as tests may run up to 10000 h. CNT technique is very time efficient in comparison to the CT testing. Due to simplicity of the CNT set-up, several CNT experiments (such as 20 CNT rigs are available in the Monash University laboratory) can simultaneously be started at the same time [139].

### 2.5.3 Mechanism of SCC in Mg alloys

Several mechanisms have been proposed for explaining the SCC of Mg alloys; however, there is no consensus on any given mechanism. SCC of Mg and its alloys has been generally attributed to (i) continuous crack propagation by dissolution at the crack tip (Fig. 2.14a), or (ii) cleavage type mechanism by discontinuous crack propagation (Fig. 2.14b) [35, 101].

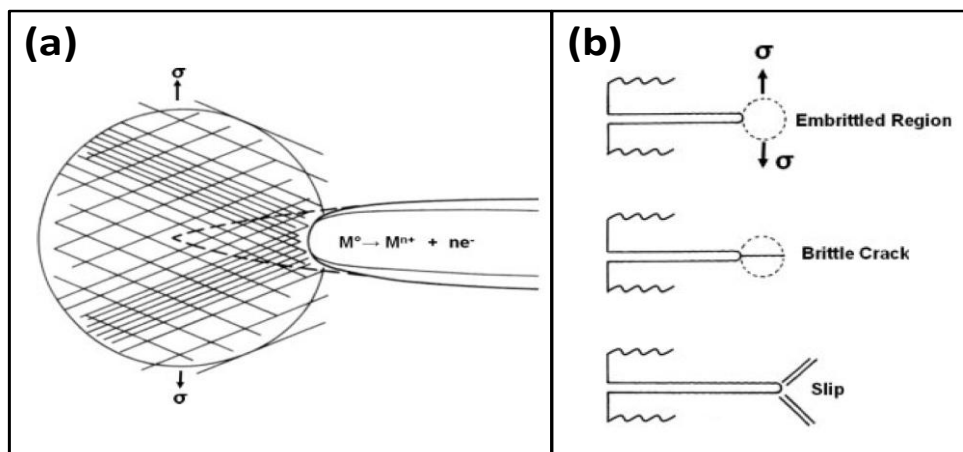


**Fig. 2.14.** (a) Continuous crack propagation by dissolution following film rupture, and (b) cleavage type fracture ahead of embrittled zone [35]

### 2.5.3.1 Dissolution mechanisms

#### a) Microgalvanic corrosion

The intergranular stress corrosion cracking (IGSCC) observed in Mg-Al alloys is often attributed to the preferential dissolution of the metal matrix adjacent to the secondary phase precipitates ( $\text{Mg}_{17}\text{Al}_{12}$  in Mg-Al alloys). Therefore, when the grain boundary precipitates are continuous, the crack propagation is also continuous [35]. IGSCC was also observed in rare earth (RE) containing Mg alloys. Kannan et al. [16] reported the IGSCC in ZE41 alloy in NaCl and distilled water (Fig. 2.15), attributing this behaviour to the micro-galvanic corrosion of second-phase particles that formed a continuous network along the grain boundaries.

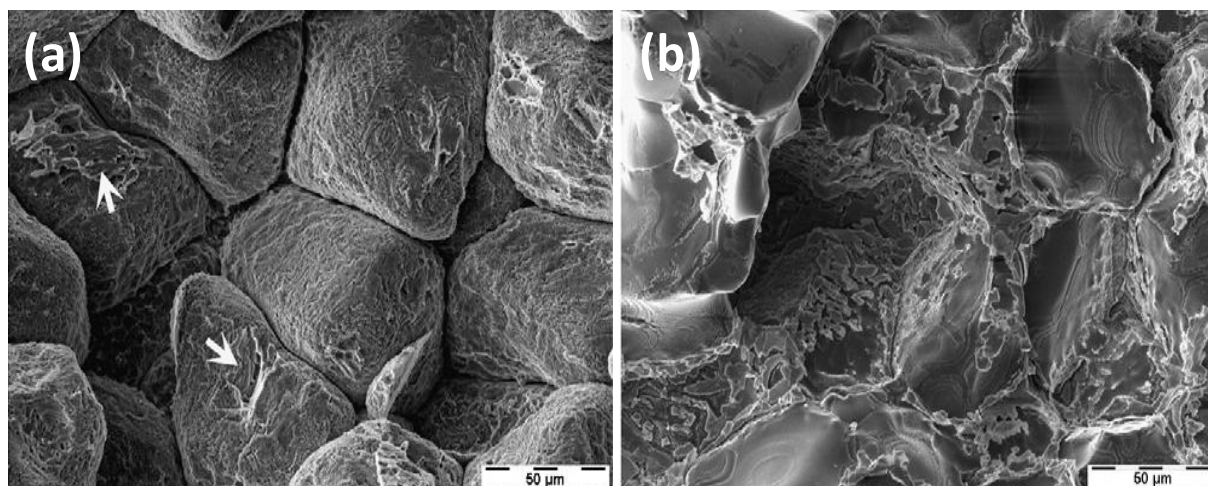


**Fig. 2.15.** Fracture surfaces of ZE41: (a) in 0.5 wt. % NaCl - predominant intergranular and isolated transgranular (arrows) cracking, and (b) in distilled water - corrosion along the grain boundaries [18]

#### b) Film rupture model

Localized plastic deformation at the crack tip causes rupture of passivating film [101]. This exposes the bare metal to the environment species, causing a rapid dissolution, which leads to crack extension or propagation. For Mg alloys, the crack growth rate in this alternative electrochemical SCC mechanism is defined by the competing rates of film rupture and regrowth, as proposed by Ebtehaj et al. [113] and Wearmouth et al. [128]. Also, crack

propagation will be continuous if the stress concentration at the crack tip is high enough to prevent the reforming of the film (i.e., repassivation is insignificant).

### 2.5.3.2 Mechanical fracture mechanisms

#### a) Cleavage fracture

In general, the transgranular stress corrosion cracking (TGSCC) is predominant in Mg alloys, which is associated with discontinuous cleavage. The lack of slip systems in Mg alloys makes them susceptible to the cleavage fracture. Various researchers [116, 140, 141] have reported that the TGSCC in Mg results due to alternating stages of electrochemical attack and mechanical fracture. TGSCC also resulted in fracture surfaces consisting of flat and parallel facets separated by perpendicular steps, consistent with the cleavage mechanism. Matching and interlocking opposite fracture surfaces confirmed the occurrence of cleavage, which was difficult to explain by a dissolution model [140, 141].

Further, Winzer et al. [111] characterized the fracture surface of AZ91 tested in distilled water by constant extension rate test (CERT) and found distinctive features of the cleavage fracture, i.e. fine parallel markings (Fig. 2.16a) and cleavage induced by  $\beta$  phase (Fig. 2.16b).

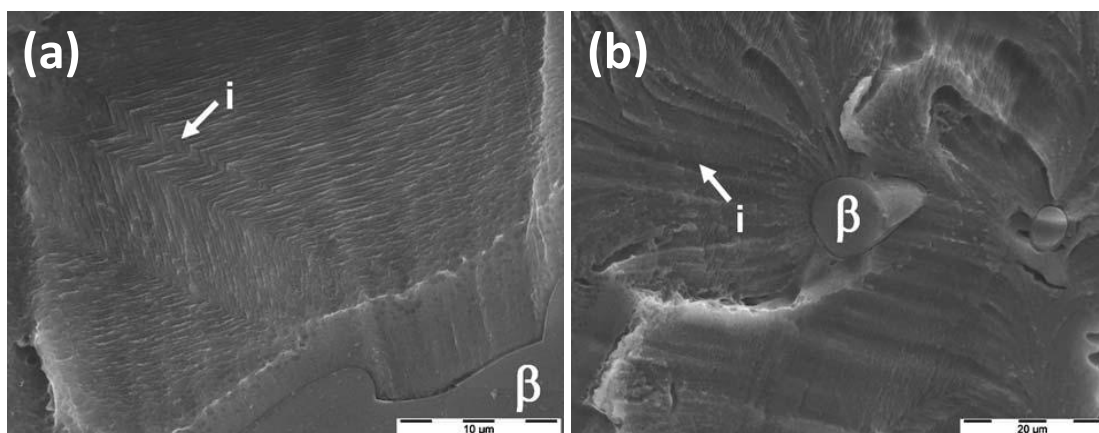


**Fig. 2.16.** Fracture surface for AZ91 specimen tested in distilled water under CERT conditions showing: (a) fine parallel markings (i) and (b) cleavage through  $\beta$  particles [111]

## **b) Hydrogen embrittlement (HE)**

The TGSCC observed in Mg alloys has been widely attributed to mechanism involving hydrogen (H). In literature, the possible mechanisms for hydrogen embrittlement of metal and alloys include H enhanced decohesion (HEDE), H enhanced localized plasticity (HELP), adsorption-induced dislocation emission (AIDE) and delayed hydride cracking (DHC) [142].

Meletis and Hochman [116] reported concurrent H evolution during crack initiation and crack propagation stages for pure Mg in a chloride-chromate solution. Further, the occurrence of cleavage fracture surfaces also suggested that the cracking may be a form of HE. Also, the authors proposed that H may be absorbed from the solution at the crack tip or may be transported by dislocation motion. This mechanism involved the discontinuous build up of stress followed by hydrogen transport to the stressed area, subsequently resulting in cleavage.

Chen et al. [143] investigated the effects of hydrogen on SCC of as-cast AZ91 in Na<sub>2</sub>SO<sub>4</sub> solution using SSRT testing and reported a significant decrease in mechanical properties of the alloy with cathodic charging. This decrease in mechanical properties was attributed to the enhanced role of hydrogen, which diffused into the matrix and accumulated at the  $\beta$  phase, and subsequently formed hydride that cracked under applied stress.

Uematsua et al. [118] also showed that the SCC of wrought AZ31 magnesium alloy was dominated by hydrogen embrittlement. They reported lower  $K_{ISCC}$  value and higher crack propagation rate with greater magnitude of cathodic potential that facilitated generation of hydrogen.

In contrast, even anodic polarization accelerated the SCC in Mg alloys, which could be explained on the basis of negative difference effect [35, 36, 118]. Ebtehaj et al. [113] showed that large amount of H was evolved with anodic polarization and reported that cracking

invariably started at the regions of localized pitting, suggesting the role of pitting in allowing H ingress into metal.

Dietzel et al. [110] has attempted to simulate the experimental SCC results obtained by CERT testing on the AZ91 alloy in distilled water using a mesoscale fibre bundle model. They studied the effect of hydrogen embrittlement on the stress–strain curves measured at various strain rates and simulated the experimental results with an assumption that the hydrogen is generated in localized corrosion pits that subsequently diffused into the bulk, thereby reducing the strain-to-failure. The stress–strain curves obtained from these simulations showed the same strain rate effect that was experimentally observed. In an another recent study by Kannan et al. [108] on the SCC of AZ80 in distilled water and 0.5 wt. % NaCl, it was shown that the pitting susceptibility of the alloy played a crucial role in the SCC and HE behaviour of the alloy.

Based on above discussion, it is noted that the inhibition of pitting corrosion will help in preventing the HE of Mg alloys. It is further suggested that the pitting corrosion represents the initiation stage of transgranular cracking of Mg-Al alloys. Nevertheless, it is clear that the role of pits is to provide a bare, film-free and active Mg surface through which atomic H can enter to embrittle the metal matrix, and cause cracking.

## **2.6 SCC of magnesium alloys: in biomaterials perspective**

Mechanical and chemical stability of implanted materials in the physiological environment are of fundamental importance in successful treatment of fracture fixations and cardiovascular surgeries. Metallic implant devices exposed to the corrosive physiological environment are often also subjected to acute loadings during service. For example, a hip implant can experience a load up to approximately four-times of the body weight during a normal walk, whereas a cardiovascular stent is continuously subjected to a cyclic loading due to heart beats [26, 144]. For an adult, loads in the spine during certain activities may exceed 3500 N [68].

The synergistic presence of the mechanical loading along with the corrosive environment may pose complication of sudden brittle fracture of implants due to the phenomenon of SCC [101, 127]. These brittle stress corrosion cracks generally initiate at locations of sharp contours such as root of a corrosion pit. Furthermore, pre-existing macro/microscopic flaws (e.g. micro-cracks, sharp corners and protrusions in implant devices) can markedly increase the probability of premature SCC failures and can be locations of SCC initiation. Moreover, the load bearing implant devices are becoming relatively complex in design, thus also increasing the number of high stress intensity points in an implant device. Furthermore, galvanic, localized or intergranular corrosion, and even thinning by uniform corrosion, could initiate SCC in biomaterials [35].

Stress corrosion cracks may propagate undetected to a sudden catastrophic failure of implant devices during service, which may have many serious consequences such as painful irritation or inflammation of surrounding tissues, and troublesome removal of failed devices. In past, several incidents involving SCC and corrosion fatigue of traditional implant devices of stainless steels and titanium alloys have been reported [20, 21, 145-149].

In this context, it is also important to note that Mg alloys are reported to be susceptible to SCC in aqueous environments, including distilled water and chloride solutions [105]. Hence, characterization of SCC of biomedical magnesium alloys in the physiological conditions will be of great importance before their actual service use. However, a very limited attention has been paid on the evaluation of mechanical integrity/SCC of Mg alloys in the body fluid. There have been only a few in-vitro studies concerning SCC of Mg alloys in the modified-simulated body fluid (*m*-SBF) [16, 27, 31, 79]. In a preliminary investigation, Kannan et al. [79] reported decrease in mechanical strength and ductility of AZ91 in the *m*-SBF solution during SSRT testing. In extension of this work, they also carried out an investigation into mechanical integrity of notched specimens [27]. Results of CERT tests on notched specimens and analysis of the fracture surfaces revealed significant SCC susceptibility of the AZ91 alloy. It was found

that the mechanical integrity of the AZ91 in *m*-SBF was dependent on the design of the specimen, and the presence of a notch substantially decreased the mechanical integrity in *m*-SBF. However, the mechanistic understanding of SCC of Mg alloys in the physiological environment has not been explored in these preliminary investigations.

For an alloy conducive to SCC, it is also extremely important to determine the important design parameters, e.g.  $K_{ISCC}$  and crack growth rates, for predicting the life of an alloy exposed to the corrosive body fluid. However, such studies have not been reported for biodegradable Mg alloys. In fact, it is yet to be established whether the novel Mg alloys, specifically developed for implant applications, possess desired resistance to SCC in the physiological environment.

## **2.7 Prevention of SCC**

There are some recommendations to avoid SCC in practices, which are discussed below.

### **1) Selection of SCC resistant alloy**

SCC can be avoided by using high-purity alloys/metals or by replacing SCC-prone material in that service environment with more SCC resistant alloy. The SCC resistant alloys can be produced by wise selection of alloying additions. For example, Mg alloys with higher concentration of Al are more susceptible to SCC, while Mg-Zn alloys have an intermediate susceptibility to SCC [67]. Addition of zirconium (Zr) and rare earths (RE) as alloying elements have been reported to increase the SCC resistance [67].

### **2) Control of stress**

The working stress endured by the alloy in service conditions must be kept below a critical level, which has been reported to be 30 to 50 % of the tensile yield strength of the material. Also, a great importance should be given to the use of simple shapes that will provide less

of local high stress generating points. Bolted and riveted joints can produce point of high stress concentrations, suggesting the importance of proper joint design. Although, sometime it is not possible to control the service stresses, however, stress concentration points can still be reduced by use of smooth geometries [35].

### **3) Surface modifications and coatings**

Coatings may be an appropriate measure for preventing the SCC to some extent, if not completely. As discussed, the localized and pitting corrosion are common cause for initiation of SCC in Mg alloys. Accordingly, the coating, which may reduce the pitting propensity in the corrosive environment, could also help in avoiding the SCC to some extent [67].

Control of stresses and environment are not practical in biomedical applications since implants are expected to work under given stress conditions in the blood plasma. Nevertheless, the development of SCC-resistant Mg alloys could be one of the preventive measures. Accordingly, alloying composition could be chosen by taking SCC resistance into account in developing Mg alloys for biomedical applications. But the alloys should also be non-toxic, which limits the choices of alloying elements. Therefore, there is a value in exploring SCC mitigation with the use of biocompatible coatings on Mg alloys.

## **2.8 Biocompatible coatings for corrosion/SCC resistance**

Surface engineering by application of coatings is a common approach to improve surface properties such as corrosion resistance while still maintaining the bulk mechanical properties of an engineering alloy. As mentioned in Sections 2.2-2.5, Mg/Mg alloys corrode very rapidly in physiological solutions. Therefore, most studies on Mg alloys concerning their use as biodegradable implants have aimed at improving their corrosion resistance in blood plasma [23, 31, 150-152]. Till now, several methods have been investigated for improving the



corrosion resistance of Mg alloys in physiological environments (for example, new alloy development [29, 30, 153], ion implantations [154, 155], coatings [156-161], composites [162-164] and laser surface modifications [165]).

Various coating methodologies, such as ion beam assisted deposition, plasma spray deposition, pulsed laser deposition, physical vapour deposition, magnetron sputtering, sol–gel derived coatings, electrodeposition and micro-arc oxidation, have been used and studied for developing biocompatible coatings. This section briefly discusses the role of most common biocompatible coatings derived from conventional conversion route and electrodeposition in improving the corrosion/SCC behaviour of Mg alloys in physiological solutions.

### **2.8.1 Calcium-phosphate (Ca-P) coatings**

Calcium (Ca) and phosphorous (P) are the main elements present in bone minerals [51]. Calcium phosphate (Ca-P)-based bioceramic coatings have been widely used on Mg alloys because of the associated advantages of biocompatibility, osteoconductivity and reduced degradation rate [25, 166, 167]. In past, surface tailoring by Ca-P coatings has also been used for improving biocompatibility of titanium or titanium-based alloys [168, 169].

Some of the Ca-P compounds of biomedical interest mainly include dicalcium phosphate [ $\text{CaHPO}_4 \cdot 2\text{H}_2\text{O}$ , DCPD], octacalcium phosphate [ $\text{Ca}_8(\text{HPO}_4)_2(\text{PO}_4)_4 \cdot 5\text{H}_2\text{O}$ , OCP], tricalcium phosphate [ $\text{Ca}_3(\text{PO}_4)_2$ , TCP] and hydroxyapatite [ $\text{Ca}_{10}(\text{OH})_2(\text{PO}_4)_6$ , HA]. HA is considered to be thermodynamically most stable in the physiological environment. OCP and DCPD, however, have been identified as precursors for facilitating kinetics of HA formation as well as for other metastable Ca-P phases [170, 171].

Among several methods for depositing Ca-P coating, electro-deposition, conversion and biomimetic precipitation routes are simple and inexpensive processes that can be carried out at low temperatures. Moreover, the thickness and chemical composition of the Ca-P coatings can also be controlled by adjusting coating bath chemistry. In addition, these coating methods also provide distinct advantages such as: (i) ease of operation, (ii) low-cost, and (iii) ability to coat the complex structures such as screws, stents and pins [167].

Previously, a few researchers electro-deposited the Ca-P coating on various Mg alloys, and also reported a distinct decrease in corrosion rate [31, 166]. Recently, Song et al. [166] showed that the calcium phosphate coating on AZ31 developed at room temperature could significantly improve the corrosion resistance, which might allow implants to maintain their mechanical integrity during bone-healing phase.

Although it has been reported that the Ca-P coatings on Mg alloys improve the corrosion resistance and biocompatibility, it appears unlikely that it will improve SCC resistance at the same time. Since Ca-P coating (a ceramic) is brittle in nature, it may break/crack during the load bearing conditions, thus exposing the substrate and accelerating the localized corrosion/pitting, which may even worsen the SCC resistance. Accordingly, it is essential to investigate the other biocompatible coating system, which may improve the corrosion/SCC resistance as well as enhance biocompatibility.

### **2.8.2 Novel graphene-calcium carbonate coating**

The two most abundantly studied bio-minerals are the calcium carbonate ( $\text{CaCO}_3$ ) and hydroxyapatite (HA). The synthesis of hybrid materials with the use of bio-mineral is highly required in biomedical applications in order to improve the biocompatibility and osteoinductivity.

Graphene ( $sp^2$ -bonded carbon sheet with a thickness of single atom) has recently received attention of materials scientists and physicists because of its unique qualities, which include excellent thermal, mechanical and electrical properties [172]. Besides these attributes, graphene also possesses the chemical inertness [173] and hydrophobicity [174], which makes it an ideal candidate for corrosion inhibiting coatings. Recently, there have been a few reports on improvement of corrosion resistance of Cu and Ni by the application of graphene coatings [175-177], which were epitaxially grown using chemical vapour deposition (CVD) at 800-1000 °C. But, the low melting point of Mg and its alloys does not allow the use of CVD to grow graphene on Mg alloys.

Graphene has found several applications in the fields of electronics and composite materials, and has been vigorously researched in last decade. However, hybridization or interaction of graphene with biominerals to form biocompatible coatings on metals and/or alloys has received limited attention. In a very recent study, Kim et al. [178] have synthesized self standing graphene- $CaCO_3$  film, which showed very high in-vitro bone bioactivity after exposure to the body fluid. The deposition of this film as a coating on biomedical Mg alloys may provide improved corrosion resistance and biocompatibility. It is also reasonable to infer that the presence of mechanically strong dispersed graphene network, which promotes the formation of the thermodynamically most unstable phase of  $CaCO_3$ , i.e. vaterite [179], may help in improving the corrosion resistance (and hence, possibly the SCC resistance) in physiological environment.

## 2.9 Research problems and objectives

As discussed in this chapter, Mg alloys have emerged as potential candidates for construction of biodegradable temporary implant devices owing to their excellent biocompatibility, favourable mechanical properties and biodegradability. At the same time, they are also highly susceptible to corrosion in the physiological environment. Furthermore, rapid corrosion of Mg alloys in physiological environment is accompanied by excessive hydrogen evolution. More importantly, implants will also experience mechanical loading in presence of aggressive physiological environment that can cause environmentally assisted cracking, i.e. stress corrosion cracking (SCC). It is therefore essential to evaluate the mechanical integrity/SCC behaviour of biodegradable magnesium alloys before employing them in service. However, very limited attention is paid to the evaluation of SCC and determination of important design parameters (for example, threshold stress intensity for SCC ( $K_{ISCC}$ ) and crack growth rates) for biodegradable Mg alloys. In addressing the SCC of Mg alloys for implant application, there is a need for investigating certain aspects as discussed below:

### ***Objective 1:***

#### ***SCC of non-toxic, biocompatible and biodegradable magnesium alloys***

Most of the commercial Mg alloys contain Al as the main alloying element. Since Al is well known as neuro-toxicant and causes various neurological disorders [180], the Al-containing magnesium alloys may not be used in biomedical applications. Accordingly, a few novel Al-free biodegradable high strength magnesium alloys (ZX50 and WZ21) were developed at ETH, Zurich for potential applications as cardiovascular stents and temporary implants in osteosynthesis. However, the development of these alloys did not take their resistance to SCC in human body fluid into account, and this study therefore aims to investigate and evaluate the SCC resistance of these novel alloys in the physiological environment.

## ***Objective 2:***

### ***Mechanistic understanding of SCC of magnesium alloys in the physiological environment***

Mg alloys are highly susceptible to corrosion and forms a poorly passivating film that may facilitate SCC by dissolution mechanism. Mg alloys also produce hydrogen during both anodic and cathodic corrosion reactions that may facilitate hydrogen embrittlement. It is hypothesized that Mg alloys may undergo SCC by both dissolution and hydrogen embrittlement mechanisms, but the contributions of the two may vary from alloy-to-alloy. Most SCC studies on Mg alloys have been conducted on Al-containing AZ series alloys. Therefore, this study will first investigate the possibility of dissolution and hydrogen embrittlement mechanisms for a common alloy, AZ91D. Then, these mechanisms will be investigated also for the Al-free magnesium alloys identified through Objective 1 above. In addition, this study also attempts to determine the most important design parameters,  $K_{ISCC}$  and crack growth rates, for AZ91D alloy in the physiological environment.

## ***Objective 3:***

### ***Improved corrosion/SCC resistance by application of a novel biocompatible coating***

Localized corrosion and/or pitting are the prime factor in causing SCC of the Mg alloys in aqueous environments. If a suitable biocompatible coating that suppresses the localized corrosion/pitting of Mg alloys in physiological solution is found, the mechanical integrity of biodegradable Mg alloys could be improved. Accordingly, this thesis also aims to develop an economical route for depositing novel graphene- $\text{CaCO}_3$  coating on the magnesium alloy, AZ91D. It is hypothesized that strong mechanical network of graphene that favour the formation of thermodynamically unstable form of  $\text{CaCO}_3$  (i.e. vaterite), which subsequently transform into hydroxyapatite during exposure to the body fluid, may

actually help in decreasing the localized corrosion/pitting susceptibility, thereby improving the SCC resistance.



## Chapter 3

### 3. Experimental principles and procedures

The evaluation of stress corrosion cracking (SCC) of biomedical magnesium alloys is of great importance as described in the literature review (Chapter 2). Research objectives have been accordingly identified, as also described in Chapter 2. To achieve these objectives, a few experimental protocols have been followed. This chapter describes general experimental procedures and details.

#### 3.1 Test materials and environment

A few as-cast and wrought magnesium alloys have been characterized in this study for their resistance to SCC in the physiological environment. The most common aluminum (Al)-containing Mg alloy, AZ91D, was received in sand-cast form. The chemical composition of AZ91D is shown in Table 3.1, as measured by the Spectrometer Services Pty Ltd.

Table 3.1: Chemical composition of AZ91D

Element	Mg	Al	Zn	Mn	Fe	Ce	Si	Cu
Wt. %	Bal.	8.81	0.79	0.21	0.003	< 0.01	< 0.01	0.003

Another as-cast Mg alloy, Mg<sub>3</sub>Zn<sub>1</sub>Ca, was produced by induction melting of high purity Mg, Zn and Ca in a steel mould crucible under an argon atmosphere and casting. The ZX50, WZ21 and WE43 Mg alloys were received from ETH Zurich and investigated in their as-received extruded conditions. The ZX50, WZ21 and WE43 magnesium alloys were produced by direct chill casting using magnesium and alloying elements (purity  $\geq 99.9\%$ ). The



elements were melted in an electric furnace at ~ 690 °C and subsequently cast at a velocity of 1.3 mm/s with continuous water cooling. All alloys were evaluated in their as-extruded conditions. The extrusion ratio was 30:1 for WZ21 and ZX50, while 25:1 for WE43 [32, 153, 181]. The nominal chemical composition of each of the Al-free Mg alloy is provided in Table 3.2.

Table 3.2: Nominal chemical composition (in wt. %) of Mg alloys used in this study

Alloy	Mg	Zn	Zr	Ca	Mn	Y	Nd	Al	Other RE
Mg3Zn1Ca	Bal.	3	-	1	-	-	-	-	-
ZX50	Bal.	5	-	0.25	0.15	-	-	-	-
WZ21	Bal.	1	-	0.25	0.15	2	-	-	-
WE43	Bal.	-	0.6	-	0.15	4	2.25		1

All the SCC and electrochemical experiments were performed in the physiological environment of modified simulated body fluid (*m*-SBF). Till now, several simulated physiological solutions have been used to carry out in-vitro assessments of Mg alloys, such as Hanks' solution, Ringer's solution and simulated body fluids (SBF). In recent times, a few studies have aimed at revising the simulated body fluids. The new SBFs (such as *m*-SBF) have ion concentrations much closer to the blood plasma [182]. Oyane et al. [182] reported that *m*-SBF showed no change in ion concentrations and pH for periods up to 8 weeks under sealed storage, and concluded that *m*-SBF has an optimum ion concentration for in-vitro assessments. A comparison of the *m*-SBF solution used in this study with the Hank's solution, original SBF and human blood plasma is provided in Table 3.3. The table shows the chemical nature of *m*-SBF solution to be largely identical to that of blood plasma, except for the concentration of  $\text{HCO}_3^-$ , which was set to the saturation level with respect to calcite. The *m*-SBF solution was buffered with 2-(4-(2-hydroxyethyl)-1-piperaziny) ethansulfonic acid (HEPES) at a physiological pH of 7.4.

In contrast, the original simulated body fluid (SBF) prepared by Kokubo et al. [183], which is buffered using tris(hydroxymethyl)aminomethane (TRIS), has a  $\text{HCO}_3^-$  ion concentration of only 4.2 mM (in contrast to the concentration of 27 mM in human blood plasma), and excess of  $\text{Cl}^-$  concentration (148 mM in comparison to 103 mM in human blood plasma). The original SBF solution prepared by Kokubo is thus considerably carbonate-deficient as well as chloride-rich, which does not mimic the human blood plasma appropriately. These vast differences in ion concentrations may result in erroneous in-vitro results, particularly since the chloride concentration profoundly affects the corrosion kinetics of magnesium alloys [184, 185].

Table 3.3: Chemical composition of *m*-SBF solution compared with Hanks' solution, original SBF prepared by Kokubo and the inorganic portion of human blood plasma

Ion	<i>m</i> -SBF (mM) [182]	Hanks' solution (mM) [70]	Original SBF [183]	Blood plasma (mM) [182, 186]
$\text{Na}^+$	142	142	142.0	142
$\text{K}^+$	5.0	5.8	5.0	5.0
$\text{Mg}^{2+}$	1.5	0.8	1.5	1.5
$\text{Ca}^{2+}$	2.5	2.5	2.5	2.5
$\text{Cl}^-$	103	145	148.8	103
$\text{HCO}_3^-$	10	4.2	4.2	27
$\text{HPO}_4^{2-}$	1.0	0.3	1.0	1.0
$\text{SO}_4^{2-}$	0.5	0.8	-	0.5
Buffer	HEPES	TRIS	TRIS	-

## 3.2 Stress corrosion cracking testing

### 3.2.1 Slow strain rate tensile (SSRT) testing

The SCC susceptibility of the magnesium alloys in *m*-SBF was investigated using slow strain rate tensile (SSRT) testing. The test solution of *m*-SBF was maintained at a nominal body temperature of 37 °C throughout the experiment. This study used round tensile specimens with the gauge dimensions of 20 mm (length) and 3 mm (diameter), as shown in Fig. 3.1. Gauge sections of these specimens were ground with SiC paper up to 2500 grit, and cleaned with acetone and deionised water prior to the testing.

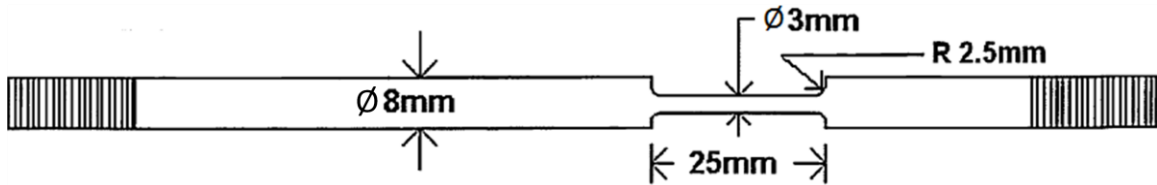


**Fig. 3.1.** Geometry and dimensions of a SSRT specimen

Fig. 3.2 shows the details of the experimental set-up for the SSRT testing. In SSRT testing, strain rate is a critical parameter and reported to have profound role on the SCC susceptibility of Mg alloys (Section 2.5.2.1). The literature reports that strain rates in the range of  $10^{-7} \text{ s}^{-1}$  render magnesium alloys susceptible to SCC in chloride solutions [18, 19, 35]. Different strain rates were achieved by employing different fractions (15-40 %) of full speed of the motor of the SSRT rig (Table 3.4).

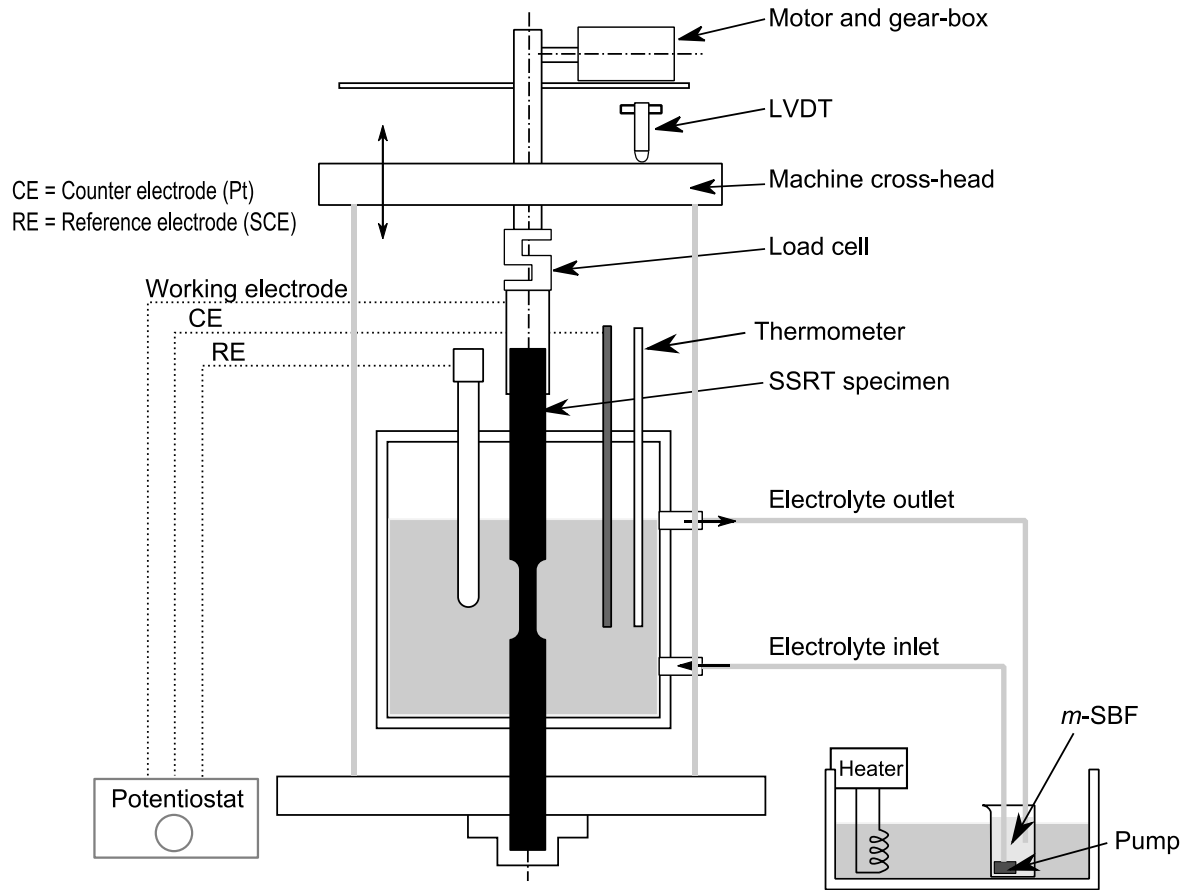


**Fig. 3.2.** Schematic of the experimental set-up of SSRT rig

Table 3.4: Different strain rates corresponding to the different motor speeds of the SSRT rig

Motor speed (%)	Strain rate ( $s^{-1}$ )
40	$5 \times 10^{-7}$
35	$4.3 \times 10^{-7}$
30	$3.1 \times 10^{-7}$
25	$2.2 \times 10^{-7}$
15	$1.2 \times 10^{-7}$

In the present study, specimens were pulled at different strain rates in the regime of  $10^{-7} s^{-1}$ . During the SSRT tests, the exposed area of the test specimen was restricted to the gauge length by wrapping the rest of the specimen with Teflon tape, thus maintaining a constant area for exposure to the corrosive solution and avoiding galvanic effects. Also, to simulate the flowing

body fluid, a submersible pump was used to continuously circulate the *m*-SBF through a corrosion vessel of the SSRT set-up, in which the test specimen was immersed, as shown in Fig. 3.2. The circulation of the *m*-SBF solution using a water bath maintained a temperature of 37 °C (which is similar to the human body temperature). This arrangement also avoided localized change of the pH in the vicinity of the test specimen throughout the experiment. All the SSRT experiments were performed in duplicate to examine the reproducibility.

The characterization of SCC susceptibility of magnesium alloys is a considerable challenge. To address this complication, two carefully selected mechanical parameters have been compared in this study, before inferring the SCC. These parameters are: ultimate tensile stress (UTS) and elongation-to-failure ( $\epsilon_f$ ) in *m*-SBF and air environment. The SCC susceptibility of each alloy was established on the basis of the SCC susceptibility index ( $I_{SCC}$ ). The  $I_{SCC}$  is the ratio of  $\epsilon_f$  or UTS measured in a corrosive environment (*m*-SBF solution) to the corresponding value in an “inert” environment (air). The SCC susceptibility index ( $I$ ) are defined in Equations 3.1 and 3.2 [18].

$$I_{UTS} = \frac{UTS \text{ in } m-SBF}{UTS \text{ in air}} \quad (3.1)$$

$$I_{\epsilon} = \frac{\epsilon \text{ in } m-SBF}{\epsilon \text{ in air}} \quad (3.2)$$

When the value of a susceptibility index ( $I$ ) approaches unity, it is assumed that the material is highly resistant to the SCC in a given environment. However, the smaller the value of the index (than 1), the greater is the susceptibility to SCC.

To carry out investigations to distinguish the dissolution and hydrogen embrittlement mechanisms of SCC, separate SSRT experiments were carried out under imposed electrochemical potentials. Facility for imposed potential SSRT experiments is also shown in Fig. 3.2. During imposed potential SSRT testing, specimens were continuously charged cathodically at a constant potential of 200 mV (vs. saturated calomel electrode (SCE)) negative

to the open circuit potential using a potentiostat, while straining the specimens simultaneously in *m*-SBF. A conventional 3-electrode cell, with a platinum mesh as the counter electrode, a SCE as the reference electrode and the SSRT specimen as the working electrode, was used. Anodic dissolution of the alloys was assumed to be minimal at the applied cathodic potential during cathodic charging SSRT experiments.

### **3.2.2 Circumferential notch tensile (CNT) testing**

A novel fracture mechanics-based technique, i.e. circumferential notch tensile (CNT) testing, was used in this study for determination of threshold stress intensity of SCC ( $K_{ISCC}$ ) and crack growth rates of AZ91D in *m*-SBF at 37 °C. Round tensile specimens, with 9.5 mm diameter and a sharp 60° “V” shape notch in middle, was used, as shown in Fig. 2.13.

#### **3.2.2.1 Fatigue pre-cracking using rotating bending machine**

For generating  $K_{ISCC}$  data, the CNT specimens need to be fatigue pre-cracked to generate sharp enough cracks to satisfy constraints of LEFM (discussed in Section 3.2.2.4).

The CNT specimens were fatigue pre-cracked using a cantilever-type rotating bending fatigue machine. The specimen was held by a collet chuck on one side which was connected directly with a motor through a shaft supported by a pair of bearing. The pre-cracking of CNT specimens was conducted at a rotating speed of 2800 rpm and an applied pneumatic pressure of ~200 kPa (at the free end of the specimen). The size of fatigue pre-crack is determined after the specimen failure. However, during the rotating-bending operations, a linear variable displacement transformer (LVDT) was used to measure the deflection at the point where load was applied. Through trial-and-error, it was established that a deflection of 0.018 mm (shown on a digital display) was sufficient to produce a fatigue pre-crack that will satisfy the valid plane strain conditions.

### 3.2.2.2 Measurement of eccentricity

One of the critical issues in accurate determination of stress intensity ( $K_I$ ) by the CNT method is possible effect of the eccentric final ligament produced during fatigue pre-cracking of specimens by rotating/bending. As shown in Fig. 3.3, the ligaments are elliptical and off-center due to the insufficient isotropy in fatigue characteristics of the material. When the ligament is off-center, the final fracture of the specimen will not only result from tension force but will also have a component of the bending force. Therefore, effect of the eccentricity must be taken into account for accurate calculation of the  $K_I$ .

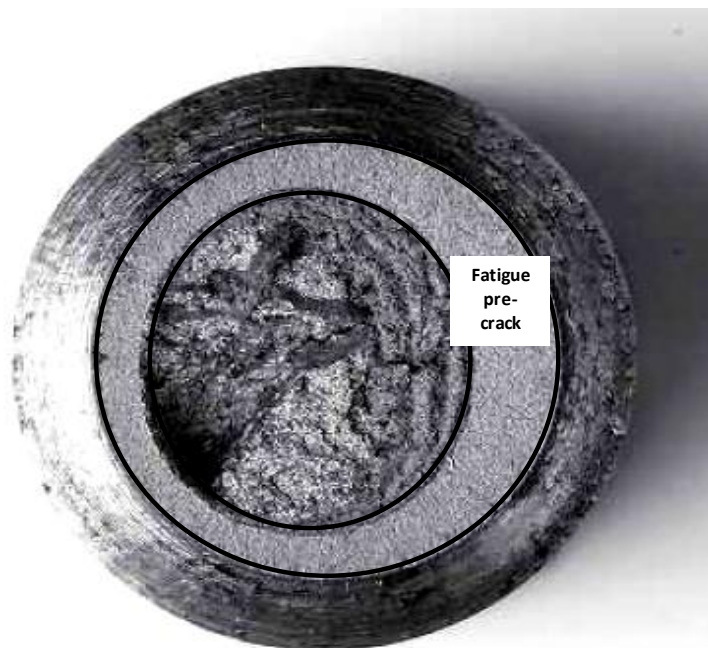


**Fig. 3.3.** Eccentricity of the final ligament after fatigue pre-cracking [124]

To calculate the eccentricity, twelve measurements of fatigue crack depth ( $a_f$ ) and the machined groove depth ( $a_m$ ) were measured at  $30^\circ$  intervals, using a profile projector (Fig. 3.4).

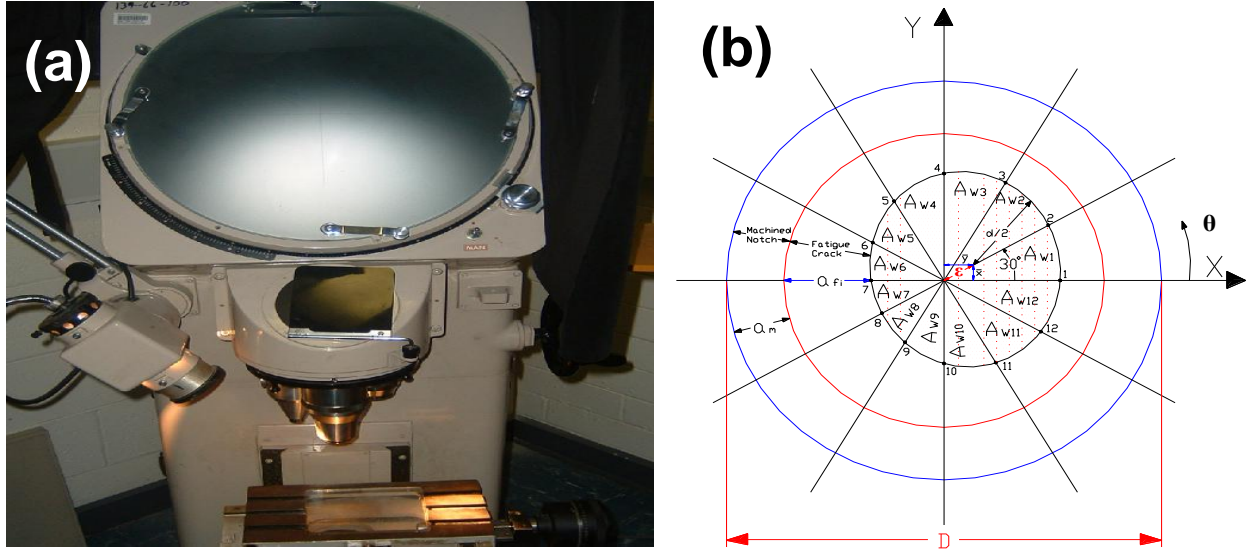


**Fig. 3.4.** (a) Profile projector and (b) eccentricity measurement of the final ligament [124]

Area of every wedge ( $A_{wi}$ ) of  $30^\circ$  is calculated using the Equation 3.3.

$$A_{wi} = \frac{\pi}{12} (0.5D - a_{fi} - a_m)^2 \quad (3.3)$$

Total ligament area can be given by Equation 3.4:

$$A = \sum_{i=1}^{12} \frac{\pi}{12} (0.5D - a_{fi} - a_m)^2 \quad (3.4)$$

After calculation of total ligament area, the diameter of ligament can be calculated using Equation 3.5.

$$d = \sqrt{\frac{4A}{\pi}} \quad (3.5)$$

The first moments of area of a  $30^\circ$  wedge about the  $X$  and  $Y$  axes, respectively, are calculated using Equations 3.6 and 3.7:

$$M_{xi} = \frac{\pi}{18} (0.5D - a_{fi} - a_m)^3 \sin \theta \quad (3.6)$$



$$M_{yi} = \frac{\pi}{18} (0.5D - a_{fi} - a_m)^3 \cos \theta \quad (3.7)$$

Hence, the total moment of all the wedges about X and Y axes can be calculated using Equations 3.8 and 3.9.

$$M_x = \sum_{i=1}^{i=12} \left( \frac{\pi}{18} (0.5D - a_{fi} - a_m)^3 \sin \theta \right) \quad (3.8)$$

$$M_y = \sum_{i=1}^{i=12} \left( \frac{\pi}{18} (0.5D - a_{fi} - a_m)^3 \cos \theta \right) \quad (3.9)$$

The X and Y coordinates of the centroid of the ligament have been obtained using Equations 3.10 and 3.11.

$$\bar{X} = \frac{\sum_{i=1}^{i=12} \left( \frac{\pi}{18} (0.5D - a_{fi} - a_m)^3 \sin \theta \right)}{\sum_{i=1}^{i=12} \frac{\pi}{12} (0.5D - a_{fi} - a_m)^2} \quad (3.10)$$

$$\bar{Y} = \frac{\sum_{i=1}^{i=12} \left( \frac{\pi}{18} (0.5D - a_{fi} - a_m)^3 \cos \theta \right)}{\sum_{i=1}^{i=12} \frac{\pi}{12} (0.5D - a_{fi} - a_m)^2} \quad (3.11)$$

Therefore, the eccentricity ( $\varepsilon$ ) can be calculated using Equation 3.12.

$$\varepsilon = \sqrt{\bar{X}^2 + \bar{Y}^2} \quad (3.12)$$

### 3.2.2.3 Calculation of applied stress intensity ( $K_I$ )

After fatigue pre-cracking, specimens are loaded at different constant stresses. They fail after different time durations. Using data from the fractured surface of the specimen after failure (fatigue crack and machined notch depth), the stress intensity ( $K_I$ ) is determined by the following relationships (Equations 3.13 to 3.19):

$$K_I = (\sigma_t + \sigma_b) \sqrt{a \pi F_o} \quad (3.13)$$

$$a = \frac{D - d}{2} \quad (3.14)$$

$$\sigma_t = \frac{4P}{\pi D^2} \quad (3.15)$$

$$\sigma_b = \frac{16P\varepsilon}{\pi D^3} \quad (3.16)$$

$$F_o = F e^{\alpha(\varepsilon/D)} \quad (3.17)$$

$$F = \frac{1.25}{[1 - (2a/D)^{1.47}]^{2.4}} \quad (3.18)$$

$$\alpha = 22.188 e^{-4.889 \left( \frac{2a}{D} \right)} \quad (3.19)$$

where,

$P$  is the tensile force applied to specimen (N)

$D$  is the specimen outside diameter (m),

$d$  is the equivalent diameter of final ligament area (m),

$\sigma_t$  is the tensile stress applied to the specimen (Pa),

$\sigma_b$  is the bending stress induced by the eccentricity of the ligament (Pa),

$\varepsilon$  is the eccentricity (m),

$a$  is the effective crack depth (m),

$F_o$  is the geometrical function depending upon the geometry of fatigue crack

$F$  is the geometrical function for round specimen without eccentricity and,

$\alpha$  is a constant

The first estimate of  $K_I$  is obtained by using the effective crack length ( $a$ ) in Equation 3.13. This estimate of  $K_I$  is used to get the Irwin correction factor ( $r_y$ ) from Equation 3.20 and  $\bar{a}$  from Equation 3.21, and hence, the final  $K_I$  is calculated using  $\bar{a}$  in place of  $a$ .

$$r_y = \frac{1}{6\pi} \left( \frac{K_I}{\sigma_y} \right)^2 \quad (3.20)$$

$$\bar{a} = a + r_y \quad (3.21)$$

where,  $\sigma_y$  is the 0.2 % offset tensile yield stress (Pa).

#### 3.2.2.4 Validity requirement for $K_I$ measurements

The data generated with CNT technique comply with the principles of linear elastic fracture mechanics (LEFM). LEFM is applicable with the assumption that the crack propagate in elastic brittle manner. The LEFM approach is only valid if the size of plastic zone ahead of the crack tip is negligible as compared to the specimen geometry. Therefore, specifications for examining the validity of measured  $K_I$  have been developed for CNT specimens [131, 187].

The validity requirements for calculating the  $K_I$  values are expressed in Equations 3.22 to 3.24.

**First criteria:** The deepest fatigue crack ( $a_f$ ) must be at least twice the Irwin correction factor ( $r_y$ ) in order to fully develop the required plane strain conditions.

$$a_f \geq 2r_y \quad (3.22)$$

where,

$$a_f = \varepsilon + \frac{(D - 2a_m - d)}{2} \quad (3.23)$$

**Second criteria:** Stress applied on the specimen must not be greater than 2.5 times the tensile yield strength of the material.

$$\frac{\sigma_N}{\sigma_y} \leq 2.5 \quad (3.24)$$

### 3.2.2.5 Determination of $K_{ISCC}$

The time-to-failure ( $t_f$ ) is obtained at different  $K_I$  for specimens of the same material under same experimental conditions. A  $K_I$  vs.  $t_f$  plot enables the determination of  $K_{ISCC}$  (which is the minimum stress intensity required for the crack initiation in a given corrosive environment), as shown in Fig. 3.5 [132]. Therefore, the tested metal or alloy is considered resistant to SCC at the  $K_I$  values lower than the  $K_{ISCC}$ .

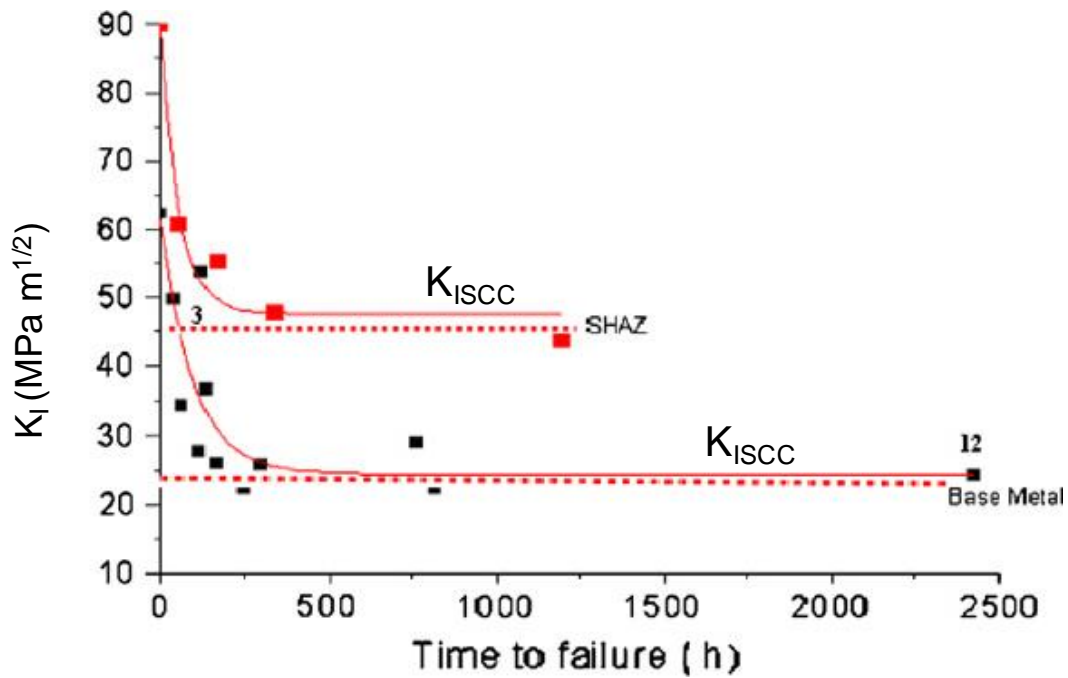


**Fig. 3.5.** Determination of  $K_{ISCC}$  of base metal and simulated heat affected zone (SHAZ) of grade 250 steel in 30 % caustic solution at 100 °C (asymptote to the time to failure axis in  $K_I$  vs. time to failure plot gives the  $K_{ISCC}$  value)

### 3.2.2.6 Determination of crack growth rate

An average crack growth rate is generally determined by measuring the longest crack and dividing it by the time-to-failure for the particular specimen. However, crack growth rate determination by this method assumes that the crack initiates at the start of the test, which is not necessarily the case. In this study, crack growth rate was determined by using the Equation 3.25:

$$\frac{da}{dt} = \frac{dK_I}{dt} \frac{da}{dK_I} \quad (3.25)$$

where, a is effective crack length in m and t is time in h.

The term  $\frac{dK_I}{dt}$  of Equation 3.25 is determined from the relationship between  $K_I$  and time-to-failure, whereas the term  $\frac{da}{dK_I}$  can be determined from the relationships for deriving  $K_I$  [130].

### 3.2.3 Fractography

Fractography is generally performed to characterize the failure modes. The most typical features of ductile failure due to mechanical overloading are dimples (Fig. 3.6a), whereas SCC is exclusively characterized by brittle failure in transgranular (Fig. 3.6b) and/or intergranular (Fig. 3.6c) fashion. It is typical of an alloy susceptible to SCC that the crack first propagates in transgranular and/or intergranular mode. Once a critical SCC crack length is achieved, mechanical overloading (ductile failure) takes over in the final stage of cracking.

In the present study, to examine the presence of SCC (i.e. intergranular/transgranular modes), fractography was performed on the fractured surfaces using JEOL 840A scanning electron microscope (SEM). Before fractography, fracture surface was cleaned using 20 wt. %  $\text{CrO}_3$  and 10 wt. %  $\text{AgNO}_3$  solution.

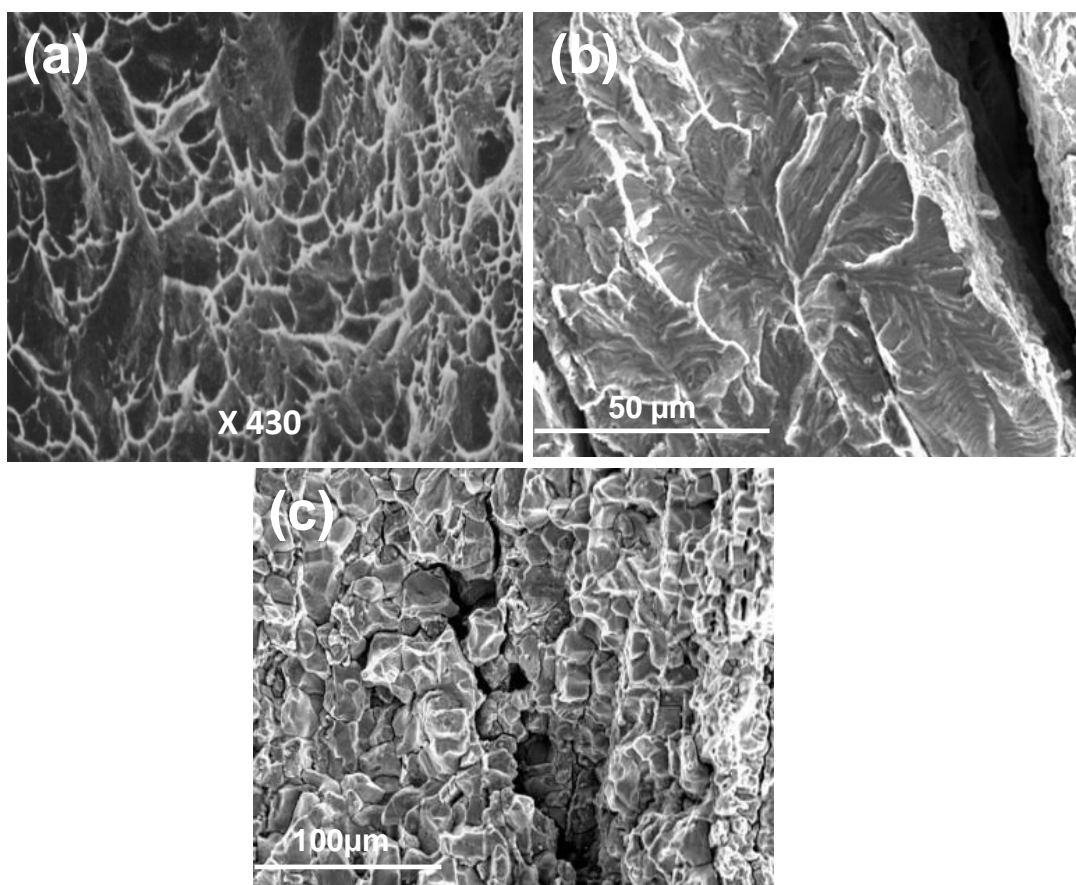


**Fig. 3.6.** Representative fractographs of (a) ductile failure due to mechanical overloading [36], (b) exclusive transgranular SCC [133], and (c) exclusive intergranular SCC [134]

### 3.3 Electrochemical characterizations

Electrochemical testing was performed for qualitative and/or quantitative investigations of the corrosion kinetics of the Mg alloy substrates as well as the coated specimens. All the electrochemical experiments were carried out in a conventional three-electrode cell that has a saturated calomel electrode (SCE) as the reference electrode and a platinum mesh as the counter electrode. A schematic of the electrochemical cell is shown in Fig. 3.7. Before electrochemical experiments were started, open circuit potential (OCP) was monitored for immersion period of 2 h, i.e. the time required for the stabilization of the electrochemical system, using a PARSTAT 2273 (Princeton Applied Research) potentiostat. A fluctuation of less than 10 mV over a period of 1000 s is generally taken to indicate stabilization.

As also described in the case of SCC testing set-up, a submersible pump was used to continuously circulate the *m*-SBF through inlet and outlet of the electrochemical cell (as shown in the experimental set-up in Fig. 3.7). The circulation of the *m*-SBF solution using a water bath and heater also maintained the body temperature of 37 °C. All the electrochemical tests were at least duplicated in order to examine the reproducibility of the results.

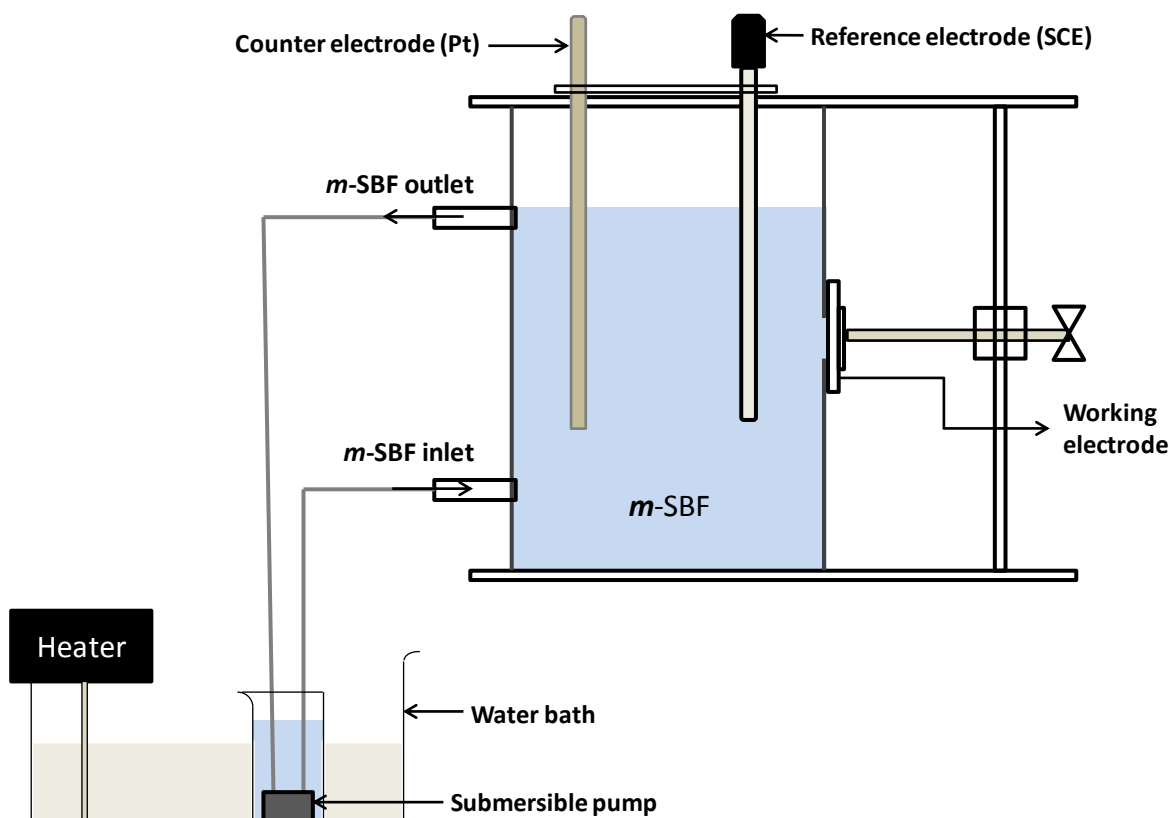


**Fig. 3.7.** Schematic diagram of the experimental set-up for electrochemical experiments

### 3.3.1 Potentiodynamic polarization

The potentiodynamic polarization scans were performed for investigating the cathodic and anodic current densities of different specimens (Mg alloy substrates, graphene-CaCO<sub>3</sub> and only-CaCO<sub>3</sub> coated Mg alloy) in *m*-SBF solution at 37 °C. The scans were carried out starting at 250 mV more negative to open circuit potential in the *m*-SBF solution at a scan rate of 0.5 mV/s.

### 3.3.2 Electrochemical impedance spectroscopy (EIS)

Electrochemical impedance spectroscopy (EIS) is used for quantitative measurement of polarization resistance of different systems such as alloys, metals, coated alloys etc. EIS has many advantages in comparison with other electrochemical techniques. Due to application of very small amplitude of AC potential signal, it is a non-destructive method for the evaluation of detailed time dependent corrosion kinetics at different interfaces, viz., metal/electrolyte, coating/electrolyte, metal/coating etc. Furthermore, the application of appropriate equivalent electrical circuit (EEC) based upon hypothetical corrosion mechanism makes possible to calculate interfacial resistances and capacitances, which can be related to the homogeneity of the corrosion films/coating and can describe corrosion mechanisms. Also, the relative magnitudes of these interfacial resistances and capacitances provide an estimation of the protection provided by a film/coating. To select the most probable equivalent circuit, three conditions should be considered and fulfilled: (i) EEC must represent the physical significance of electrochemical phenomena of the system, (ii) EEC should minimize the relative error for each frequency point for both absolute and imaginary parameters, and (iii) EEC should offer low chi-square values (typically below  $10^{-3}$ ) [188]. Once an appropriate EEC have been chosen, the experimental EIS data is simulated by chosen EEC using complex nonlinear least square fitting (CNLS) method.

In this study, EIS experiments were carried out by applying a sinusoidal potential wave at open circuit potential with amplitude of 10 mV. Impedance response was measured over frequencies between 1 MHz and 10 mHz, recording 10 points per decade of frequency, using PAR power suite electrochemistry package. Impedance analysis was carried out using PAR ZSimpWin software generally on the experimental EIS data in frequency range of 100 kHz-50 mHz.



### **3.4 Post corrosion analysis**

Corrosion morphologies of the different specimens (graphene-CaCO<sub>3</sub> and only-CaCO<sub>3</sub> coated) were examined using a JEOL 7001F SEM. The specimens were analyzed without cleaning the corrosion products (corroded specimens were just rinsed with deionised water and were subsequently dried with compressed air). Also, all the corroded specimens were gold coated prior to the SEM to avoid charging of less conducting corrosion products.

## Chapter 4

### 4. Stress corrosion cracking of AZ91D and Mg-Zn-Ca alloys under dynamic and static loadings in the physiological environment\*

#### 4.1 Introduction

As described in Chapter 2 (Section 2.6), it is essential that metallic implant materials possess adequate resistance to cracking/fracture under synergistic action of the corrosive physiological environment and mechanical loading (i.e. stress corrosion cracking (SCC)), before the implant can be put to actual use. In general, aluminium (Al)-containing magnesium alloys (such as AZ series) have been reported to be highly susceptible to SCC and the susceptibility generally increases with Al content, as shown in Fig. 2.9. In such alloys, SCC-induced fractures may occur at stresses as low as 50 % of the yield strength. It is also noted that the most SCC studies have been conducted on Al-containing magnesium alloys in aqueous environments. However, the Al-containing Mg alloys may not find actual use as human implants because Al is reported to be toxic to human health (as Al can cause neurological disorders such as dementia and Alzheimer's disease) [28, 180]. Nevertheless, this chapter first investigates the mechanistic understanding of SCC of Mg alloys in the physiological environment. For this purpose, one of the most common magnesium alloys, AZ91D, was investigated under dynamic and

\*Results of this chapter have been published in the following papers:

- (1) Lokesh Choudhary, R.K. Singh Raman, "Magnesium alloys as body implants: Fracture mechanism under dynamic and static loadings in a physiological environment", **Acta Biomaterialia**, 8 (2012) 916-923
- (2) Lokesh Choudhary, R.K. Singh Raman, "Mechanical integrity of magnesium alloys in a physiological environment: Slow strain rate testing based study", Accepted for publication in **Engineering Fracture Mechanics** (DOI: 10.1016/j.engfracmech.2012.09.016)

static loading in *m*-SBF. This exercise also provided the baseline data for other magnesium alloys that can be actually used as biodegradable implants (such as Mg-Zn-Ca alloy developed in this study with Zn and Ca as main alloying element to avoid toxicity issues).

In summary, this chapter presents the assessment of SCC of a rapidly corroding Mg alloys, and investigates the SCC mechanism in *m*-SBF. The SCC susceptibility of the alloy in *m*-SBF was established by slow strain rate tensile (SSRT) testing using smooth specimens under different electrochemical conditions for identifying the SCC mechanism. However, to assess the life of the common implant devices (such as screws, pins, rods, wires and stents) that often possess sharp contours, protrusions, fine micro-cracks, SCC susceptibility of notched specimens of AZ91D was also investigated by a fracture mechanics based technique, circumferential notch tensile (CNT) testing. CNT tests also produced important design data, i.e. threshold stress intensity for SCC ( $K_{ISCC}$ ) and SCC crack growth rate, in *m*-SBF environment. Fractographic features of SCC were examined using scanning electron microscopy. This chapter also compares the SCC behaviour of AZ91D and Mg-Zn-Ca alloys in the physiological environment, based on their electrochemical characteristics.

## 4.2 Experimental

The details of the chemical composition of AZ91D and Mg<sub>3</sub>Zn<sub>1</sub>Ca alloys have been provided in Table 3.1 and 3.2, respectively. The physiological environment of modified simulated body fluid (*m*-SBF) was chosen as described in Chapter 3, Section 3.1.

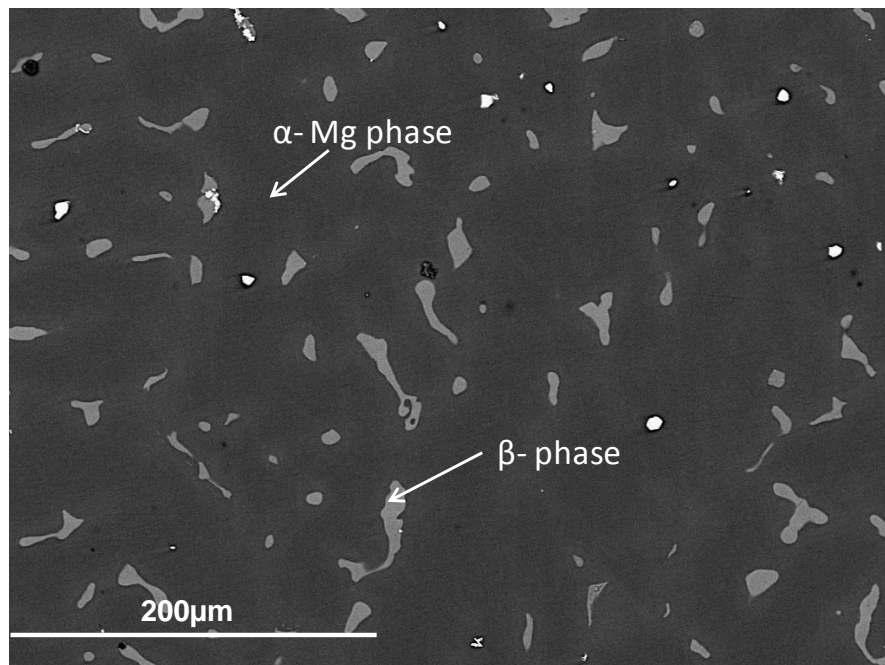
Experimental details about the specimen dimensions and geometries, slow strain rate tensile (SSRT) testing, circumferential notch tensile (CNT) testing, fractography and potentiodynamic polarization have also been provided in Chapter 3.

## 4.3 Results and discussion

### 4.3.1 SCC of AZ91D under dynamic and static loadings

#### 4.3.1.1 Microstructure of AZ91D alloy

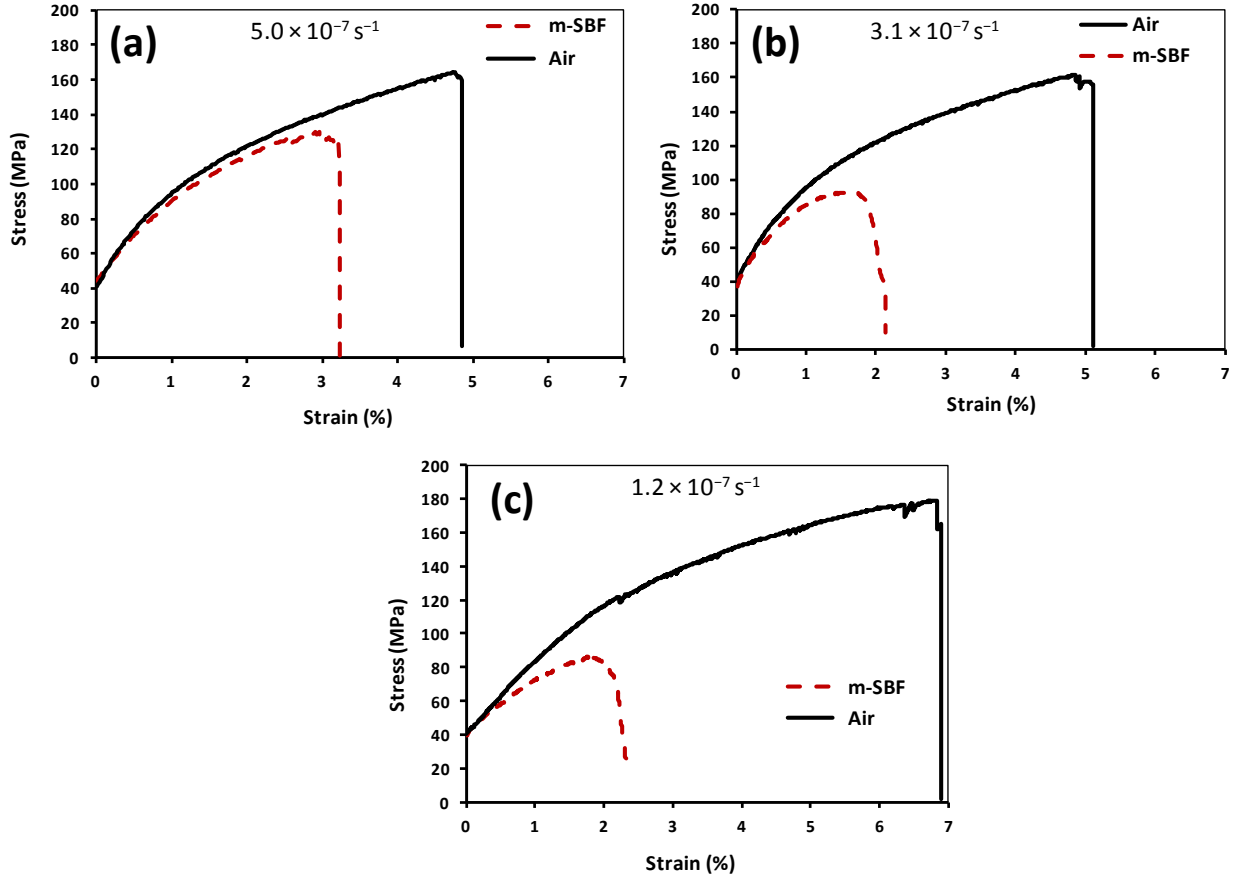
The microstructure of as-cast AZ91D magnesium alloy is shown in Fig. 4.1. It is mainly composed of primary  $\alpha$ -Mg phase and secondary  $\beta$ -phase (the latter is primarily present along the grain boundaries). The discontinuous  $\beta$  precipitate is well established to be the intermetallic compound,  $\text{Mg}_{17}\text{Al}_{12}$  [72, 97].



**Fig. 4.1.** Microstructure (SEM back-scattered electron image) of AZ91D alloy

#### 4.3.1.2 Slow strain rate tensile (SSRT) testing of AZ91D

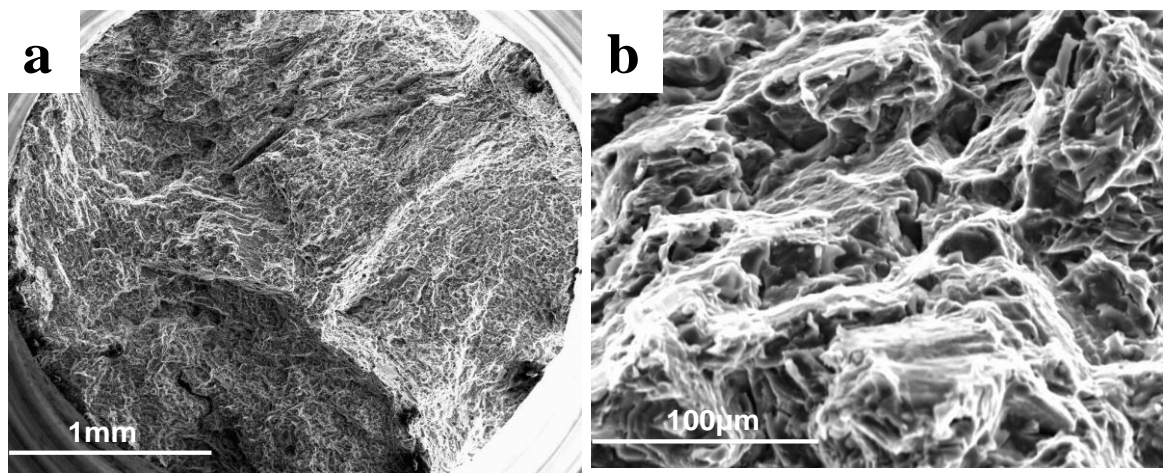
The stress vs. strain curves for the AZ91D alloy (in *m*-SBF solution at 37 °C and laboratory air) at the strain rates of  $5.0 \times 10^{-7} \text{ s}^{-1}$ ,  $3.1 \times 10^{-7} \text{ s}^{-1}$  and  $1.2 \times 10^{-7} \text{ s}^{-1}$  are shown in Fig. 4.2a, 4.2b and 4.2c, respectively.



**Fig. 4.2.** Stress vs. strain curves for AZ91D in *m*-SBF solution and air at the strain rates: (a)  $5.0 \times 10^{-7} \text{ s}^{-1}$ , (b)  $3.1 \times 10^{-7} \text{ s}^{-1}$  and (c)  $1.2 \times 10^{-7} \text{ s}^{-1}$

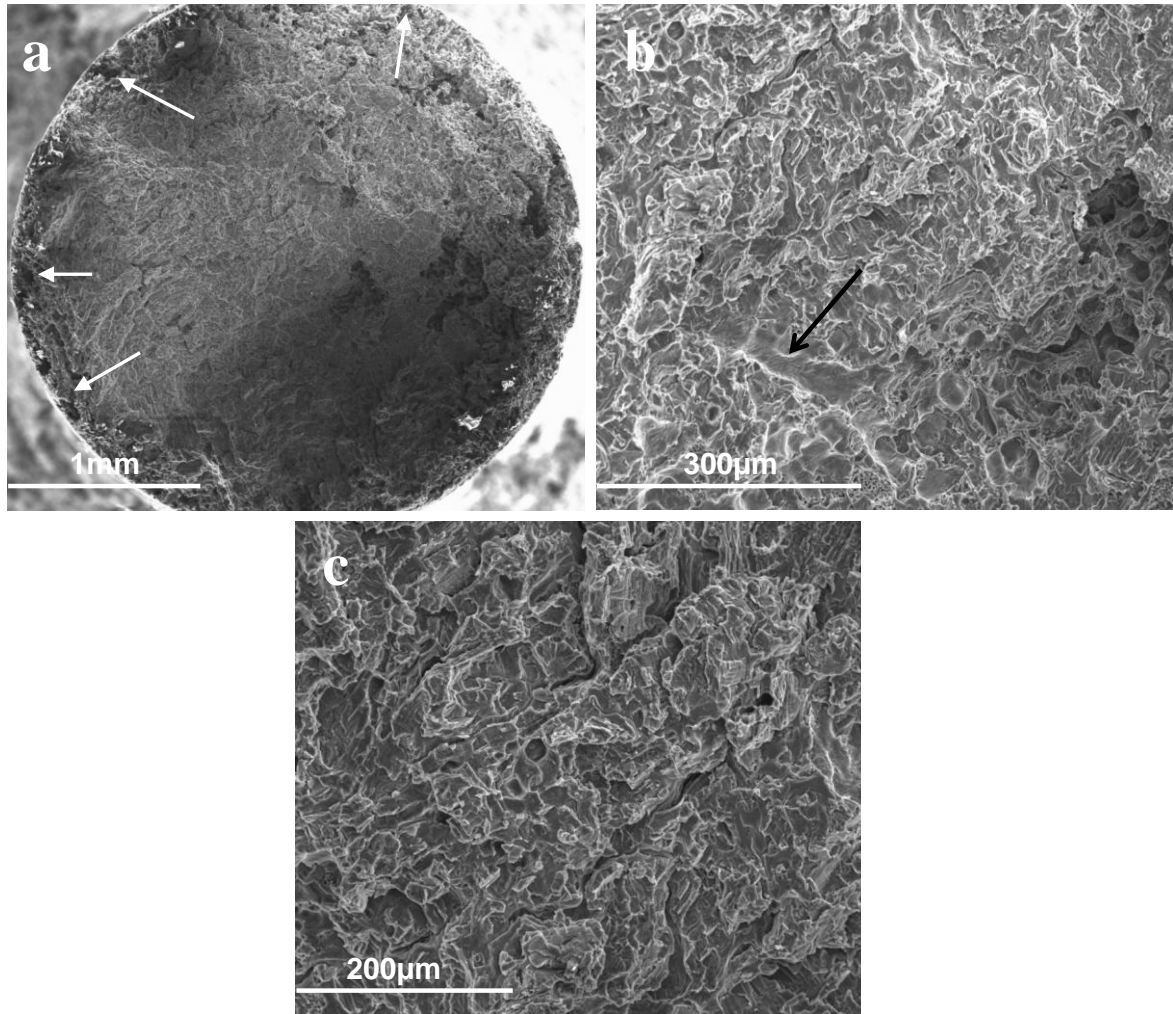
AZ91D tested at the strain rate of  $5.0 \times 10^{-7} \text{ s}^{-1}$  in air (Fig. 4.2a) exhibited an elongation-to-failure ( $\epsilon_f$ ) of  $(5.1 \pm 0.3) \%$  and UTS of  $(170 \pm 7.1) \text{ MPa}$ . At the same strain rate when tested in *m*-SBF solution, AZ91D suffered a significant loss in the mechanical properties ( $\epsilon_f = (3.2 \pm 0.1) \%$  and UTS =  $(128 \pm 3) \text{ MPa}$ ). Similarly, as shown in Fig. 4.2b and c, AZ91D tested at the lower strain rates of  $3.1 \times 10^{-7}$  and  $1.2 \times 10^{-7} \text{ s}^{-1}$  in air exhibited superior mechanical properties ( $\epsilon_f$  and UTS) as compared to the specimens tested in *m*-SBF at these strain rates. These deteriorations in the  $\epsilon_f$  and UTS could be the result of susceptibility of the AZ91D alloy to the SCC in *m*-SBF solution. For confirmation, fractography was performed on the failed specimens of AZ91D.

The overall fracture surface of specimen tested in air is shown in Fig. 4.3a. The fracture surface of the specimen tested in air primarily revealed dimples at higher magnification (Fig. 4.3b), confirming the mechanical overload failure. There were also occasional features of brittle fracture, which may be associated with secondary phase particles of the alloy (predominantly,  $\beta$ -phase). Mix-mode fracture observed in air is consistent with the fractographic features for the magnesium alloy tested in air and reported in the literature [18, 19].



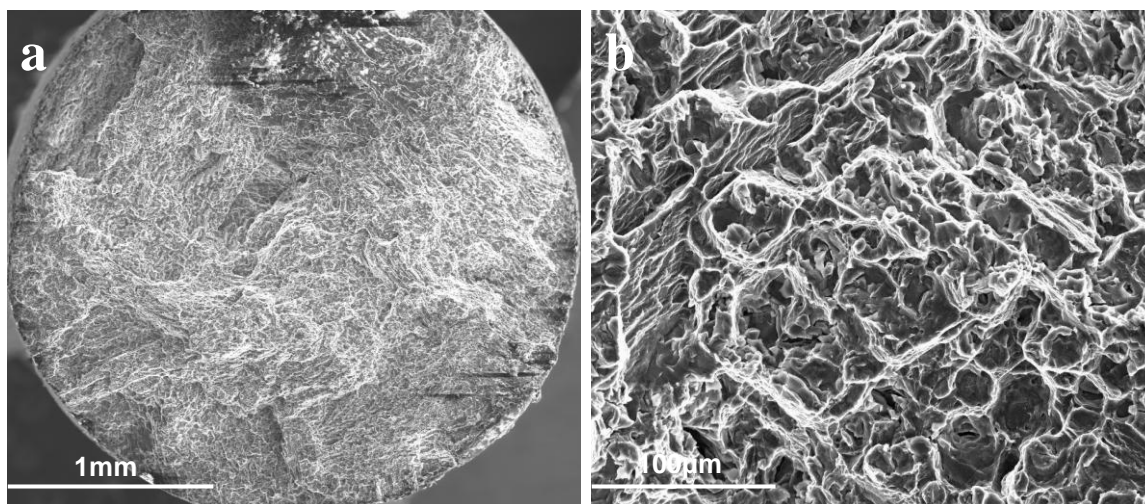
**Fig. 4.3.** Representative fractographs of the AZ91D tested in air: (a) overall fracture surface, (b) the fracture surface showing dimples and occasional instances of brittle fracture

Fig. 4.4 represents the fractographs of the AZ91D specimen tested in *m*-SBF solution at the strain rate of  $1.2 \times 10^{-7} \text{ s}^{-1}$ . The overall fracture surface (Fig. 4.4a) suggests that the specimen has undergone pitting and localized corrosion along the circumference. The SCC was manifested by the presence of transgranular cracking (Fig. 4.4b, arrow) and crack branching (Fig. 4.4c) on the fracture surface. The fractograph of the specimen tested in *m*-SBF at the strain rate of  $3.1 \times 10^{-7} \text{ s}^{-1}$  showed similar SCC features to the specimen tested in *m*-SBF at the strain rate of  $1.2 \times 10^{-7} \text{ s}^{-1}$ .



**Fig. 4.4.** Fractograph of the AZ91D specimen tested in *m*-SBF solution at 37 °C at the strain rate,  $1.2 \times 10^{-7} \text{ s}^{-1}$ : (a) overall fracture surface (arrows indicate pitting at the circumference), (b) evidence of transgranular cracking (indicated by arrow) and (c) fractograph showing crack branching

Fig. 4.5a represents the overall fracture surface of AZ91D alloy tested in *m*-SBF solution at  $5.0 \times 10^{-7} \text{ s}^{-1}$ . At a higher magnification, the fracture surface reveals transgranular cracking (Fig. 4.5b).



**Fig. 4.5.** Fractograph of the AZ91D specimen tested in *m*-SBF solution at 37 °C at the strain rate,  $5.0 \times 10^{-7} \text{ s}^{-1}$ : (a) overall fracture surface, (b) evidence of transgranular cracking

In another set of experiment, SSRT tests on AZ91D alloy in *m*-SBF were conducted at a strain rate of  $2.2 \times 10^{-7} \text{ s}^{-1}$  under different conditions: (a) strained in air, (b) strained in *m*-SBF solution, (c) immediately strained in air after pre-immersion in *m*-SBF solution for 28 h, and (d) continuously cathodically charged and simultaneously pulled in *m*-SBF. The purpose of these tests were to investigate: (1) the occurrence of SCC and its mechanism, and (2) whether the loss of the mechanical property is indeed a result of the synergistic effect of stress and corrosive environment (i.e. SCC), or whether it can simply be attributed to the continuously reducing cross-sectional area of the specimen due to high corrosion rate of magnesium alloys. The stress vs. time curves for AZ91D alloy under these conditions are presented in Fig. 4.6. AZ91D tensile specimen, which was strained continuously in *m*-SBF at a strain rate of  $2.2 \times 10^{-7} \text{ s}^{-1}$  (Fig. 4.6b), failed in 28 h. Accordingly, a pre-immersion time of 28 h was selected for straining the pre-immersed AZ91D tensile specimen in air, assuming the stress-independent corrosion damage to be similar to that of specimen strained in *m*-SBF solution. The specimen pulled in *m*-SBF solution (Fig. 4.6b) shows a considerable reduction in mechanical properties as compared to the specimen pulled in air (Fig. 4.6a). The stress-time curve for the specimen pre-immersed in *m*-SBF for 28 h and then strained in air (Fig. 4.6c) is very similar to the



specimen pulled in air (Fig. 4.6a). Therefore, it is fair to infer that the simultaneous effect of stress and corrosive environment (i.e. SCC) was the primary cause of the loss of mechanical property in the case of specimen pulled in *m*-SBF (Fig.4.6b) and the stress-independent corrosion contributed only marginally. Also, a considerable loss of the mechanical strength and a decrease in the time-to-failure were observed in continuous cathodic charging conditions (i.e., when anodic dissolution is minimal, Fig. 4.6d). Thus the cathodic charging experiment infers hydrogen-induced cracking as the SCC mechanism. However, the maximum loss in strain (elongation-to-failure) was observed in the case of the specimen strained in *m*-SBF solution at open circuit conditions (Fig. 4.6b), which indicated the possibility of a combined effect of hydrogen-induced cracking and anodic dissolution. This combined mechanism may be plausible for magnesium and its alloys, which are known to invariably produce considerable amounts of hydrogen during anodic dissolution.

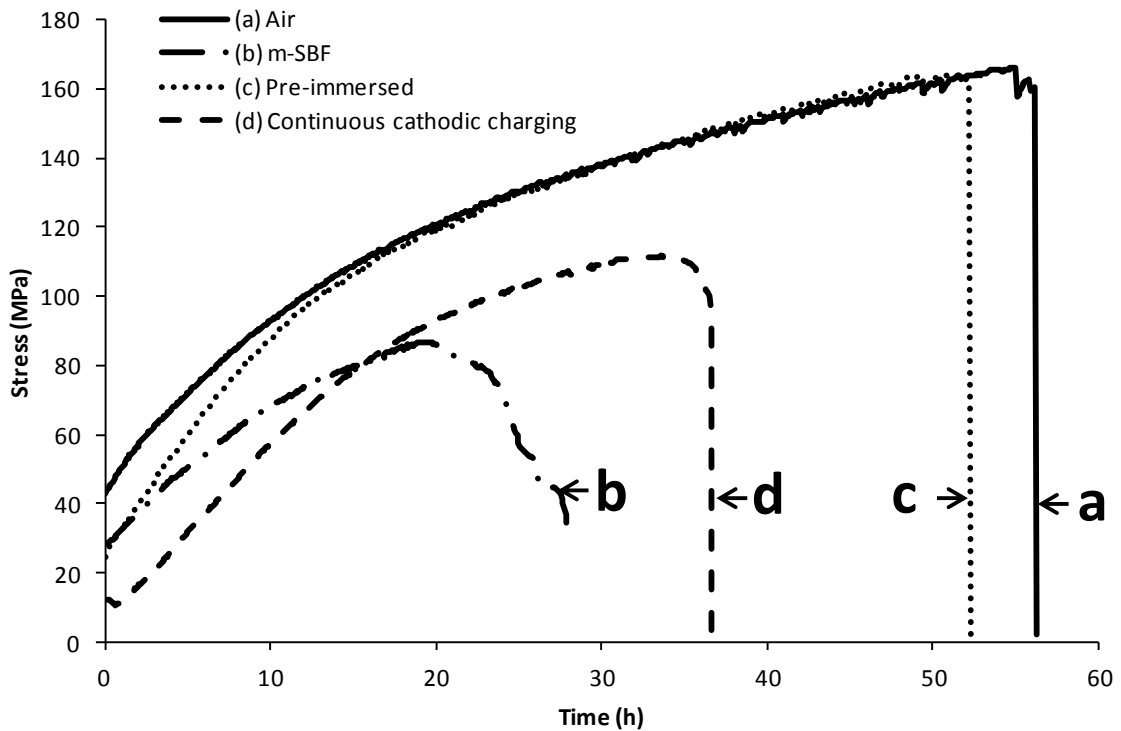


**Fig. 4.6.** Stress vs. time plots of AZ91D alloy tested at a strain rate of  $2.2 \times 10^{-7} \text{ s}^{-1}$ : (a) in air, (b) in *m*-SBF solution, (c) pre-immersed in *m*-SBF for 28h and then immediately strained in air, and (d) continuously charged at 200 mV cathodic to open circuit potential in *m*-SBF during the test

The fractographs for the specimen tested in air at  $2.2 \times 10^{-7} \text{ s}^{-1}$  were similar to the fractographs of the specimen tested at  $1.2 \times 10^{-7} \text{ s}^{-1}$  and  $5 \times 10^{-7} \text{ s}^{-1}$  (Fig. 4.3), and showed dimples over the fracture surface. The fractograph for the specimen pulled in *m*-SBF solution at 37 °C is shown in Fig. 4.7. Overall fracture surface of the specimen tested in *m*-SBF shows the localized attack at the specimen circumference (Fig. 4.7a). At higher magnification, the fractography of this specimen revealed distinctive features of SCC such as transgranular cracking and localized cracks (Fig. 4.7b).

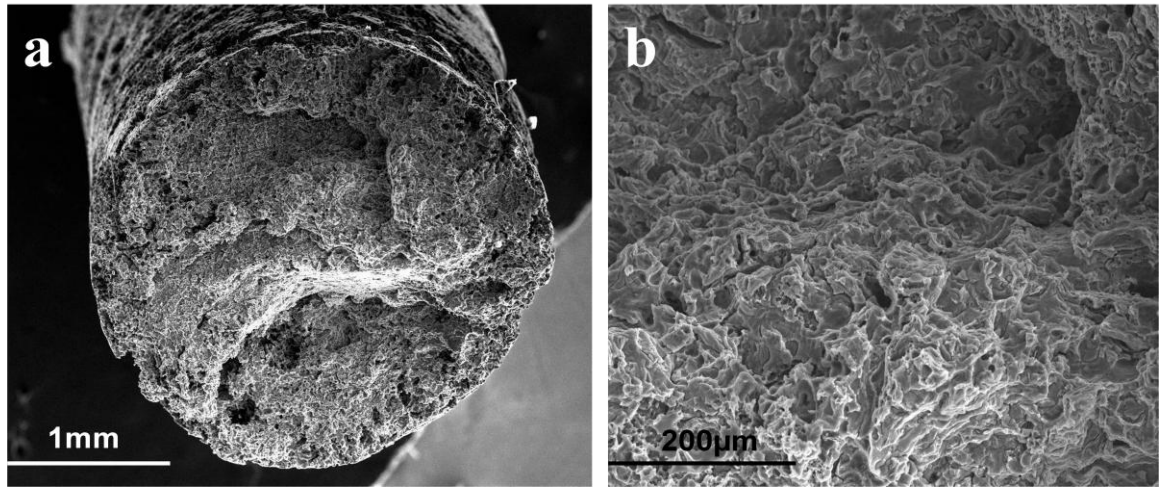


**Fig. 4.7.** Fractograph of the specimen failed in *m*-SBF at a strain rate of  $2.2 \times 10^{-7} \text{ s}^{-1}$ : (a) overall fracture surface, and (b) evidence of transgranular cracking

The fractograph for the specimen immersed in *m*-SBF for 28 h followed by straining in air showed dimples (Fig. 4.8a) similar to that observed for the specimen tested in air, suggesting the ductile failure. The specimen that was cathodically charged and simultaneously pulled in *m*-SBF solution exclusively showed evidences of the transgranular cracking (arrows, Fig. 4.8b). The transgranular cracking observed in the case of cathodically charged conditions is attributed to mechanism involving hydrogen. In this mechanism, the hydrogen generated during the cathodic charging diffuses ahead of crack tip and embrittles the matrix [35].

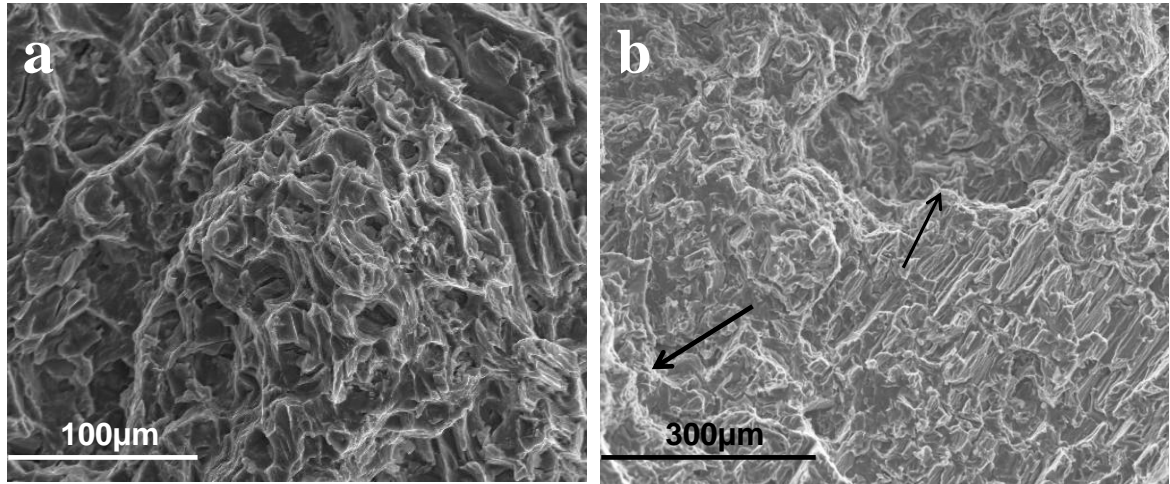


**Fig. 4.8.** SEM fractographs for the specimens: (a) immersed in *m*-SBF solution for 28 h and then strained in air, and (b) continuously cathodically charged and simultaneously pulled in *m*-SBF

Although SSRT testing in different environmental conditions could mechanistically establish the SCC susceptibility of AZ91D in the physiological environment, it is also equally important to determine the SCC design parameters (i.e. threshold stress intensity for SCC ( $K_{ISCC}$ ) and crack growth rates) using a fracture mechanic-based study in order to estimate the life time of temporary implant devices.

#### 4.3.1.3 Circumferential notch tensile (CNT) testing for $K_{ISCC}$ data

Before CNT testing, a sharp fatigue pre-crack was produced ahead of the machined notch using a cantilever-beam rotating-bending fatigue machine. The fatigue pre-cracked CNT specimens of AZ91D alloy were loaded at different stress intensities in *m*-SBF at 37 °C. Specimens failed after different time durations depending on the applied stress intensities. The  $K_I$  at each applied load was calculated (following the procedure described in Section 3.2.2.3) and plotted against the time-to-failure (Fig. 4.9). As evident from Fig. 4.9, the time-to-failure increased exponentially with decreasing stress intensity. For example, a CNT specimen loaded at a stress intensity of  $11.7 \text{ MPa m}^{1/2}$  failed in only 16 h, whereas it took 119 h for a specimen

loaded at a stress intensity of  $6.8 \text{ MPa m}^{1/2}$  to fail. The threshold stress intensity was determined by drawing an asymptote to time-to-failure axis in the plot of stress intensity vs. time-to-failure (Fig. 4.9). This is consistent with the common practice [132]

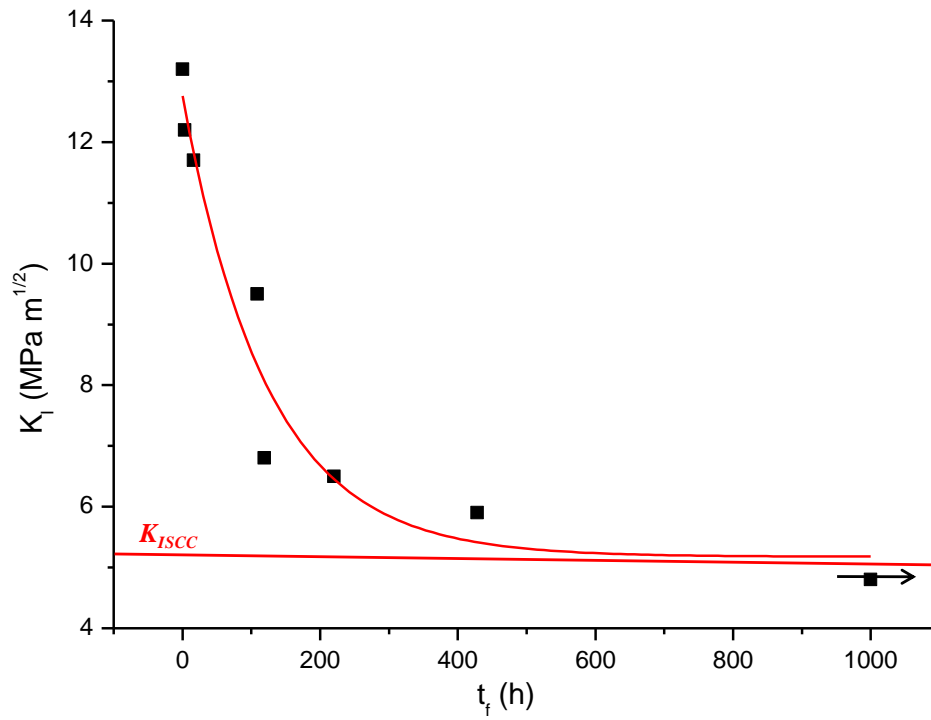


**Fig. 4.9.**  $K_I$  vs.  $t_f$  plot of AZ91D alloy tested in *m*-SBF at 37 °C

As described in Section 3.2.2.4 in Chapter 3,  $K_I$  data generated from each test had to be subjected to the rigorous validity tests. Table 4.1 would suggest that the  $K_I$  data used for the plot in Fig. 4.9 passed the validity requirements.

Table 4.1: Experimentally determined  $K_I$  data satisfying the validity requirement

$K_I$ (MPa m <sup>1/2</sup> )	$t_f$ (h)	$a_f$ (mm)*	$2r_y$ (mm)*	$\sigma_N/\sigma_y$ *	Deviation
13.2	0	1.4	1	2.43	$\pm 0.44$
12.2	3.4	1.32	0.92	2.33	$\pm 0.35$
11.7	16	1.44	0.87	2.28	$\pm 0.14$
9.5	108.5	1.32	0.67	2	$\pm 1.17$
6.8	119	1.25	0.42	1.39	$\pm 1.27$
5.9	428	1.25	0.34	1.25	$\pm 0.48$
6.5	214	1.21	0.37	1.31	$\pm 0.044$
4.8	Did not fail	1.45	0.24	1.19	$\pm 0.37$

\*  $a_f$  is fatigue crack depth (m),  $r_y$  is Irwin correction factor (m),  $\sigma_N$  is nominal applied stress (Pa) and  $\sigma_y$  is 0.2 % offset tensile yield stress (Pa).

The equation of the curve which best fits the experimental results (Fig. 4.9) can be given by Equation 4.1:

$$K_I = 7.58 \exp\left(-\frac{t_f}{123.58}\right) + 5.18 \quad (4.1)$$

According to Equation 4.1, the value of  $K_I$  when producing a horizontal asymptote to time-to-failure axis in Fig. 4.9 (i.e.,  $K_{ISCC}$ ) is 5.18 MPa m<sup>1/2</sup> for AZ91D alloy in *m*-SBF. Table 4.1 also shows that a specimen tested at  $K_I$  below 5.18 MPa m<sup>1/2</sup> did not fail within 1000 h.

Fracture surfaces of CNT specimens were observed under the scanning electron microscope (SEM) after cleaning of corrosion products. Fig. 4.10a shows the overall fractograph of a specimen that failed at a stress intensity of 6.8 MPa m<sup>1/2</sup>. The fracture surface consisted of four regions: machined notch, fatigue pre-cracked region, SCC zone and mechanical overload failure zone. At higher magnifications, distinctive features of each of these regions become clearer. Fig. 4.10b shows the transition from fatigue pre-cracked region to SCC zone. The fatigue pre-cracked region is characterized by beach marks running from the circumference.

The SCC region mainly consisted of transgranular cracking and a few cleavage marks, which may be an indicative of hydrogen-assisted cracking. Apart from transgranular cracking, a few localized pits were also visible. The stress corrosion crack propagated transgranularly until the critical stress intensity (i.e fracture toughness) was attained. At this stage, the mechanical overloading occurred. Accordingly, the central part of the fracture surface revealed ductile failure characterized by dimple formation (Fig. 4.10c), which confirmed that the final failure indeed occurred by mechanical overloading.

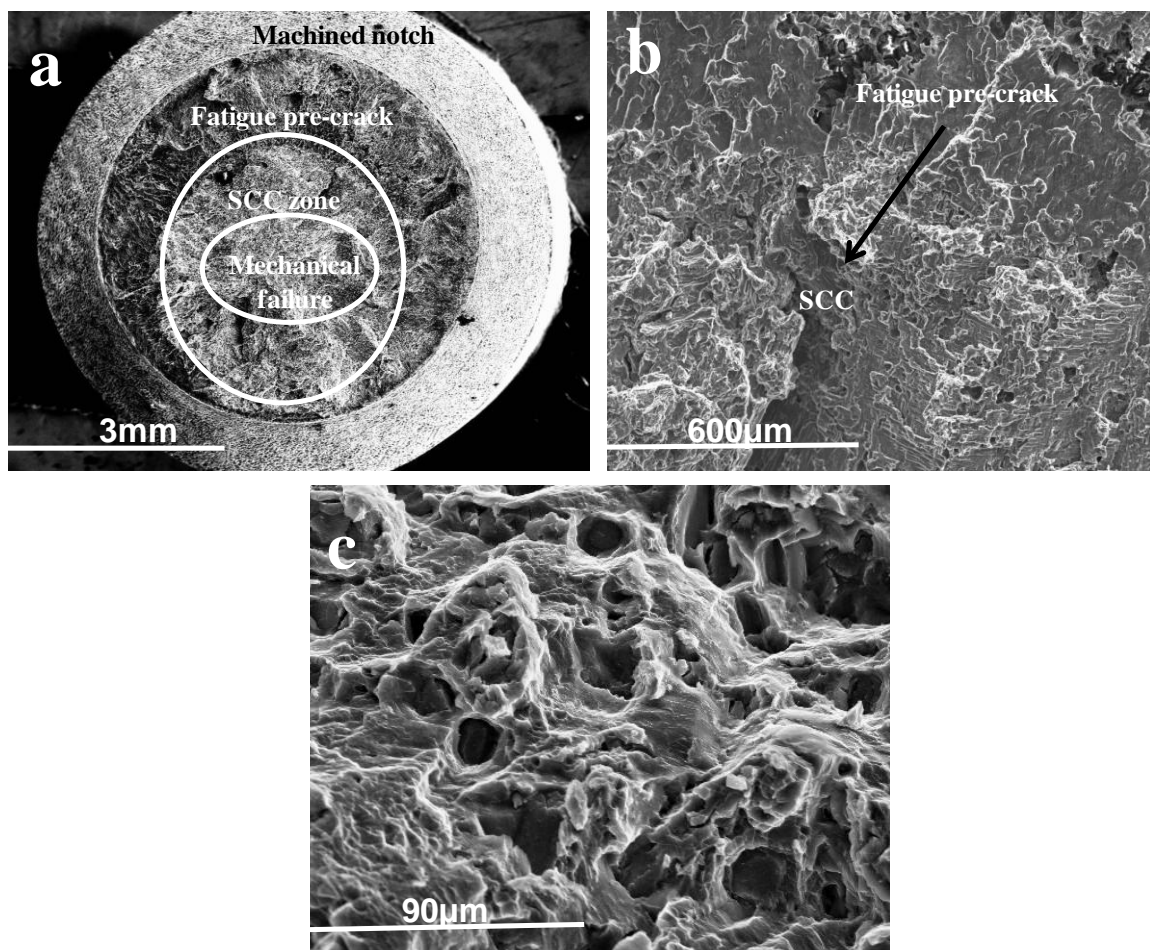


**Fig. 4.10.** SEM fractographs of the specimen tested at  $K_I = 6.8 \text{ MPa m}^{1/2}$ : (a) the overall fracture surface showing machined notch, fatigue pre-crack, SCC and mechanical failure zones, (b) fractograph showing fatigue pre-cracked and SCC zones (arrow indicating the crack propagation direction), and (c) mechanical failure zone showing the dimples

Fractographs in Fig. 4.11 suggest the fracture features of the specimen tested at another stress intensity ( $11.7 \text{ MPa m}^{1/2}$ ) to be similar to those in Fig. 4.10. It has been reported [114] that SCC of Mg-Al alloys is usually transgranular, but instances of intergranular cracking or a mix of both are also reported. Stameppla et al. [36] reported the transgranular SCC of magnesium alloys to be associated with conditions causing electrochemical breakdown or mechanical rupture of protective films at the crack tip, which allows the hydrogen entry.

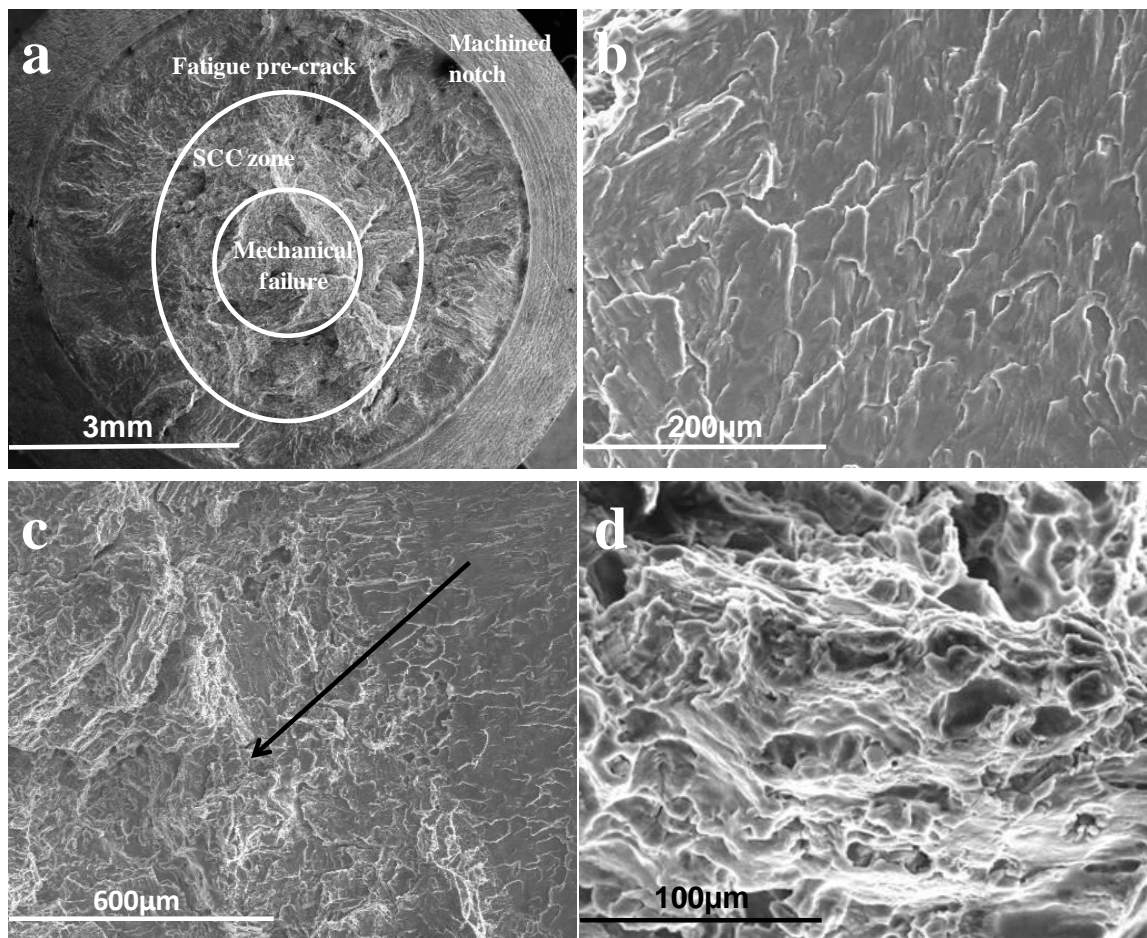


**Fig. 4.11.** SEM fractographs of the specimen tested at  $K_I = 11.7 \text{ MPa m}^{1/2}$ : (a) the overall fracture surface showing machined notch, fatigue pre-crack, SCC and mechanical failure zones, (b) fatigue pre-cracked area, (c) fractograph showing transition from fatigue pre-cracked area to SCC zone (arrow indicating the crack propagation direction), and (d) mechanical failure zone showing the dimple formation

Temporary biodegradable implants are required to serve at least for a definite time period depending on their applications such as the age of a patient. For the implant devices with sharp

corners and protrusions, it is essential to determine the stress corrosion crack growth rate for predicting the service life of the component in the physiological environment. When the growing crack reaches the critical size, the mechanical overloading takes over before the fracture. The crack growth rate for AZ91D alloy in *m*-SBF is calculated (as discussed in Section 3.2.2.6) from Equation 3.25 for each value of  $K_I$ . The Fig. 4.12 represents the crack growth rate vs.  $K_I$  for AZ91D alloy in *m*-SBF. The equation of the line in Fig. 4.12, which best fits the results of  $da/dt$  vs.  $K_I$  for the AZ91D magnesium alloy in *m*-SBF at 37 °C, is as follows:

$$\frac{da}{dt} = (2.31 \times 10^{-10}) K_I - 1.27 \times 10^{-9} \quad (4.2)$$

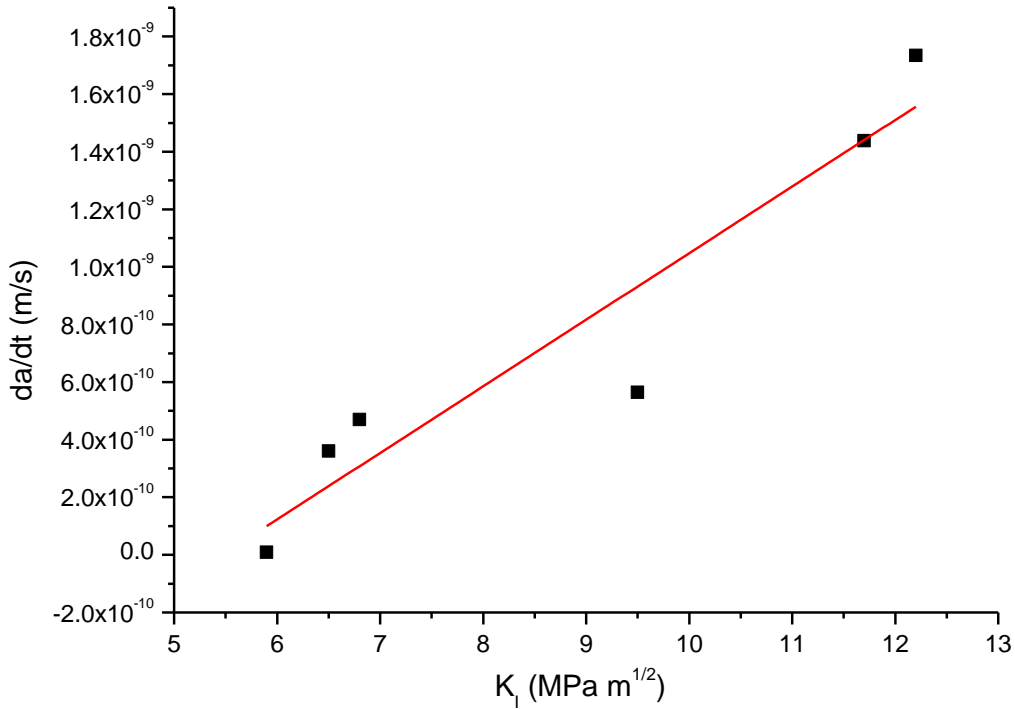


**Fig. 4.12.** Crack growth rate ( $da/dt$ ) vs.  $K_I$  plot for AZ91D alloy in *m*-SBF at 37 °C

In term of crack growth rate,  $K_{ISCC}$  is defined as the point where crack growth becomes zero or insignificantly slow, such as  $10^{-14}$  m/s [189]. Accordingly, in this study, a crack growth rate



less than  $1 \times 10^{-14}$  m/s was considered as a zero crack growth rate. On this basis, the  $K_{ISCC}$  was determined (using Equation 4.2) to be  $5.5 \text{ MPa m}^{1/2}$  for AZ91D alloy in *m*-SBF at 37 °C. This is similar to the experimentally determined  $K_{ISCC}$  value ( $5.18 \text{ MPa m}^{1/2}$ ).

The crack growth rate increases monotonically with increasing  $K_I$ , as suggested by Equation 4.2. The crack growth rate was in the range of  $10^{-9}$  m/s for AZ91D alloy in *m*-SBF at stress intensities  $> 10 \text{ MPa m}^{1/2}$ , while it was in the range of  $10^{-10}$  m/s for stress intensities in the range of  $6.5 - 10 \text{ MPa m}^{1/2}$ . Similar crack growth rates ( $1.2 \times 10^{-9} - 6.7 \times 10^{-9}$  m/s) were reported in the literature for AZ91D alloy in distilled water under constant extension rate test conditions [105].

Some of the implant devices (e.g. stents and screws) generally have the locations of stress concentrations, such as sharp contours, that can often show crack-like behaviour. Following the procedure demonstrated in this study, it should be possible to calculate the mechanical integrity and life of such implants of magnesium alloys using the stress intensity-crack growth relation. Of course, the in-service inspection of the crack growth of such implants will be a non-trivial task. However, the flaw-tolerant design assessment of the implant devices (that may have a pre-existing fine crack), by the CNT testing as demonstrated in this study, will provide a crucial information on whether the existing crack will be tolerable for the given service time of the device [190]. It is also noted that CNT testing is one of the least expensive techniques for generating  $K_{ISCC}$  and crack growth data [191].

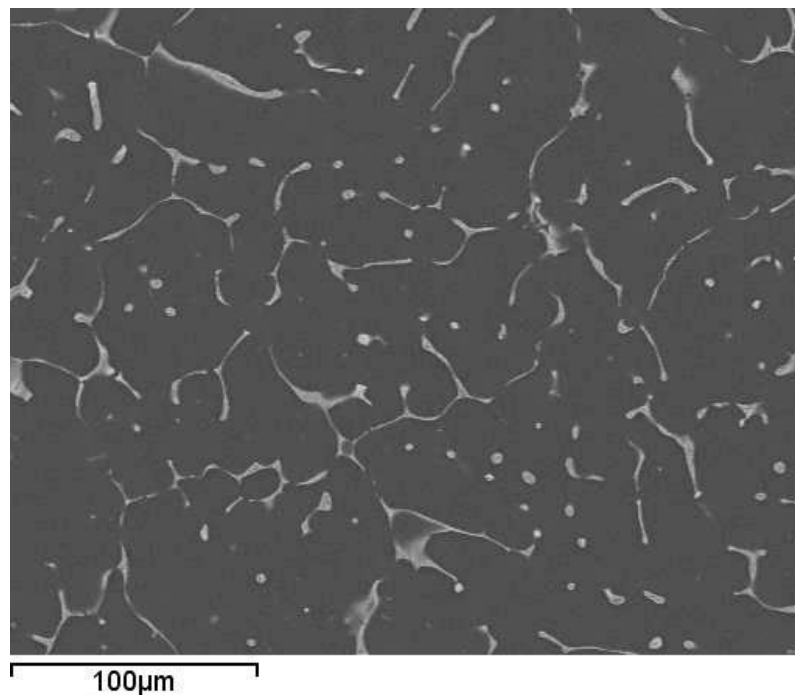
As discussed earlier, the Al-containing Mg alloys are unlikely to be used as implant materials. Nevertheless, this study provides an improved mechanistic insight into SCC fracture characteristics for magnesium alloys in physiological environment, in general, which will be a useful guideline for the potential magnesium alloys that can actually be employed. However, in the present study, an Al-free magnesium alloy (Mg-Zn-Ca alloy) was also included. While Ca and Zn are both non-toxic to the human body [29], Zn addition also improves strength of

magnesium alloys through the solid solution hardening [15, 67]. Addition of Ca is reported to refine the microstructure and improve strength as well as the corrosion resistance of magnesium alloys [16, 192]. The present study also investigates the stress corrosion cracking behavior of Mg- 3 wt. % Zn-1 wt. % Ca (Mg3Zn1Ca) magnesium alloy in the physiological environment using slow strain rate tensile (SSRT) testing.

#### **4.3.2 SCC of Mg - 3 wt. % Zn - 1 wt. % Ca (Mg3Zn1Ca) alloy**

##### **4.3.2.1 Microstructure of Mg3Zn1Ca alloy**

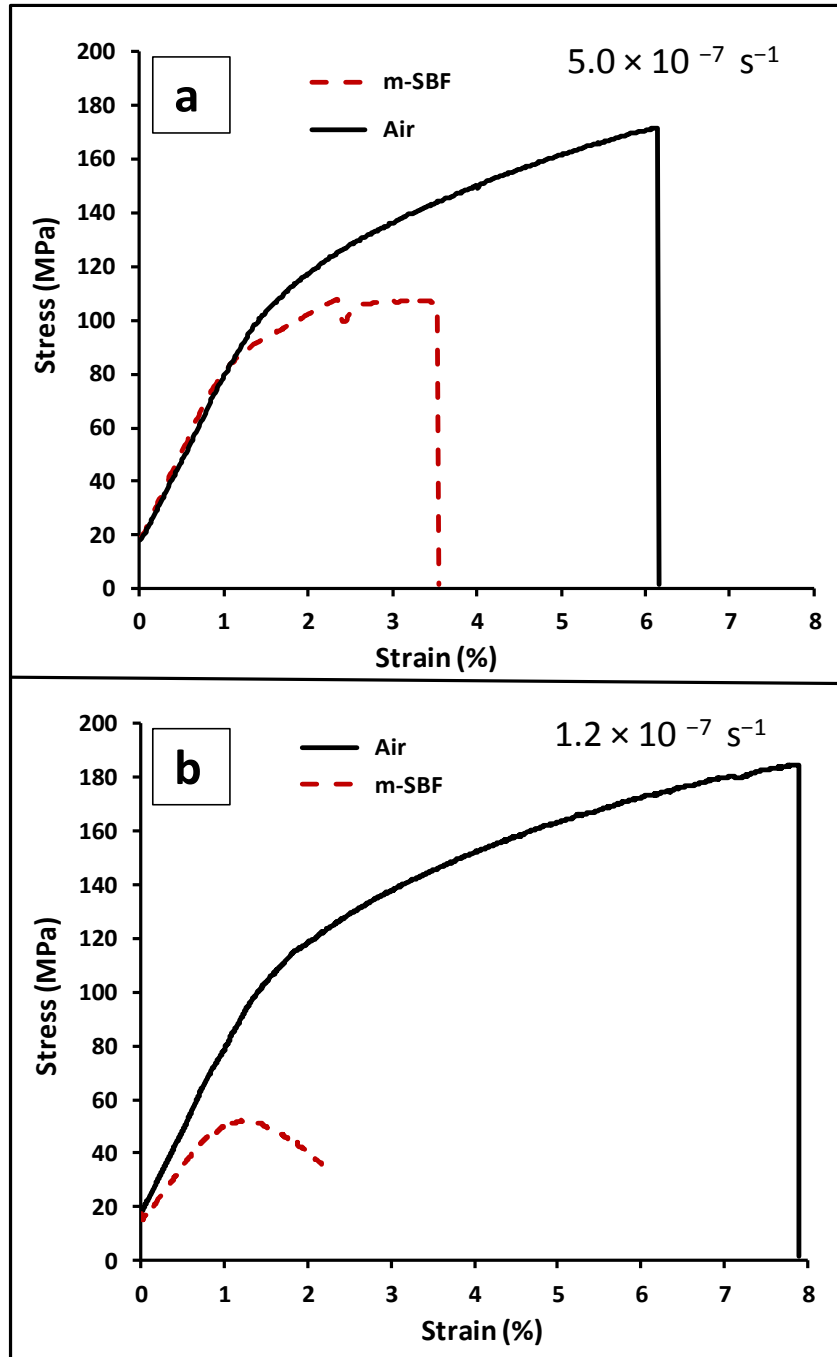
Back scattered scanning electron microscopy image of Mg3Zn1Ca alloy is shown in Fig. 4.13. It consisted of the  $\alpha$ -Mg matrix and secondary phases (which are reported to be  $\text{Ca}_2\text{Mg}_6\text{Zn}_3$  and  $\text{Mg}_2\text{Ca}$  [99, 193, 194]) mostly along the grain boundaries. The grain size was in the range of 60-80  $\mu\text{m}$ .



**Fig. 4.13.** Back scattered SEM microstructure of as-cast Mg3Zn1Ca alloy

#### 4.3.2.2 Slow strain rate tensile (SSRT) testing of Mg3Zn1Ca alloy

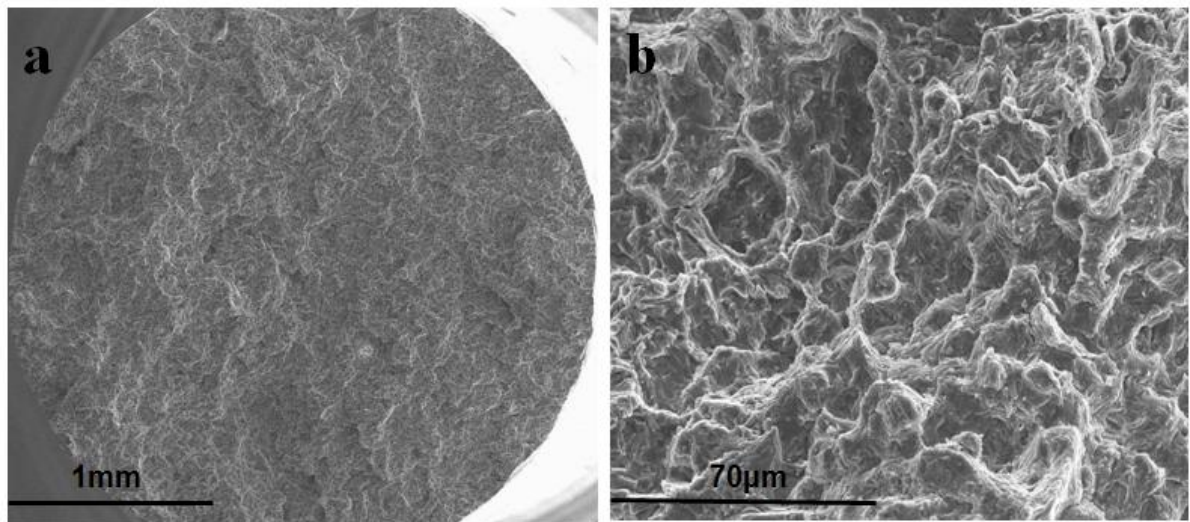
The stress vs. strain curves for the Mg3Zn1Ca alloy (in *m*-SBF and air) at the strain rates of  $5.0 \times 10^{-7} \text{ s}^{-1}$  and  $1.2 \times 10^{-7} \text{ s}^{-1}$  are shown in Fig. 4.14a and 4.14b, respectively.



**Fig. 4.14.** Stress vs. strain curves for the Mg3Zn1Ca alloy at the strain rate of: (a)  $5.0 \times 10^{-7} \text{ s}^{-1}$  and (b)  $1.2 \times 10^{-7} \text{ s}^{-1}$

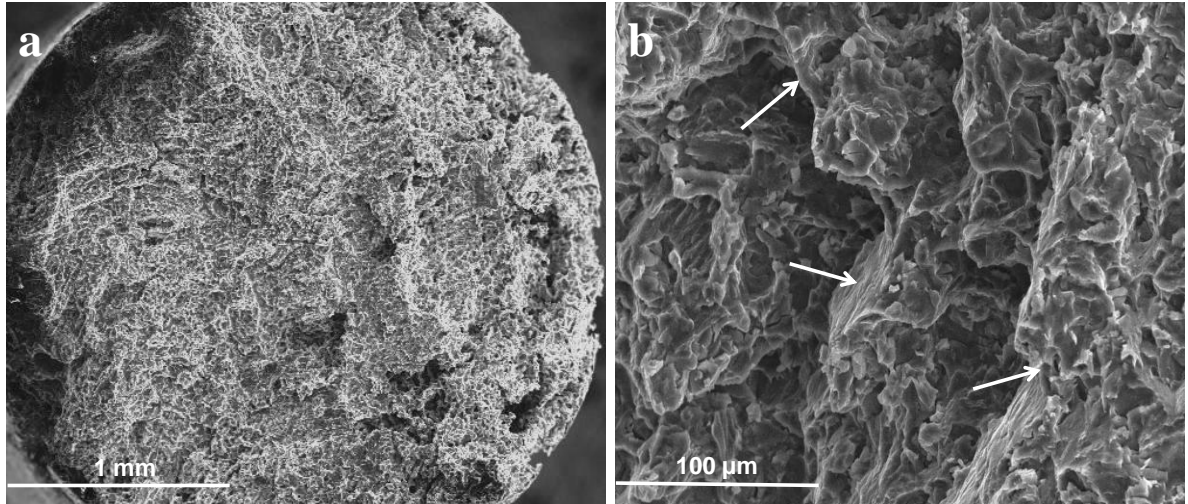
Similar to the AZ91D alloy (Fig. 4.2c), the Mg3Zn1Ca alloy also shows the significant SCC susceptibility at the strain rate of  $1.2 \times 10^{-7} \text{ s}^{-1}$ , which was characterized by a drastic decrease in the magnitude of UTS and elongation-to-failure ( $\epsilon_f$ ) in *m*-SBF solution as compared to air (Fig. 4.14b). The decrease in mechanical properties, UTS and  $\epsilon_f$ , in *m*-SBF (as compared to the air) was less pronounced at the strain rate of  $5.0 \times 10^{-7} \text{ s}^{-1}$  (Fig. 4.14a) in comparison to those of at the strain rate,  $1.2 \times 10^{-7} \text{ s}^{-1}$  (Fig. 4.14b). This trend is also similar to the one for the AZ91D alloy (Fig. 4.2a and 4.2c).

Fig. 4.15 shows the fracture surface of the Mg3Zn1Ca alloy tested in air. At a higher magnification (Fig. 4.15b), the fracture surface reveals dimples as the primary feature.



**Fig. 4.15.** Typical fractograph of the Mg3Zn1Ca alloy tested in air: (a) overall fracture surface and (b) fracture surface showing dimples as the primary feature

Fractographs of the Mg3Zn1Ca alloy specimen tested in *m*-SBF at the strain rate of  $5.0 \times 10^{-7} \text{ s}^{-1}$  are shown in Fig. 4.16, which revealed pitting (Fig. 4.16a) and the areas of transgranular cracking as indicated by arrows (Fig. 4.16b).



**Fig. 4.16.** Fractograph of the Mg<sub>3</sub>Zn<sub>1</sub>Ca alloy tested in *m*-SBF solution at 37 °C at the strain rate,  $5.0 \times 10^{-7} \text{ s}^{-1}$ : (a) overall fracture surface, (b) fractograph showing transgranular cracking (arrows)

Similar to the features for the AZ91D alloy, the fractography of the Mg<sub>3</sub>Zn<sub>1</sub>Ca alloy tested at  $1.2 \times 10^{-7} \text{ s}^{-1}$  also revealed the considerable pitting and localized corrosion along the circumference (Fig. 4.17a) and transgranular cracking (Fig. 4.17b).

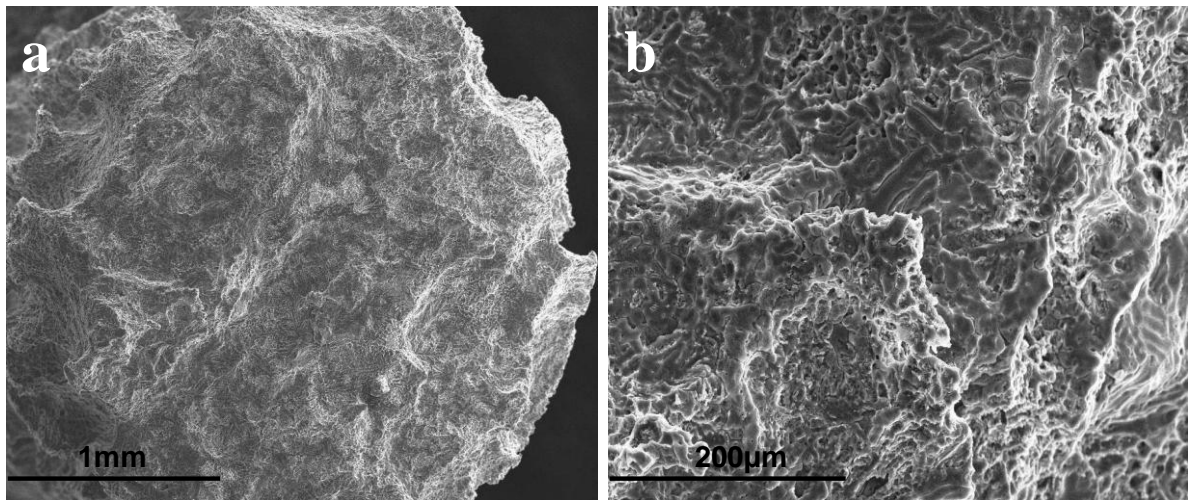


**Fig. 4.17.** Fractograph of the Mg<sub>3</sub>Zn<sub>1</sub>Ca specimen tested in *m*-SBF solution at 37 °C at the strain rate  $1.2 \times 10^{-7} \text{ s}^{-1}$ : (a) overall fracture surface, (b) fractograph showing transgranular cracking

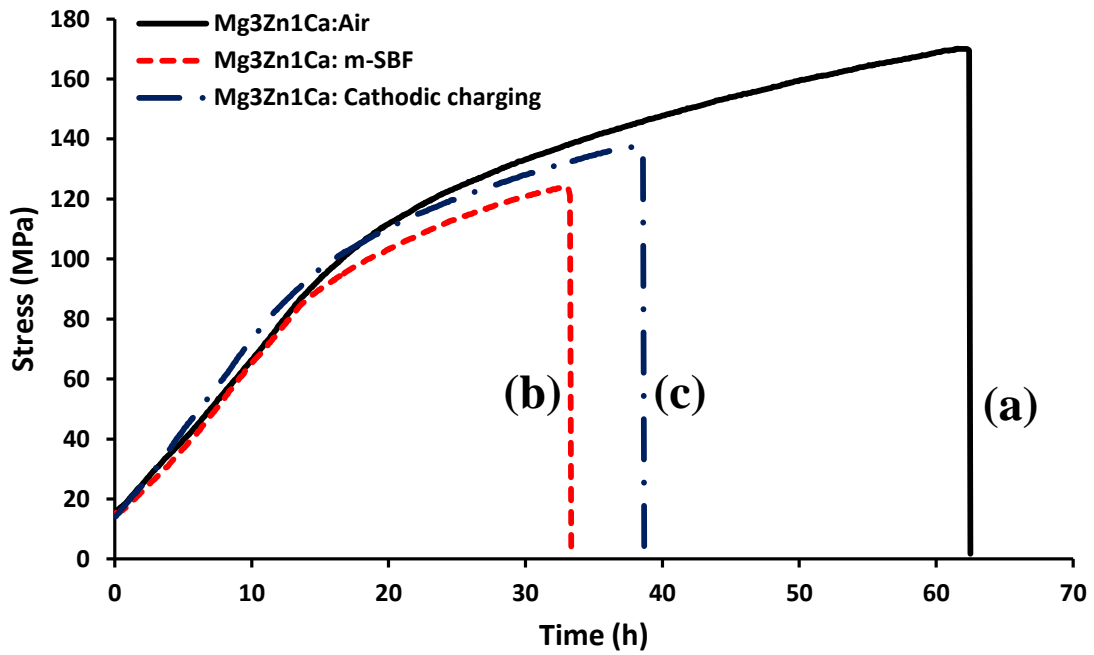
The SCC susceptibility indices for the AZ91D and Mg3Zn1Ca alloys at two strain rates are presented in Table 4.2. At the strain rate of  $1.2 \times 10^{-7} \text{ s}^{-1}$ , both the alloys showed considerably greater SCC susceptibility (i.e. lower susceptibility indices) than at the higher strain rate of  $5.0 \times 10^{-7} \text{ s}^{-1}$ , which is in agreement with the results reported by Dietzel et al. [110]. However, there is also a definite trend of greater SCC susceptibility for the Mg3Zn1Ca alloy as compared to the AZ91D alloy at both the strain rates.

Table 4.2: SCC susceptibility indices for AZ91D and Mg3Zn1Ca alloys

Alloy	Strain rate $5.0 \times 10^{-7} \text{ s}^{-1}$		Strain rate $1.2 \times 10^{-7} \text{ s}^{-1}$	
	I <sub>SCC</sub> (UTS) *	I <sub>SCC</sub> ( $\epsilon_f$ ) *	I <sub>SCC</sub> (UTS) *	I <sub>SCC</sub> ( $\epsilon_f$ ) *
AZ91D	$0.75 \pm 0.05$	$0.63 \pm 0.03$	$0.51 \pm 0.05$	$0.36 \pm 0.04$
Mg3Zn1Ca	$0.58 \pm 0.07$	$0.55 \pm 0.05$	$0.29 \pm 0.02$	$0.28 \pm 0.01$

\*Susceptibility indices are defined in Equations 3.1 and 3.2.

Similar to the AZ91D alloy, the slow strain rate tensile test on Mg3Zn1Ca alloy under cathodic charging was also performed at the strain rate of  $2.2 \times 10^{-7} \text{ s}^{-1}$ . As shown in Fig. 4.18, the specimen pulled at 200 mV negative to the open circuit potential (OCP) in *m*-SBF underwent substantial reduction in UTS and time-to-failure (Fig. 4.18c) as compared to the specimen pulled in air (Fig. 4.18a). However, the losses in mechanical properties (UTS and elongation-to-failure) during cathodic charging experiment (Fig. 4.18c) were less as compared to the specimen pulled in *m*-SBF at OCP (Fig. 4.18b). This suggested the combined mechanism of HASCC and anodic dissolution to cause SCC also in the case of Mg3Zn1Ca alloy, as observed in for the AZ91D alloy.



**Fig. 4.18.** Stress vs. time plots of Mg3Zn1Ca alloy in: (a) air (b) *m*-SBF at open circuit potential (OCP) and (c) *m*-SBF under continuous cathodic charging at 200 mV (vs. SCE) negative to OCP at the strain rate of  $2.2 \times 10^{-7} \text{ s}^{-1}$

In general, the transgranular SCC of magnesium alloys is reported to be associated with conditions causing electrochemical breakdown or mechanical rupture of protective films at the crack surface, which allows hydrogen to diffuse into the bulk of metal [35]. It is clear from the SCC susceptibility indices (Table 4.2) that the Mg3Zn1Ca alloy is comparatively more susceptible to SCC than the AZ91D alloy at a given strain rate. This can be attributed to the greater susceptibility of Mg3Zn1Ca alloy to pitting and localized corrosion as compared to the AZ91D (Figs. 4.4a, 4.5a, 4.16a and 4.17a). Also, the potentiodynamic polarization curves (Fig. 4.19) suggest that the cathodic current density is considerably higher for the Mg3Zn1Ca alloy as compared to the AZ91D, which indicates greater propensity of the Mg3Zn1Ca alloy to generate cathodic hydrogen. As a result, the Mg3Zn1Ca alloy may suffer greater hydrogen-assisted stress corrosion cracking (HASCC) than the AZ91D alloy.

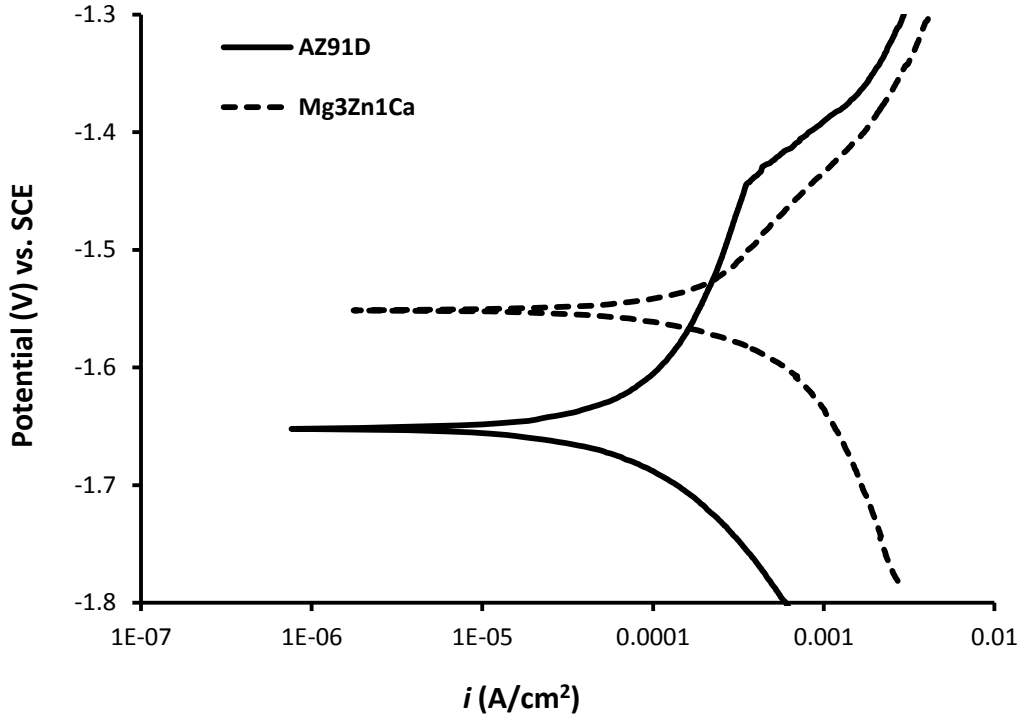


**Fig. 4.19.** Potentiodynamic polarization scans for the AZ91D and Mg3Zn1Ca alloy in the *m*-SBF solution at 37 °C.

#### 4.4 Conclusions

- AZ91D alloy was found to be susceptible to SCC in the physiological environment. A substantial decrease in mechanical integrity of AZ91D was observed in investigations using SSRT testing in *m*-SBF solution.
- Threshold stress intensity for SCC ( $K_{ISCC}$ ) of AZ91D alloy in *m*-SBF at 37 °C was determined to be 5.18 MPa m<sup>1/2</sup>, using the CNT technique. The crack growth rates were observed in the range of 10<sup>-9</sup> - 10<sup>-10</sup> m/s and found to be increasing with the applied stress intensity.
- The Mg3Zn1Ca alloy was found to be more susceptible to SCC as compared to the AZ91D at a given strain rate. The higher susceptibility of Mg3Zn1Ca alloy in comparison to AZ91D was attributed to its higher propensity towards localized



corrosion/pitting, which provided an active bare surface for H to enter into the matrix, causing greater hydrogen-assisted cracking. The SCC susceptibility also increased with decreasing strain rate for both the alloys.

- Common mode for SCC crack propagation of AZ91D and Mg<sub>3</sub>Zn<sub>1</sub>Ca alloys in *m*-SBF was the transgranular cracking, which is consistent with the literature on SCC of magnesium alloys in chloride solutions.
- The SSRT experiments under cathodic charging conditions revealed the SCC mechanism to be the combined effect of hydrogen-assisted stress corrosion cracking and anodic dissolution for both the alloys.

## **Chapter 5**

### **5. SCC of aluminium-free biodegradable magnesium alloys in the physiological environment**

#### **5.1 Introduction**

As discussed in earlier chapters, magnesium and its alloys are attractive biodegradable material because of their attributes of excellent biocompatibility, appropriate mechanical properties and suitable electrochemical characteristics [1, 12, 13, 24, 59]. The most common magnesium alloys generally contain aluminium (Al), such as AZ series alloys. However, due to serious neurotoxic effects of Al [195], there has been an increasing interest in Al-free magnesium alloys as the material of construction for biodegradable implant devices for short-to-medium term applications [29-32]. In fact, some of these Al-free magnesium alloys have successfully undergone animal trials and are currently being considered to be employed as cardiovascular stents [32-34]. However, it is yet to be established whether these alloys possess the desired resistance to cracking under the simultaneous influence of corrosive human body fluid and mechanical loading. In this study, Al-free biodegradable magnesium alloys, ZX50, WZ21 and WE43, especially designed for temporary implant applications, were evaluated for their resistance to stress corrosion cracking (SCC) in physiological environment. The alloys WZ21 and WE43 are reported to meet the requirements of moderate and homogenous degradation for stent applications [32, 196]. In addition, each of these alloys also exhibits high ductility (uniform elongation of 17–30 %) and appropriate strength (ultimate tensile strength: 250–350 MPa), which is necessary for an alloy to serve as suitable stent material. Stents require sufficient ductility for ease of fabrication and safe stent placement (ballooning requires a uniform strain optimally  $\geq 15$  %) and reasonable strength to offer adequate support to blood

vessel (i.e. ultimate tensile strengths  $\geq 250$  MPa) [181, 197]. Temporary implants for osteosynthesis also require good ductility for geometrical adaption by the surgeon [198]. Furthermore, these alloys have been shown to possess good cytocompatibility during both in-vitro and in-vivo animal studies [32, 33]. The WE43 alloy was particularly chosen as a reference alloy since it has already been employed for stent application and shown to meet other requirements for implant applications [199]. However, the resistance to environmentally-assisted cracking is one critical property that has not been characterized for these alloys.

In this chapter, the susceptibility to stress corrosion cracking of biodegradable and Al-free magnesium alloys (ZX50, WZ21 and WE43) has been investigated by slow strain rate tensile (SSRT) testing under simulated physiological conditions. SCC susceptibility of these alloys has been further confirmed by fractography. Also, an attempt has been made to explain the variation in SCC susceptibility of these alloys on the basis of their electrochemical and microstructural characteristics.

## **5.2 Experimental procedures**

The details about nominal chemical compositions of the alloys, testing environment, methodology for conducting SSRT testing and fractography have been provided in the Chapter 3.

The open circuit potentials for ZX50, WZ21 and WE43 alloys were determined to be  $-1.52$  V,  $-1.77$  V and  $-1.91$  V (vs. SCE), respectively.

## 5.3 Results and discussion

### 5.3.1 Microstructure

The optical micrographs for WZ21, WE43 and ZX50 alloys are shown in Fig. 5.1. Alloys exhibit fine-grained microstructures, with an average grain size of 7  $\mu\text{m}$  for WZ21, 15  $\mu\text{m}$  for WE43 and 4  $\mu\text{m}$  for ZX50. The smaller grain size, especially for WZ21 and ZX50 alloys, have been attributed to the restriction effect of alloying elements on the grain growth during solidification as well as grain boundary pinning by second phase particles during extrusion [181, 197]. The microstructures have been further characterized in the literature by the presence of second-phase particles, that are reported to be  $\text{Mg}_6\text{Zn}_3\text{Ca}_2$  in ZX50 [153], predominately  $\text{Mg}_{12}\text{YZn}$  in WZ21 [181], and  $\text{Mg}_{12}\text{Nd}$  and  $\text{Mg}_{14}\text{Nd}_2\text{Y}$  in WE43 [200].

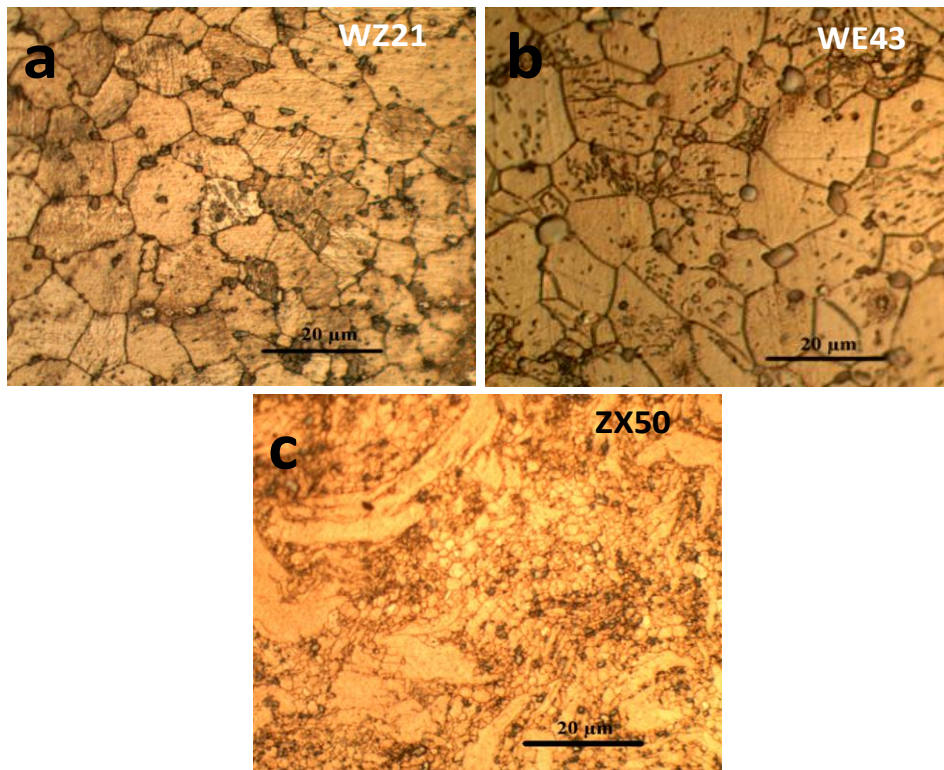


**Fig. 5.1.** Optical microstructure of as-received extruded magnesium alloys: (a) WZ21, (b) WE43 and (c) ZX50

### 5.3.2 Slow strain rate tensile (SSRT) testing

The stress vs. elongation plots for the ZX50, WZ21 and WE43 alloys under different environmental conditions at the strain rate of  $3.1 \times 10^{-7} \text{ s}^{-1}$  are shown in Figs. 5.2a, 5.2b and 5.2c, respectively. Table 5.1 compares a few mechanical properties of the alloys in air and *m*-SBF.

Table 5.1: Summary of mechanical properties of ZX50, WZ21 and WE43 alloys at the strain rate of  $3.1 \times 10^{-7} \text{ s}^{-1}$  (duplicate tests)

Alloy	In air		In <i>m</i> -SBF	
	UTS (MPa)	Elongation-to-failure (%)	UTS (MPa)	Elongation-to-failure (%)
ZX50	$352.5 \pm 17.7$	$21.2 \pm 2.3$	$257.0 \pm 5.6$	$3.8 \pm 0.03$
WZ21	$242.5 \pm 10.6$	$28.1 \pm 0.17$	$166.2 \pm 10.2$	$7.7 \pm 0.5$
WE43	$263.0 \pm 2.8$	$16.9 \pm 1.9$	$211.0 \pm 11.3$	$8.0 \pm 0.7$

The alloys ZX50 and WZ21 show an excellent combination of strength and ductility when tested in air. The enhancement in strength of these alloys has been attributed to the well-known strengthening influence of fine grain size (Fig. 5.1) [153]. Grain refinement is also reported to promote the non-basal dislocation modes of magnesium alloys [201], thereby, simultaneously improving their ductility. However, the considerably reduced elongations to failure (as suggested by the data in Table 5.1 and the plots in Fig. 5.2) indicate that each alloy possibly suffered embrittlement when tested in *m*-SBF solution. The loss in elongation to failure during testing in *m*-SBF was most pronounced in ZX50.

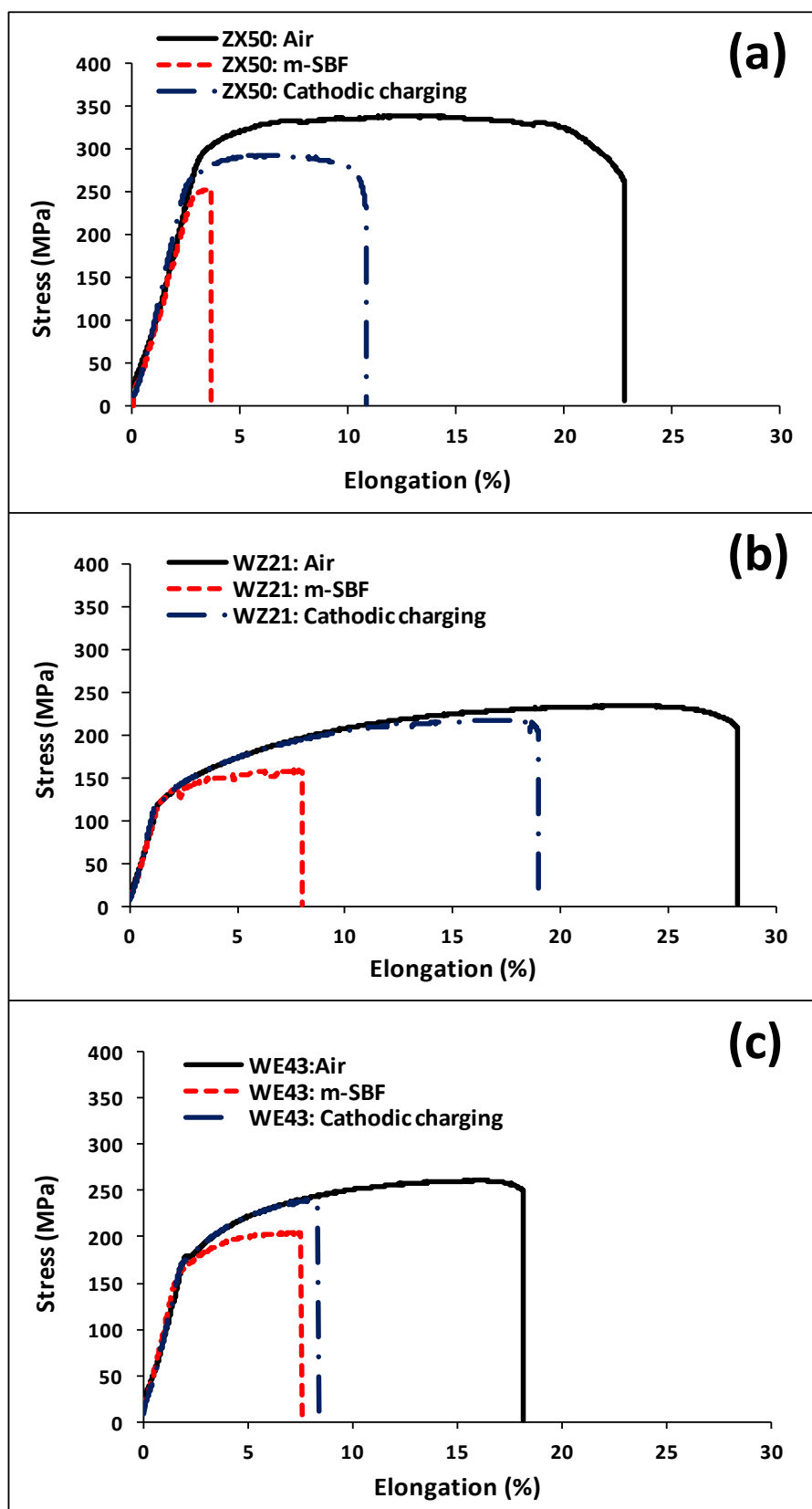


**Fig. 5.2.** Typical stress vs. strain plots in *m*-SBF and air, and under cathodic charging condition at the strain rate of  $3.1 \times 10^{-7} \text{ s}^{-1}$  for alloys: (a) ZX50, (b) WZ21 and (c) WE43

In order to quantify the SCC susceptibility of each of the alloys,  $I_{SCC}$  values were calculated (as described in Section 3.2.1) based on the SSRT data in the corrosive environment (*m*-SBF) and in an inert environment (air) presented in Table 5.1. The  $I_{SCC}$  data for each alloy are summarized in Table 5.2. The  $I_{SCC}$  for the WE43 alloy was relatively high compared to the ZX50 and WZ21 (particularly on the basis of elongation to failure), which suggests that WE43 is the most resistant of the three alloys to SCC in *m*-SBF solution, whereas ZX50 alloy is the least resistant. The lower resistance of ZX50 can be attributed to its higher susceptibility to localized corrosion/pitting in physiological environment. A recent study by Kraus et al. [33], that included animal trials and microfocus computed tomography ( $\mu$ CT), has demonstrated ZX50 alloy to suffer severe localized corrosion within 1 week, whereas WZ21 underwent uniform corrosion for up to 4 weeks.

Table 5.2:  $I_{SCC}$  indices for WZ21 and ZX50 alloys tested at a strain rate of  $3.1 \times 10^{-7} \text{ s}^{-1}$

Alloy	$I_{SCC}$	
	UTS	Elongation to failure
ZX50	$0.74 \pm 0.01$	$0.17 \pm 0.01$
WZ21	$0.68 \pm 0.01$	$0.29 \pm 0.01$
WE43	$0.79 \pm 0.02$	$0.44 \pm 0.04$

The susceptibility to SCC, as indicated by SSRT results, was confirmed by SEM fractography. For this purpose, the fracture surfaces of the alloys were examined for distinct features of SCC (i.e. transgranular/intergranular cracking).

### 5.3.3 Fractography

The overall fracture surface of the WE43 alloy tested in air (Fig. 5.3a) shows homogenous and fibrous features over the entire fracture surface. At a higher magnification (Fig. 5.3b), dimples were found, indicating ductile failure by mechanical overloading. The fracture surfaces of the WZ21 and ZX50 alloys tested in air revealed similar ductile features (i.e. dimples) over the entire fracture surface.

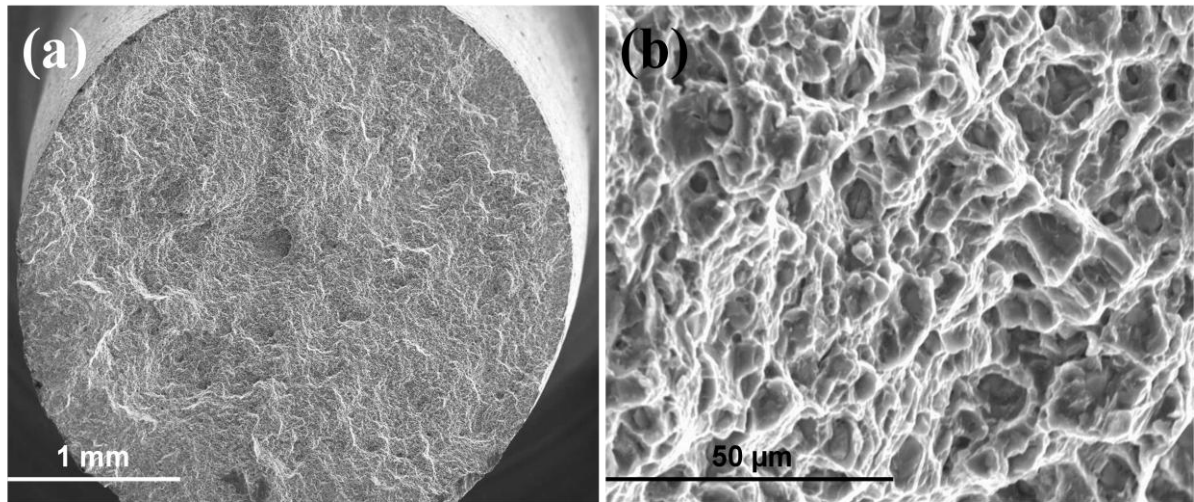


**Fig. 5.3.** Fractograph of WE43 specimen tested in air: (a) overall fracture surface, and (b) evidence of dimple formation

The fracture surface of the ZX50 alloy tested in the *m*-SBF is shown in Fig. 5.4. The specimen strained in *m*-SBF showed significantly different features to those tested in air. Overall fracture surface (Fig. 5.4a) of the specimen tested in *m*-SBF has two distinct regions: SCC zone and mechanical failure zone. The features of these regions become clearer at higher magnifications. Fig. 5.4b shows transgranular cracks (bright arrows) running from the circumference confirming the occurrence of SCC. Fig. 5.4b also shows the transition from SCC zone to mechanical overloading region. It is typical of an alloy susceptible to SCC that when a critical SCC crack length is achieved, the mechanical overloading takes over in the final stage of cracking, as evidenced from the dimple formation in Fig. 5.4c.



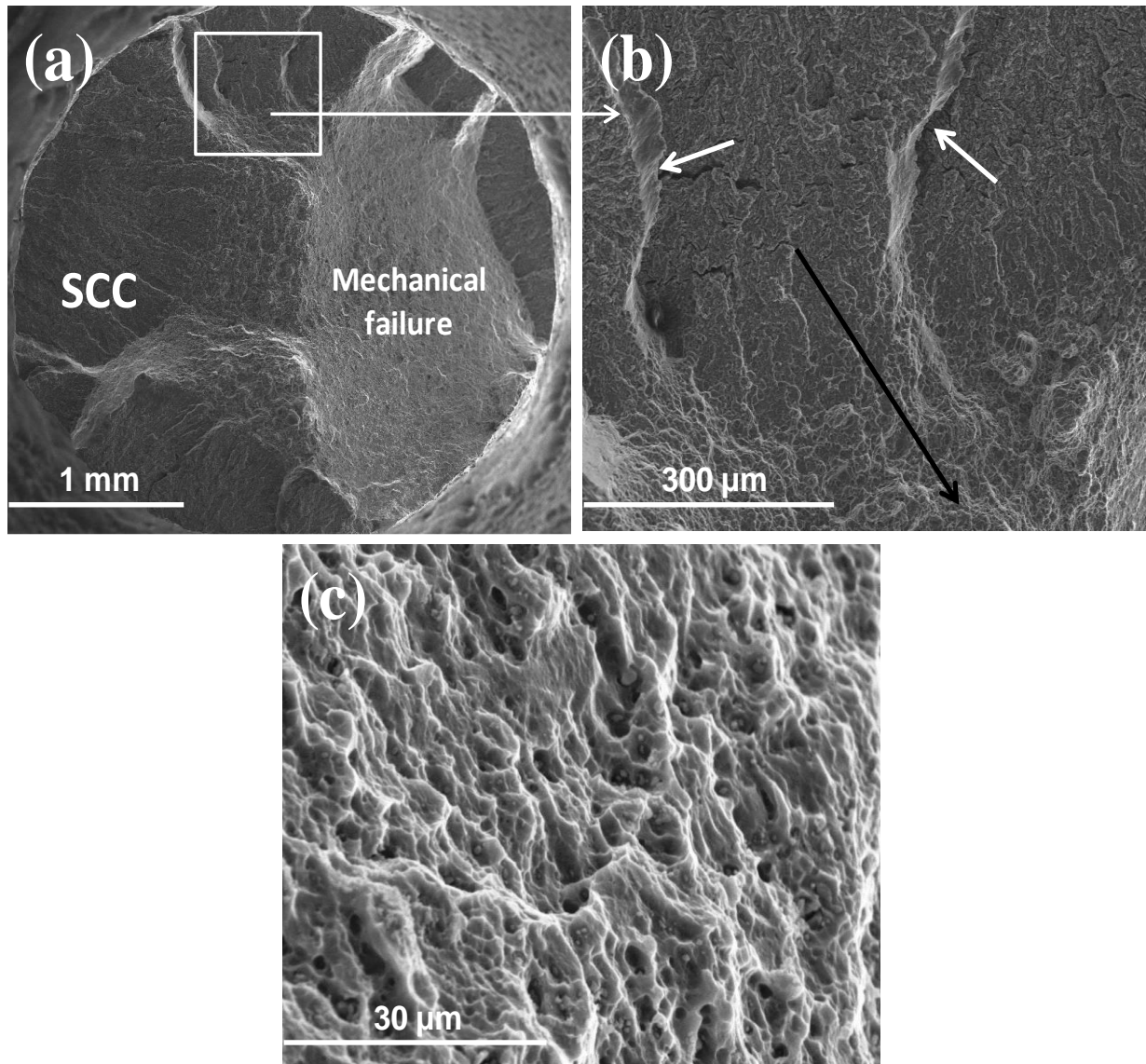


**Fig. 5.4.** Fractograph of the ZX50 alloy tested in the *m*-SBF solution at 37 °C: (a) overall fracture surface, (b) transgranular cracking in the SCC zone (dark arrow indicates crack propagation direction and bright arrows indicate areas of transgranular cracking) and (c) mechanical failure zone showing the dimples

Fractographic features similar to those for the ZX50 alloy showing the transgranular cracking in the circumferential areas were also observed in the case of the WZ21 alloy (Fig. 5.5) and WE43 alloy (Fig. 5.6). However, for the WE43 alloy, the SCC region also displays areas with features for intergranular cracking in addition to transgranular cracking (Fig. 5.6b). This mixed feature is consistent with the fractographic evidences reported in the literature for rare-earth

containing magnesium alloys [18]. The intergranular crack propagation in WE43 alloy can be attributed to the precipitates preferentially located at the grain boundary, which would accelerate the electrochemical dissolution along the grain boundaries and cause some intergranular SCC [18, 200].

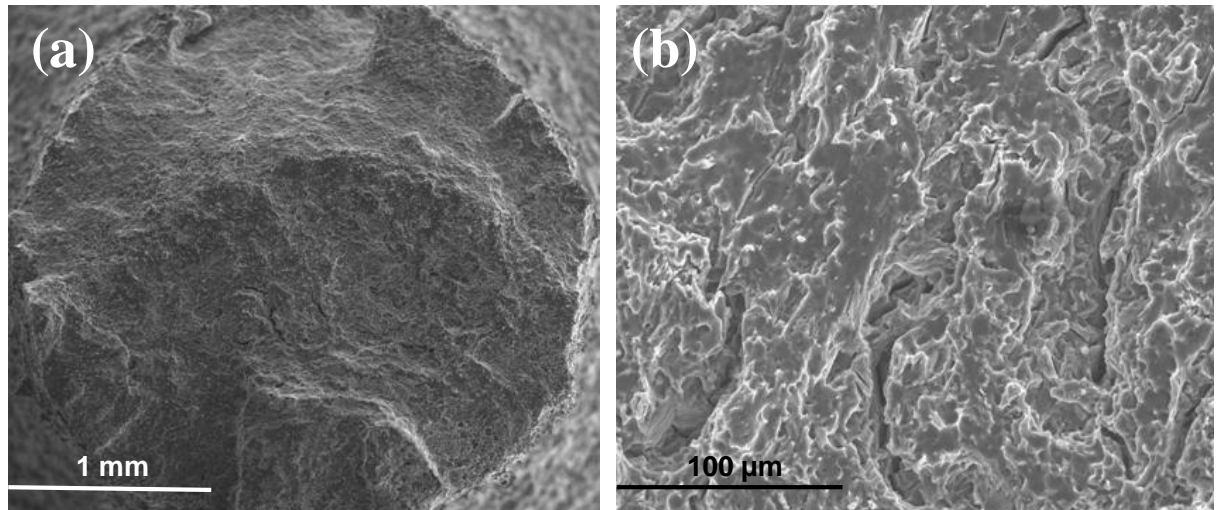


**Fig. 5.5.** Fractograph of the WZ21 alloy tested in the *m*-SBF at 37 °C: (a) overall fracture surface, (b) evidence of transgranular cracking

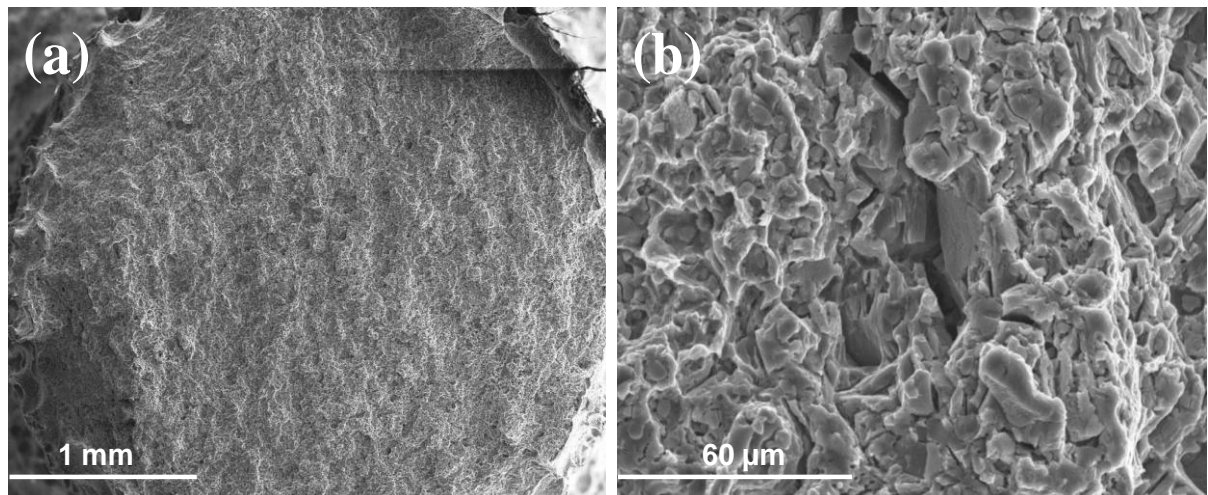


**Fig. 5.6.** Fractograph of the WE43 alloy tested in the *m*-SBF at 37 °C: (a) overall fracture surface, (b) evidence of transgranular cracking and intergranular cracking

It is reported in the literature that the crack morphology is influenced by the grain size. For fine grained magnesium alloys, SCC is exclusively transgranular, whereas, for coarse grained magnesium alloys, SCC can be mixed transgranular and intergranular [36]. The fractography results of this study are in agreement with the reported literature [36] as the fine grained magnesium alloys, ZX50 and WZ21, undergo exclusive transgranular cracking (Fig. 5.4b and 5.5b) while significantly coarser alloy, WE43, undergoes mixed mode of failure (Fig. 5.6b).

#### **5.3.4 Cathodic charging SSRT experiments**

The predominant feature of transgranular cracking of magnesium alloys has generally been attributed to the mechanism involving hydrogen, i.e. hydrogen assisted stress corrosion cracking (HASCC) [35, 36]. The transgranular cracking observed in each alloy may be attributed to the electrochemical breakdown or mechanical rupture of protective films, which allows the evolved hydrogen to enter into the alloy matrix, eventually, causing the embrittlement and premature fracture [35, 36].

Magnesium alloys corrode very quickly in chloride-containing solutions, including SBF and generate considerable hydrogen due to the negative difference effect [69]. Magnesium alloys also readily undergo pitting and localized corrosion. The decrease in mechanical properties (elongation to failure and UTS) during the SSRT experiment at open circuit conditions in the *m*-SBF solution (Fig. 5.2 and Table 5.1) can thus be attributed to general and localized corrosion or HASCC or both. To ascertain the cause of SCC, a few SSRT tests were performed on each alloy under continuous cathodic charging conditions (200 mV negative to the open circuit potential) in *m*-SBF solution, while the alloy sample was continuously pulled at the strain rate of  $3.1 \times 10^{-7} \text{ s}^{-1}$ . Cathodic current densities were also measured for WZ21 and WE43 during SSRT experiments under cathodic charging conditions. The current densities were in the range of 0.5 - 1.5 A/cm<sup>2</sup> for WZ21 and 2.5 – 3.5

A/cm<sup>2</sup> for WE43 for most of the experimental duration (Fig. 5.7). Because the presence of oxygen does not contribute to the cathodic kinetics during corrosion of magnesium alloys [6, 202], the only cathodic partial reaction for magnesium alloys is  $H^+ + e^- = H$  [64]. Higher cathodic current density therefore corresponds to a greater hydrogen evolution. As seen in Fig. 5.2, each of the three alloys underwent a substantial loss in elongation to failure and UTS under the continuous cathodic charging conditions, which suggests the role of hydrogen in premature cracking (i.e. HASCC). WE43 also showed considerably greater propensity for generating atomic hydrogen (as evident from its relatively higher cathodic current density throughout the experiment; see Fig. 5.7), possibly suggesting the highest contribution of HASCC in the cracking of this alloy. In fact, it seems that HASCC is the predominant cracking mechanism for WE43 even in the absence of cathodic charging, since the elongation to failure was similar in the SSRT experiments with and without cathodic charging in the m-SBF (Fig. 5.2c).

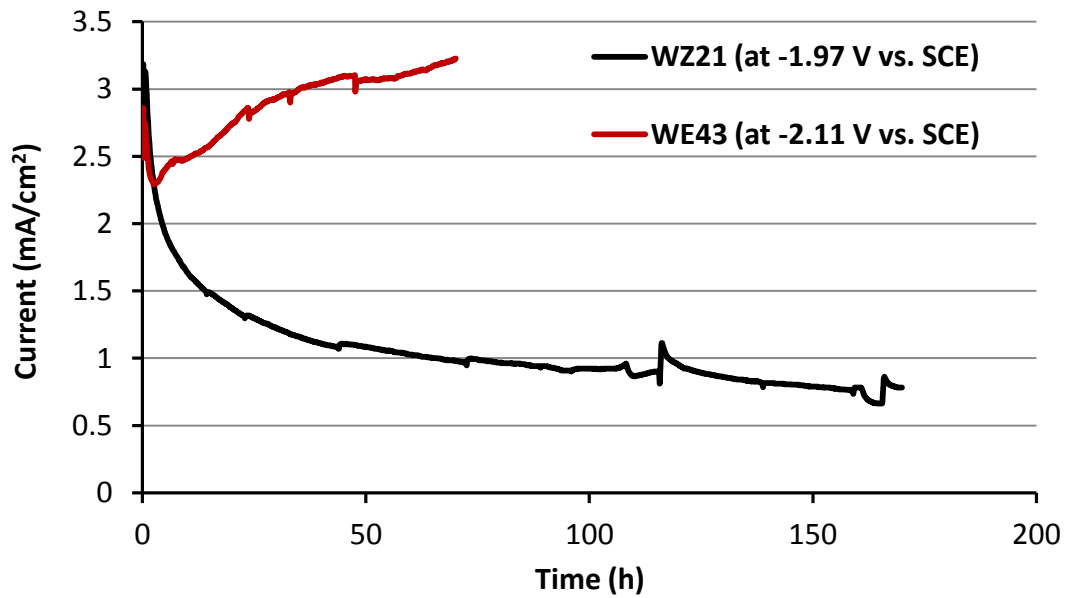


**Fig. 5.7.** Evolution of cathodic current density for WZ21 and WE43 during cathodic charging SSRT experiments

For each alloy, the maximum loss in UTS and the least elongation to failure (Fig. 5.2) were observed in the case of specimens tested in the *m*-SBF under the open circuit condition (and not under the cathodic charging conditions that provided maximum hydrogen), which indicates a combined HASCC and anodic dissolution effects. A similar combined mechanism has been reported for AZ91D and Mg3Zn1Ca alloys tested in the *m*-SBF (Chapter 4). However, comparison of elongation to failure under the open circuit and cathodic charging conditions for the three alloys (Fig. 5.2) have shown that the contribution of anodic dissolution was the least for WE43 and much higher for ZX50 and WZ21 alloys.

The mechanism described above suggests the critical role of pits as the common stress-intensity points and SCC initiation sites. The most favourable sites for localized anodic dissolution (pitting) are the areas adjacent to the microstructural or electrochemical heterogeneities, such as second phase particles, impurities and inclusions [35, 97]. Such localized dissolutions also provide easier sites for hydrogen entry into the matrix which has well established embrittling effect. Magnesium and its alloys can generate considerable amount of hydrogen even at the open circuit potential (OCP) besides undergoing anodic dissolution. At OCPs, the concomitant effect of anodic dissolution and hydrogen cause the maximum reduction in elongation to failure for each alloy (Fig. 5.2). But, under cathodic charging conditions, anodic dissolution is suppressed thereby suppressing the localized pitting. Consequently, the reduction in elongation to failure was less pronounced for each alloy in cathodic charging SSRT experiments as compared to the SSRT tests at OCP in *m*-SBF (Fig. 5.2). There are a few hydrogen embrittlement models reported in the literature, mainly hydrogen enhanced localized plasticity (HELP), hydrogen enhanced decohesion (HEDE), delayed hydride cracking (DHC) and adsorption-induced dislocation emission (AIDE). It will be interesting to identify which of these operates in the present system. However, it is clear that any measure to delay the localized dissolution (pitting), such as by

employing the suitable coating, will retard both the dissolution and hydrogen-assisted stress corrosion cracking.

SSRT testing is an accelerated laboratory technique for characterizing SCC. However, for determination of the stress corrosion crack growth rate for predicting the service life of the components susceptible to SCC, it is essential to conduct a fracture mechanics-based damage tolerance design analysis (as discussed in Chapters 2, 3 & 4), which will also include determination of  $K_{ISCC}$ . Such studies are particularly necessary because implant devices often have sharp corners and protrusions, which can readily act as SCC initiators.

## 5.4 Conclusions

In this study, a few novel biodegradable magnesium alloys (ZX50, WZ21 and WE43) were investigated using SSRT testing in order to evaluate their stress corrosion cracking susceptibility in the physiological environment of *m*-SBF. The following general conclusions may be drawn:

- 1) All the alloys revealed good mechanical properties when tested in air, which was attributed to the fine grain size of the alloys. In contrast, each alloy suffered significant embrittlement when tested in *m*-SBF, as suggested by a considerably lower elongation to failure observed in *m*-SBF as compared to the air.
- 2) The ZX50 alloy was found to be more susceptible to SCC than WZ21 and WE43, which is consistent with its reported propensity towards localized corrosion.
- 3) Fractography confirmed the ductile failure in case of all the alloys when tested in air, but also revealed the distinctive features of SCC, i.e. transgranular/intergranular cracking when tested in the *m*-SBF.

- 4) The SCC mechanism for these extruded alloys was the combined effect of HASCC and anodic dissolution. The major contribution of SCC in WE43 alloy was from HASCC due to higher magnitude of cathodic current density (i.e. greater cathodic hydrogen generation), while the major contribution of SCC in WZ21 alloy was due to anodic dissolution.

## **Chapter 6**

### **6. Novel graphene-calcium carbonate coating on AZ91D for resistance to localized corrosion and assisted degradation in mechanical property**

#### **6.1 Introduction**

As described in Chapters 2, 4 and 5, magnesium alloys undergo accelerated corrosion in the physiological environment and may lose their mechanical integrity during load bearing applications primarily due to the phenomenon of SCC. It has been also established in Chapters 4 and 5 that Mg alloys are susceptible to SCC in human body fluid.

The most common way to improve the SCC resistance is to reduce the amount of aggressive ions in the corrosive solution as well as the mechanical loading, both of which would not be possible in the case of biomedical implant applications. However, development of corrosion resistant alloys and surface modification with biocompatible coatings may be feasible solutions for achieving desired level of corrosion/cracking resistance. Since choices of alloying elements for developing biodegradable Mg alloys with good degradation resistance remain limited, surface modification of Mg alloys with biocompatible coatings appears to be an attractive alternative. As discussed in Chapter 2 (Section 2.8), several biocompatible coatings based on calcium phosphate compounds (brushite, hydroxyapatite, octacalcium phosphate) have been extensively applied on Mg alloys in order to improve their corrosion resistance and biocompatibility. However, since these ceramic calcium phosphate compounds are brittle in nature [51], it is highly probable that these coatings are likely to suffer disruptions during the load bearing implant applications, thus exposing the substrate materials, and possibly leading



to accelerated localized corrosion and fracture. Therefore, it is attractive to explore advanced synthetic biomaterials for depositing robust coatings on the biodegradable Mg alloys.

Calcium carbonates ( $\text{CaCO}_3$ ) and hydroxyapatites [ $\text{Ca}_{10}(\text{PO}_4)_6(\text{OH})_2$ ] are the widely studied biominerals [51, 179, 203, 204]. The fabrication of biominerals that mimic the structure and strength of bone or exhibit bone-forming ability is a topical subject in materials and biomedical sciences. In recent times, graphene, an  $\text{sp}^2$ -bonded carbon layer of graphite with a thickness of single atom, has also triggered a widespread research interest due to its excellent thermal, mechanical and electrical properties [172, 205]. It would also be highly desirable to exploit the advantageous and exceptional properties of graphene in the field of biomedical sciences. In this context, Nayak et al. [206] demonstrated that graphene can be used as a biocompatible scaffold for the proliferation of human mesenchymal stem cells, even accelerating their differentiation into bone cells. Accordingly, the notion of hybridization of bone bioactive minerals (e.g.,  $\text{CaCO}_3$ , hydroxyapatite) with graphene can be of huge importance in potential medical applications.

Graphene has been used in preparing high strength composite and electronic materials [207, 208], but the interaction of graphene with biominerals to form bioactive compounds is rarely researched. In a very recent study, Kim et al. [178] successfully hybridized bioactive calcium carbonate and graphene nanosheets and subsequently fabricated biocompatible, self-standing hybrid films of graphene- $\text{CaCO}_3$  (vaterite - one of the thermodynamically most unstable polymorphs of calcium carbonate [209]) by means of  $\text{CO}_2$ -injection. More importantly, they also observed the formation of graphene-incorporated hydroxyapatite after incubation of the prepared film in SBF solution (since the main component of the film, i.e. vaterite, is assumed to be inorganic precursor for inducing the formation of carbonated apatite [210-212]). In addition, the film composed of this hybrid material exhibited excellent cell viability and proliferation rate, suggesting the novel prospects of utilizing graphene-based biominerals in clinical and biomedical applications.

Although, Kim et al. [178] were successful in developing the free standing graphene-CaCO<sub>3</sub> film, it was not yet investigated whether the similar film can be produced on the metal surface as a coating with the intention of providing excellent biocompatibility, and possibly, improving corrosion resistance. In the present work, the main aim was to develop a graphene-calcium carbonate coating on a magnesium alloy, AZ91D, using an economical conversion route. The conversion route for depositing coating also provides distinct advantages such as: (i) ease of operation, (ii) ability to coat complex shapes such as screws, stents and pins, and (iii) low cost and low temperature process. The electrochemical degradation kinetics of the coating has been systematically investigated using electrochemical impedance spectroscopy (EIS). Furthermore, it is reasonable to assume that the presence of the mechanically strong graphene network, which promotes the formation of vaterite, may also help in improving the SCC resistance in physiological environment. Therefore, the mechanical integrity of the graphene-CaCO<sub>3</sub> coated specimens has also been investigated in this study.

## **6.2 Experimental**

### **6.2.1 Material and test environment**

AZ91D alloy used in this study is described in Chapter 3 and its nominal chemical composition is shown in Table 3.1. All the electrochemical and mechanical integrity tests were carried out in the physiological environment of *modified* simulated body fluid (*m*-SBF) at a temperature of 37° C.

### 6.2.2 Coating method

Before the coating process, the rectangular coupons ( $3\text{ cm} \times 2\text{ cm} \times 0.4\text{ cm}$ ) of AZ91D were sectioned from the as-cast billet. The specimen coupons were ground progressively on SiC papers up to 2500 grit followed by rinsing with acetone and de-ionized water before coating deposition.

The graphene oxide (GO) solution ( $\sim 0.16\text{ wt. \%}$ ) was prepared using modified Hummers' method [213, 214] followed by ultrasonication for 1 hour and centrifugation at 3000 rpm for 30 minutes. In the mean time, 0.3 M calcium chloride dihydrate ( $\text{CaCl}_2 \cdot 2\text{H}_2\text{O}$ ) solution (180 mL) was mixed with 0.6 M ammonium hydroxide ( $\text{NH}_4\text{OH}$ ) solution (120 mL). The prepared GO dispersion (180 mL) was then added to this solution mixture followed by a vigorous stirring. The pH of the coating bath was 11.7. Rectangular coupons of AZ91D were then immersed in the final solution mixture for 1 h at room temperature. While the specimens were immersed in the coating solution, carbon dioxide ( $\text{CO}_2$ ) gas was purged with a flow rate of  $\sim 1\text{ L/minute}$  to facilitate the formation of GO- $\text{CaCO}_3$  coating on AZ91D. During the coating deposition, the solution was also stirred slowly at 120 rpm. The resulting GO- $\text{CaCO}_3$  coated specimens were immersed in a reducing mixture of 0.15 mL of hydrazine (35 wt %), 1.05 mL of  $\text{NH}_4\text{OH}$  (0.28 wt %) and 300 mL of water at  $95\text{ }^\circ\text{C}$  for 1 h. This reduction of GO- $\text{CaCO}_3$  coated specimens resulted in the formation of graphene- $\text{CaCO}_3$  composite coating on the AZ91D.

As a control, only- $\text{CaCO}_3$  coating (i.e. without graphene) was also developed on the AZ91D using the same process where  $\text{CO}_2$  gas was purged for 1 h into the reaction mixture of  $\text{CaCl}_2$  and  $\text{NH}_4\text{OH}$  without GO sheets. After coating deposition, coated specimens were heated in an oven at  $95\text{ }^\circ\text{C}$  for 1 h.

### 6.2.3 Coating characterization

The coating morphology was characterized using the JEOL 7001F scanning electron microscope (SEM) operating at 15 keV. The chemical constituents of the deposited coating were analysed by X-ray diffraction (XRD) using Cu K $\alpha$  line generated at 40 kV and 25 mA at a scan rate of 2°/ minute and a step size of 0.02°.

For characterization of carbonate structure present within the coating, attenuated total reflectance-Fourier transformed infrared spectra (ATR-FTIR) were collected in the wavelength range of 600-2500 cm<sup>-1</sup> using the PerkinElmer spectrum 100 series spectrometer. For each specimen, 128 scans were performed with a spectral resolution of 8 cm<sup>-1</sup>.

The presence of graphene in the graphene-CaCO<sub>3</sub> coated specimen was confirmed using Raman spectroscopy. Raman spectra were obtained using a Renishaw Confocal micro-Raman Spectrometer equipped with a HeNe (632.8 nm) laser operating at 10 % power. Extended scans (10 s) were performed between 100 and 3200 wave numbers with a laser spot size of 1  $\mu$ m.

### 6.2.4 Electrochemical testing

In order to systematically investigate the corrosion kinetics of different specimens (bare specimen, graphene-CaCO<sub>3</sub> coated and only-CaCO<sub>3</sub> coated), electrochemical impedance spectroscopy (EIS) and potentiodynamic polarization scans were performed in *m*-SBF solution at 37 °C. The details of these electrochemical characterization techniques have been described in Chapter 3, Section 3.3.

### 6.2.5 Post-corrosion analysis

Post-corrosion morphologies of the coated specimens were observed under the JEOL 7001F scanning electron microscope as described in Chapter 3, Section 3.4.

### 6.2.6 Mechanical integrity of coated specimens

The conventional slow strain rate tensile testing, where straining is applied while a specimen is immersed in a corrosive solution (that was extensively employed for SCC testing, as discussed in Chapter 4 and 5), may not be suitable for evaluating the SCC susceptibility of a coated system. Since SSRT is an accelerated laboratory testing (due to fast dynamic loading), coating may quickly crack/break during testing. Consequently, the effect of coating on the mechanical integrity of the alloy cannot be studied. Accordingly, for evaluation of the mechanical integrity of the graphene-CaCO<sub>3</sub> coated alloy in this study, coated samples were first immersed in the *m*-SBF solution for 120 h, and then subjected to immediate straining in air at a strain rate of  $3.1 \times 10^{-7} \text{ s}^{-1}$ . Ultimate tensile strength (UTS) for pre-immersed specimens pulled in air was used as a parameter for evaluating the susceptibility to SCC. As mentioned in Chapter 2, corrosion deteriorates the mechanical integrity of Mg alloys; the pre-exposure time was therefore chosen to be sufficiently long to cause the visible corrosion on the specimen surface.

For the comparison purpose, the similar pre-exposure followed by straining in air was also performed on the bare specimen.

## 6.3 Results and discussion

### 6.3.1 Coating characterization

The macrographs of the graphene-CaCO<sub>3</sub> coated and only-CaCO<sub>3</sub> coated specimens are shown in Fig. 6.1. The graphene-CaCO<sub>3</sub> coating on AZ91D appeared to be light grey in colour while a brown coloured surface appearance was observed in the case of only-CaCO<sub>3</sub> coated alloy (i.e., coating produced without any graphene oxide solution in the coating bath).

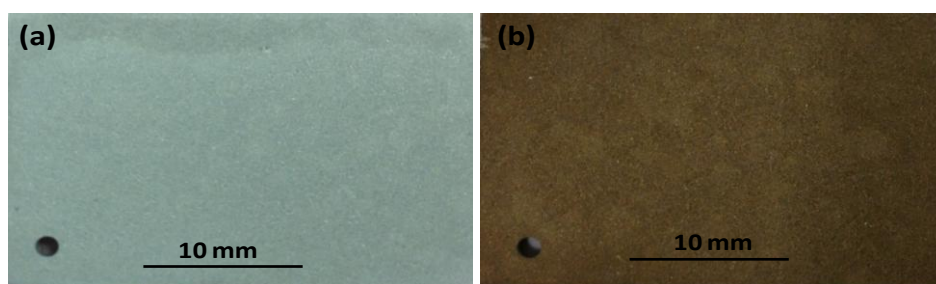


**Fig. 6.1.** Surface appearance of: (a) graphene- $\text{CaCO}_3$  coating and (b) only- $\text{CaCO}_3$  coating, on AZ91D

The overall SEM morphology of the graphene- $\text{CaCO}_3$  coating deposited on AZ91D is shown in Fig. 6.2a. The cracks in the coating are primarily the result of dehydration due to presence of high vacuum in the SEM chamber [215]. The alloy surface was mineralized by the unstable polymorph of calcium carbonate, which are of spherical shape (i.e. vaterite), as shown in Fig. 6.2b. The spherical  $\text{CaCO}_3$  (vaterite) were interconnected by a dispersed graphene network (Fig. 6.2b). It is favourable to form thermodynamically unstable polymorph of calcium carbonates, i.e. vaterite phase (hexagonal crystal that typically grows in a spherical form), rather than the formation of stable calcite phase with rhombohedral crystalline structure that does not undergo any further phase transition in aqueous solution [216]. The cross sectional microscopy of the graphene- $\text{CaCO}_3$  coated specimens revealed the coating thickness to be  $\sim 7$ - $10\ \mu\text{m}$ , and suggested a reasonable coating adherence to the alloy substrate (Fig. 6.2c). In contrast, the only- $\text{CaCO}_3$  coating (without any graphene) deposited on AZ91D shows a predominant presence of rhombohedral calcite crystal (Fig. 6.2d) and just a few vaterite microspheres. This also suggests that the presence of GO/graphene network in fact stabilized the vaterite phase. The stabilization of vaterite microspheres in graphene- $\text{CaCO}_3$  coating is attributed to the high mechanical strength of the GO network surrounding vaterite, which will retard their crystal growth and morphological transformation into rhombohedral calcite phase [178]. Furthermore, it has been reported that carboxyl-functionalized carbon nanotubes (CNT-COOH) can favour the formation of vaterite phase through the strong electrostatic interaction

between carboxyl groups of CNT-COOH and metallic  $\text{Ca}^{2+}$  ions, thus making the dissolution of vaterite spheres difficult [217]. It is reasonable to infer in this study that the thermodynamically unstable vaterite microspheres could be similarly stabilized by wrapping with GO sheets due to favourable electrostatic interaction between  $\text{Ca}^{2+}$  in vaterite and functional groups (such as hydroxyl, epoxy, carboxylic acid, and carbonyl) of GO sheets [178, 179, 218, 219]

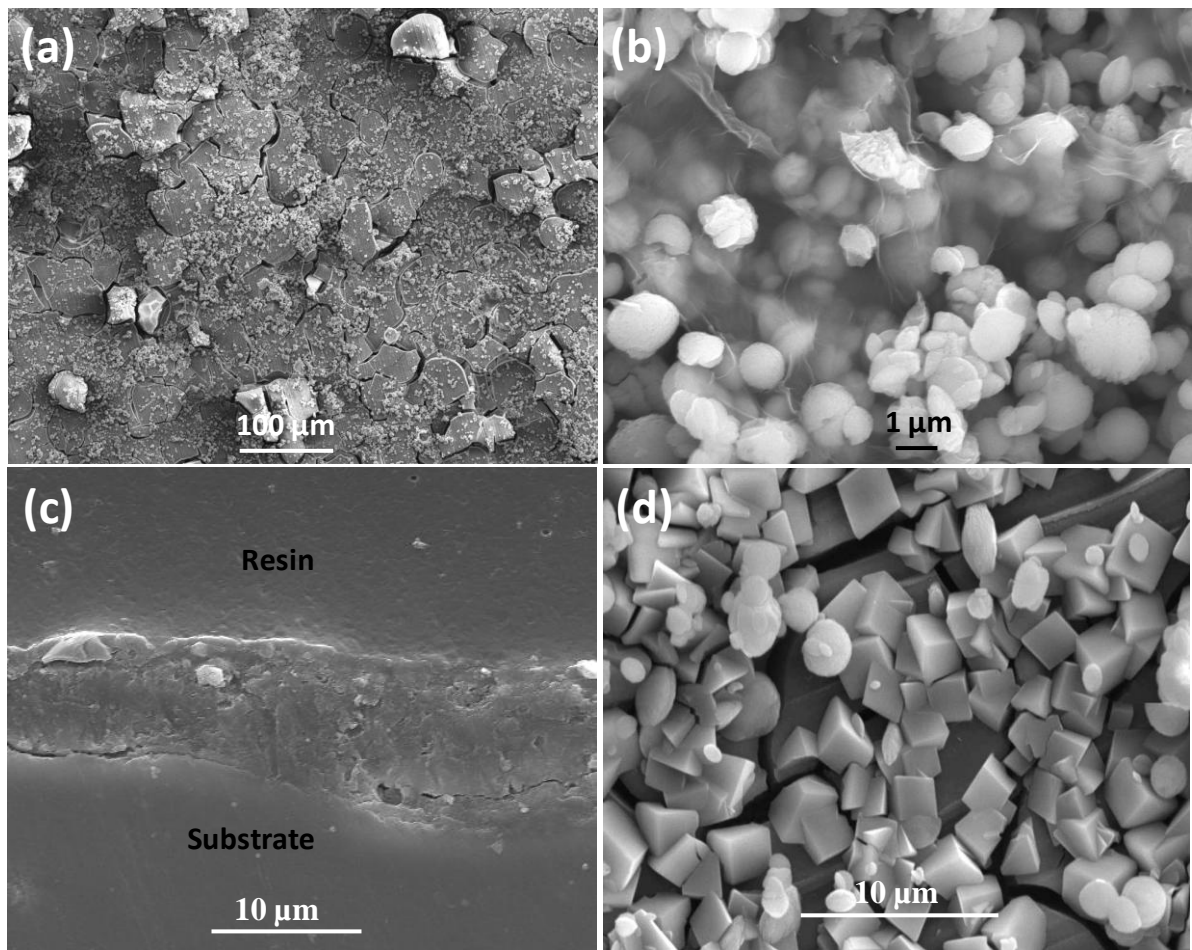


**Fig. 6.2.** (a) Overall SEM morphology of graphene- $\text{CaCO}_3$  coating, (b) a higher magnification SEM image showing the wrapping of vaterite microsphere by a graphene network, (c) cross sectional microscopy of graphene- $\text{CaCO}_3$  coating on AZ91D, and (d) SEM morphology of only-  $\text{CaCO}_3$  (calcite) coating formed on AZ91D alloy in absence of the graphene network

XRD scans for the graphene- $\text{CaCO}_3$ , only- $\text{CaCO}_3$  coated specimens and bare AZ91D are shown in Fig. 6.3. The peaks at  $32.7^\circ$ ,  $41.7^\circ$  and  $43.8^\circ$  for vaterite (ICDD PDF card number 033-

0268) were clearly shown in the spectra for graphene-CaCO<sub>3</sub> coated specimen as compared to the peaks at 29.4 and 48.5° for rhombohedral calcite (ICDD PDF card number 047-1743) in only-CaCO<sub>3</sub> coated specimen.

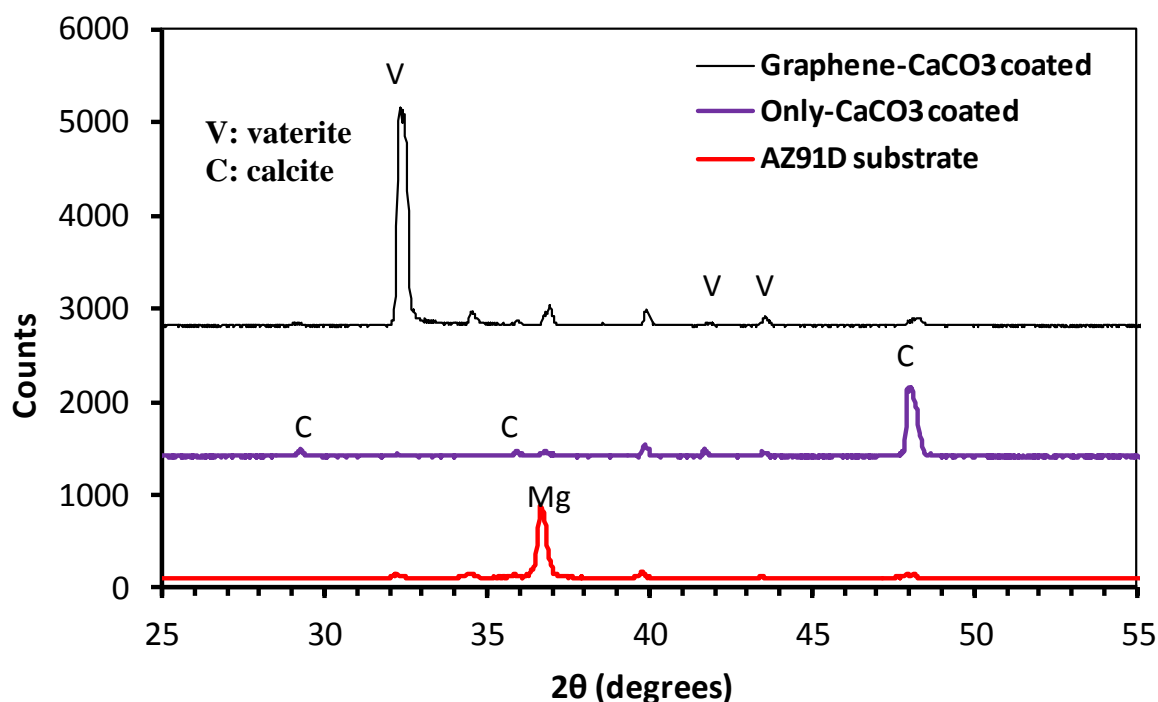


**Fig. 6.3.** XRD scans of graphene-CaCO<sub>3</sub> and only-CaCO<sub>3</sub> coated specimens as compared to the AZ91D substrate

Further investigations by ATR-FTIR spectroscopy on the graphene-CaCO<sub>3</sub> coated specimens demonstrated the carbonate absorption near 872 cm<sup>-1</sup> and the split band at around 1400–1485 cm<sup>-1</sup> by an asymmetric stretch of carbonate, confirming the presence of carbonate groups within the structure (Fig. 6.4a). Raman spectroscopy was performed in order to confirm the presence of graphene network in the graphene-CaCO<sub>3</sub> coated AZ91D specimens, as shown in Fig. 6.4b. It revealed signature peaks of the D band (disorder band caused by the graphite edges) at 1345 cm<sup>-1</sup> and G band (in-phase vibration band of graphite lattice) at 1590 cm<sup>-1</sup>, suggesting the discontinuous presence of graphene network on the coated AZ91D specimens [220].



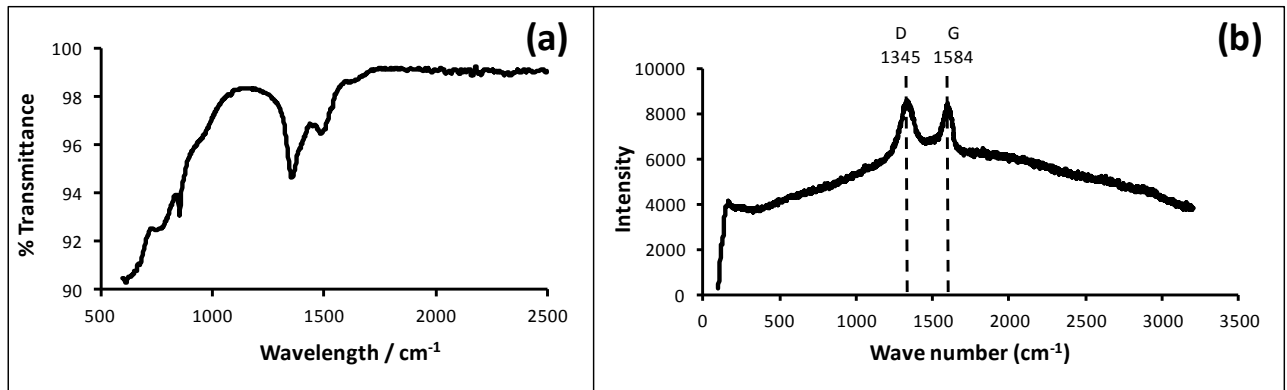


**Fig. 6.4.** (a) FTIR and (b) Raman spectra of graphene- $\text{CaCO}_3$  coated specimen

### 6.3.2 Electrochemical corrosion

The kinetics of time-dependent electrochemical degradation of the graphene- $\text{CaCO}_3$  coated AZ91D was studied using electrochemical impedance spectroscopy (EIS). Fig. 6.5 presents the evolution of impedance spectra (Nyquist plots) of the graphene- $\text{CaCO}_3$  coated AZ91D alloy after immersion for different durations as well as the bare specimen after 2 h of immersion in *m*-SBF. The Nyquist plots for the coated and bare alloy consist of two capacitive loops. The capacitive loop in the higher frequency range relates to the charge transfer processes, whereas the loop in the intermediate/lower frequency range corresponds to the mass transfer processes [188]. The polarization resistance is determined by combined diameter of both the capacitive loops [176]. On this basis, it is evident that the polarization resistance of the graphene- $\text{CaCO}_3$  coated specimens is  $\sim 3$  times greater than the bare AZ91D even after 120 h of immersion in *m*-SBF. The combined as well as the individual diameter of the coated specimen increased gradually with an increase in immersion time till 24 h (Fig. 4), indicating a gradual improvement in corrosion resistance provided by the graphene- $\text{CaCO}_3$  coating. This improvement in the polarization resistance till 24 h can possibly be attributed to the subsequent transformation of graphene wrapped vaterite spheres into the carbonated hydroxyapatite, as discussed in a following section.

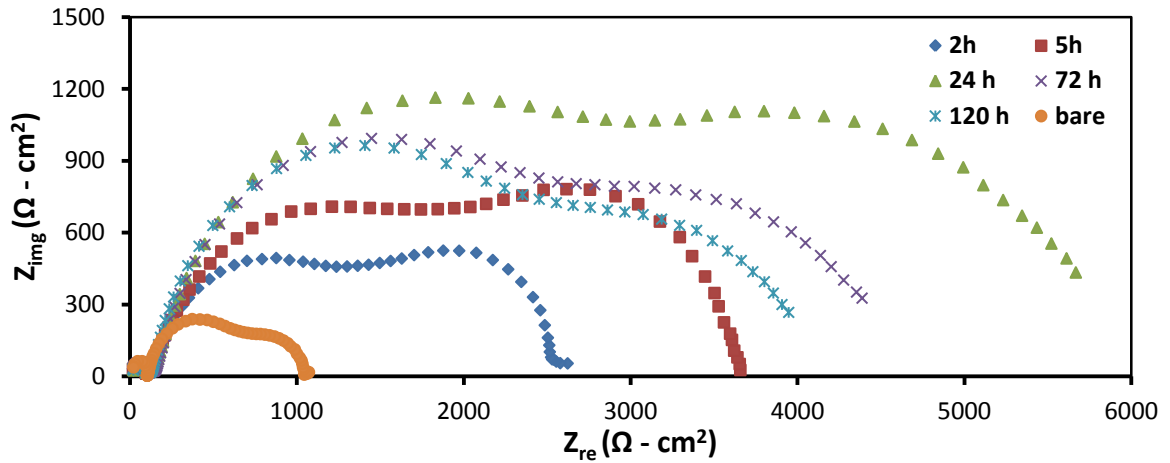


**Fig. 6.5.** Evolution of Nyquist plots for the graphene- $\text{CaCO}_3$  coated AZ91D in *m*-SBF for different durations

The impedance data of the bare AZ91D after 2 h of immersion and graphene- $\text{CaCO}_3$  coated alloy after different durations of prior immersion are also shown in Bode impedance plots (Figure 6.6a). In the Bode impedance plot, the magnitude of impedance at the lowest frequency represents the polarization or corrosion resistance. It is also noted from Bode impedance plots (Figure 6.6a) that the impedance of the graphene- $\text{CaCO}_3$  coated specimen at the lowest frequency is ~3 times higher than the bare AZ91D even after 120 h of immersion. The phase angle plots (Figure 6.6b) indicate two time constants for all the cases, one appearing at intermediate/higher frequency range (~10 - 100 Hz), while other at lower frequency (~ 0.1 - 1 Hz). The two time constants arising in case of the coated specimen may be attributed to the presence of two interfaces, i.e., the graphene- $\text{CaCO}_3$  coating/solution interface and the metal/solution interface. This is consistent with several other coated metal systems [221-225]. The presence of the two time constants in case of the bare alloy indicates the development of a film (presumably  $\text{Mg}(\text{OH})_2$ ) and thus two interfaces, i.e., the film consisting of corrosion products/solution interface and the metal/solution interface.

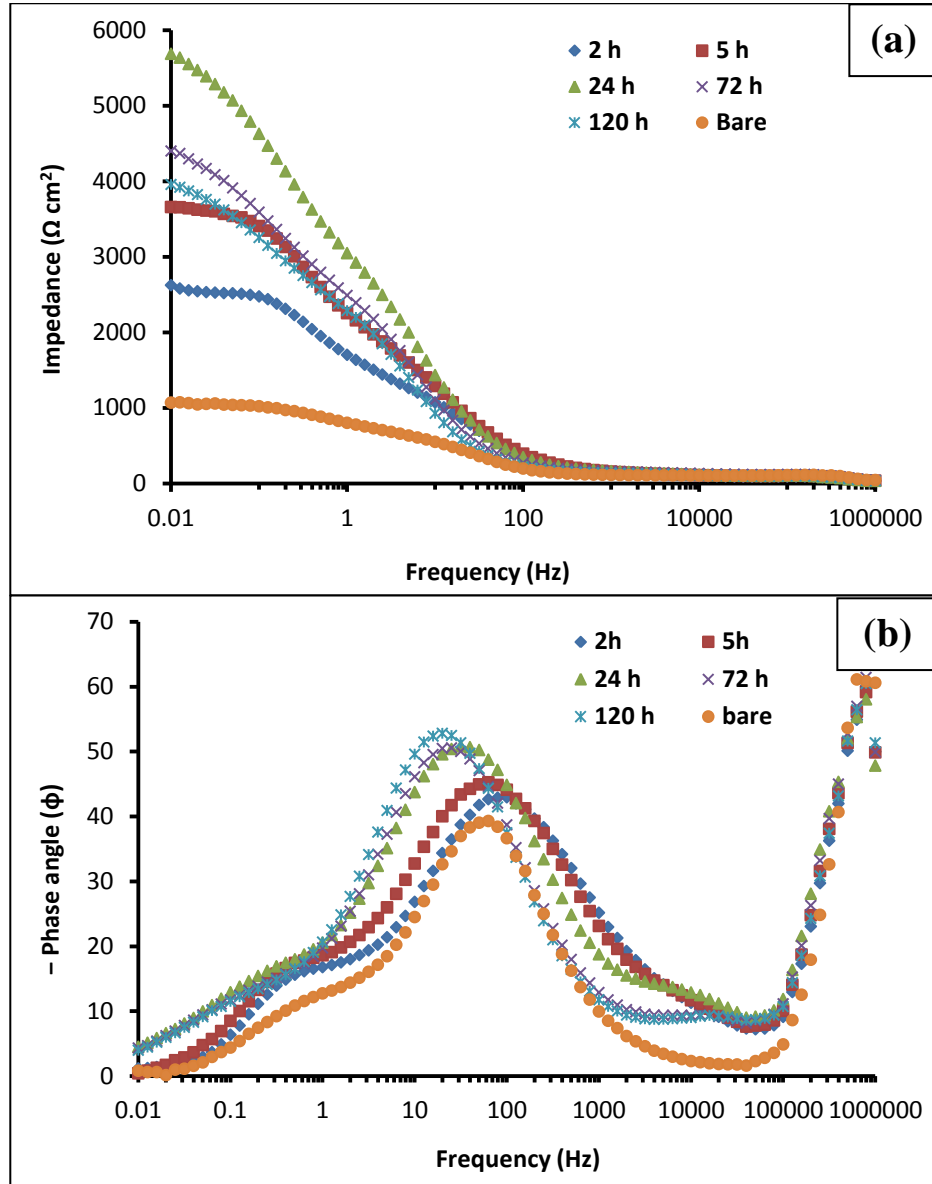


**Fig. 6.6.** (a) Bode impedance and (b) Bode phase plots for the graphene- $\text{CaCO}_3$  coated specimen after different immersion periods in *m*-SBF (immersion period was 2 h for bare AZ91D)

For quantitative determination of characteristic coating parameters such as capacitance, resistance etc., it is essential to simulate the experimental EIS data using an appropriate equivalent electrical circuit (EEC) based on a hypothetical corrosion mechanism. The following three main criteria should be fulfilled while choosing the EEC: (i) it should represent the hypothetical corrosion mechanism of the system, (ii) it should have low chi squared value, and (iii) it should have minimum total error and relative error in calculation of individual

parameters [188]. The EEC with two time constants, as shown in Figure 6.7, was used to simulate the experimental impedance data. The nested EEC was specifically chosen because of interconnected nature of the coating porosity, as is often reported in the case of the coated alloy systems [222, 223].

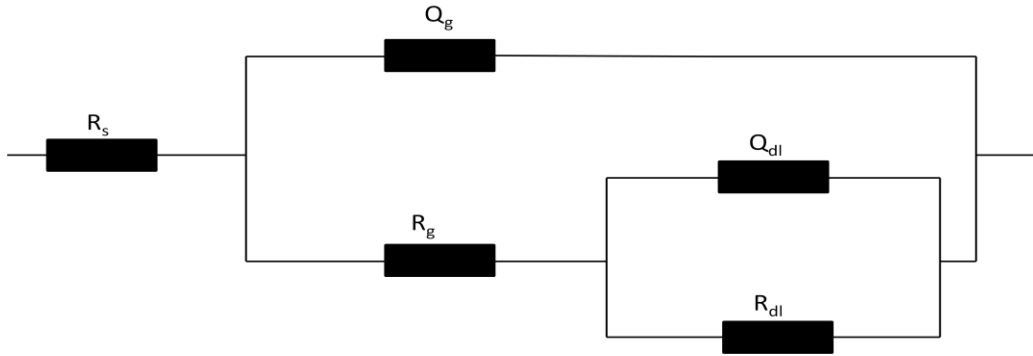


**Fig. 6.7.** The EEC used for simulation of experimental EIS data

In this EEC,  $R_s$  is the solution resistance and the surface film (graphene- $\text{CaCO}_3$  coating) is represented by a parallel combination of the constant phase element (CPE),  $Q_g$  and the film resistance,  $R_g$ . The electrical double layer is represented by another CPE,  $Q_{dl}$  and a charge transfer resistance,  $R_{dl}$ . In the simulation of experimental data, the CPE behaviour is generally attributed to the distributed surface reactivity, roughness, electrode porosity [188, 222]. Figures 6.8a and 6.8b show the fitting of simulated data with experimentally observed data for the graphene- $\text{CaCO}_3$  coated specimen after 2 h and 120 h of immersions, respectively. As evident from the Figures 6.8a and 6.8b, the experimental plots match well with the simulated data in the frequency region between 0.1 Hz and 100 kHz. The total error in impedance measurement in the simulation of the experimental data, when using the EEC shown in Fig. 6.7, was less than 7 % for all the experiments. The associated chi square values were also relatively low.

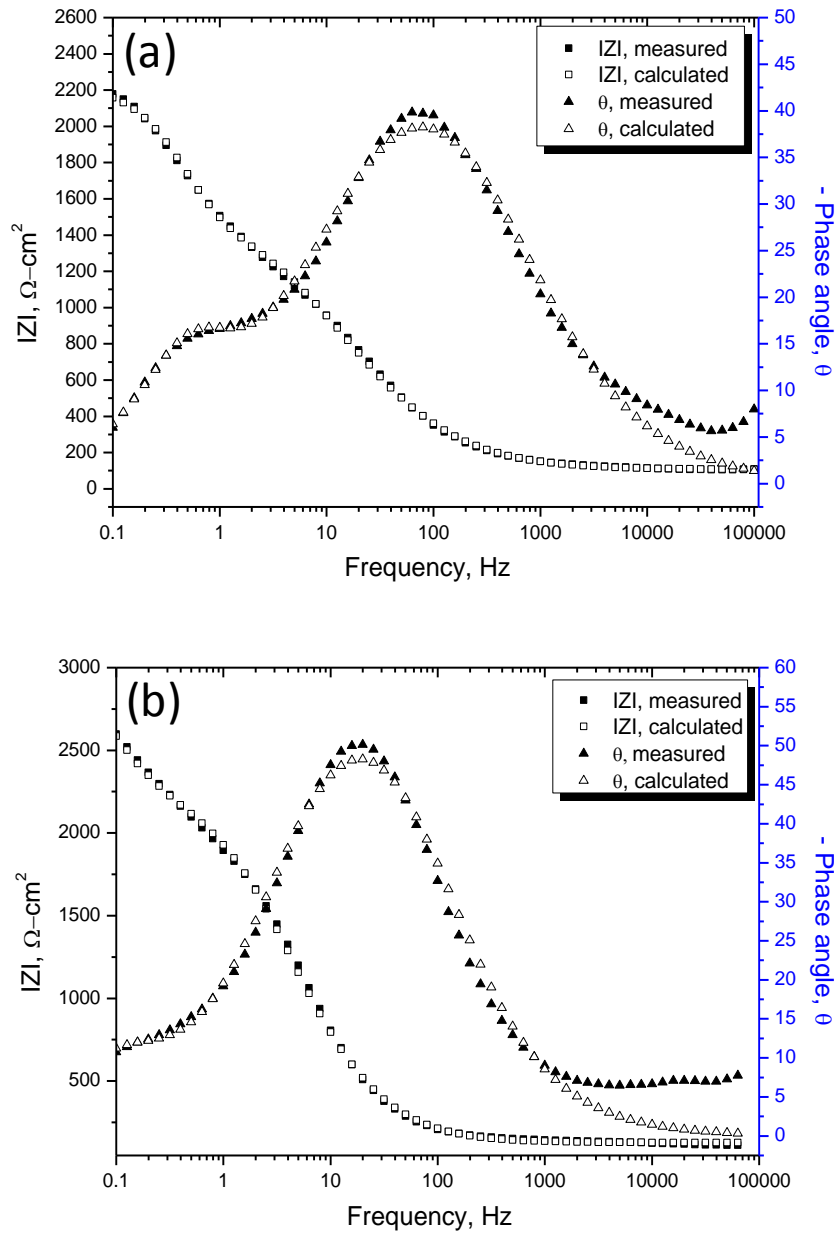


**Fig. 6.8.** Curve fitting of experimental and simulated Bode plots for the graphene-CaCO<sub>3</sub> coated specimen after: (a) 2 h of immersion and (b) 120 h of immersion in *m*-SBF

The temporal evolutions of the  $Q_g$ ,  $R_g$ ,  $Q_{dl}$  and  $R_{dl}$  for graphene-CaCO<sub>3</sub> coated specimen with different immersion time are shown in Fig. 6.9. The  $R_g$  values for graphene-CaCO<sub>3</sub> coated specimen increase with increasing immersion period till 24 h, but decrease slowly for the immersion between 24 h and 120 h, suggesting a gradual degradation of the coating after 24 h

(Fig. 6.9a). This behaviour is also complemented with simultaneous decrease in CPE,  $Q_g$ , till 24 h immersion, while an increase is observed between 24 h and 120 h immersion (Fig. 6.9b), suggesting the availability of more conductive pathways through coating for the electrolyte ingress at the coating/solution interface during 24 h - 120 h immersion in *m*-SBF. Similar behaviour was also observed in the case of  $R_{dl}$  and  $Q_{dl}$ .

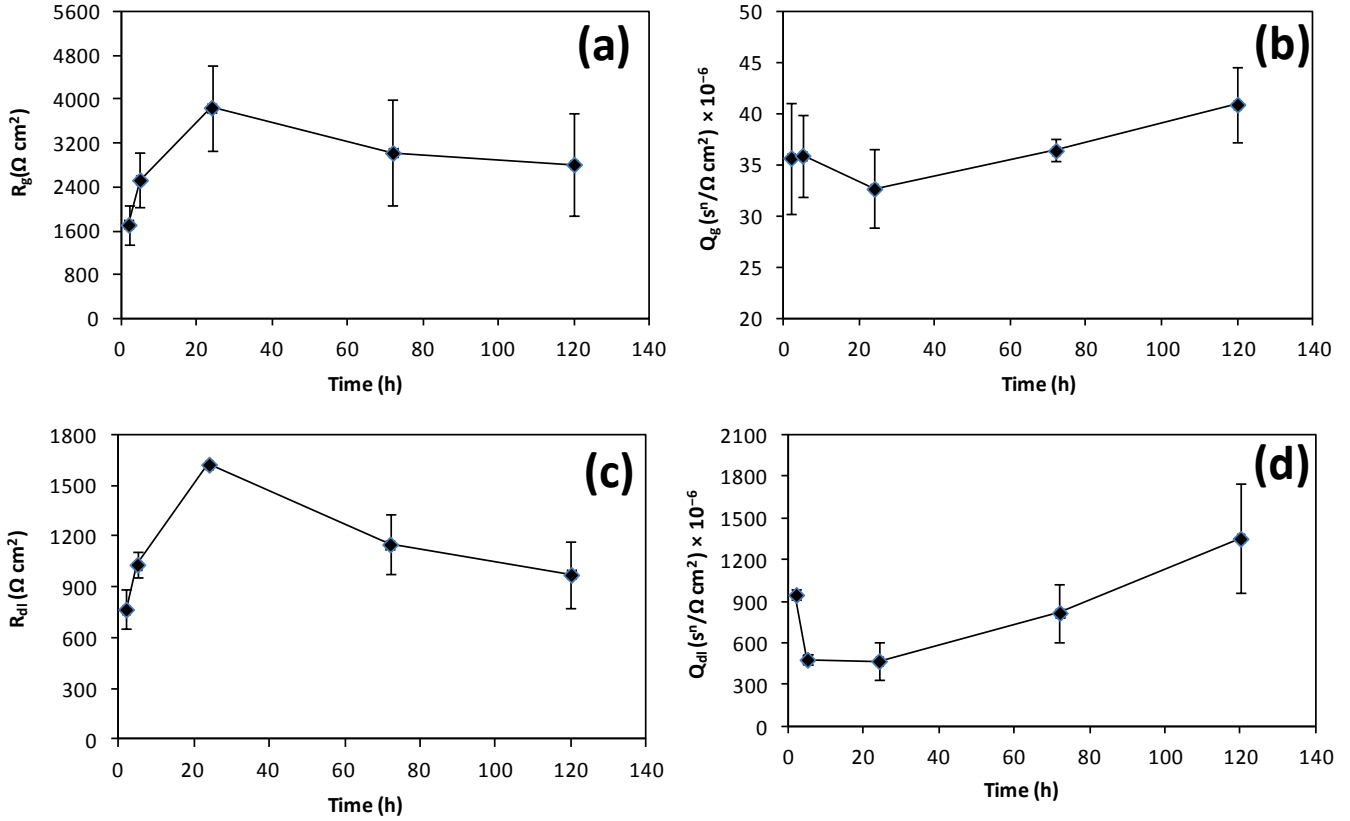


**Fig. 6.9.** Temporal evolution of different parameters for the graphene-CaCO<sub>3</sub> coated specimen after different immersion periods in *m*-SBF

In contrast, the only-CaCO<sub>3</sub> coating produced on AZ91D did not provide any appreciable improvement in polarization resistance (as shown in Nyquist and Bode impedance plots in the Fig. 6.10). In fact, the polarization resistance of the only-CaCO<sub>3</sub> coated specimen was even lower than that for the bare AZ91D (at all immersion periods in *m*-SBF).

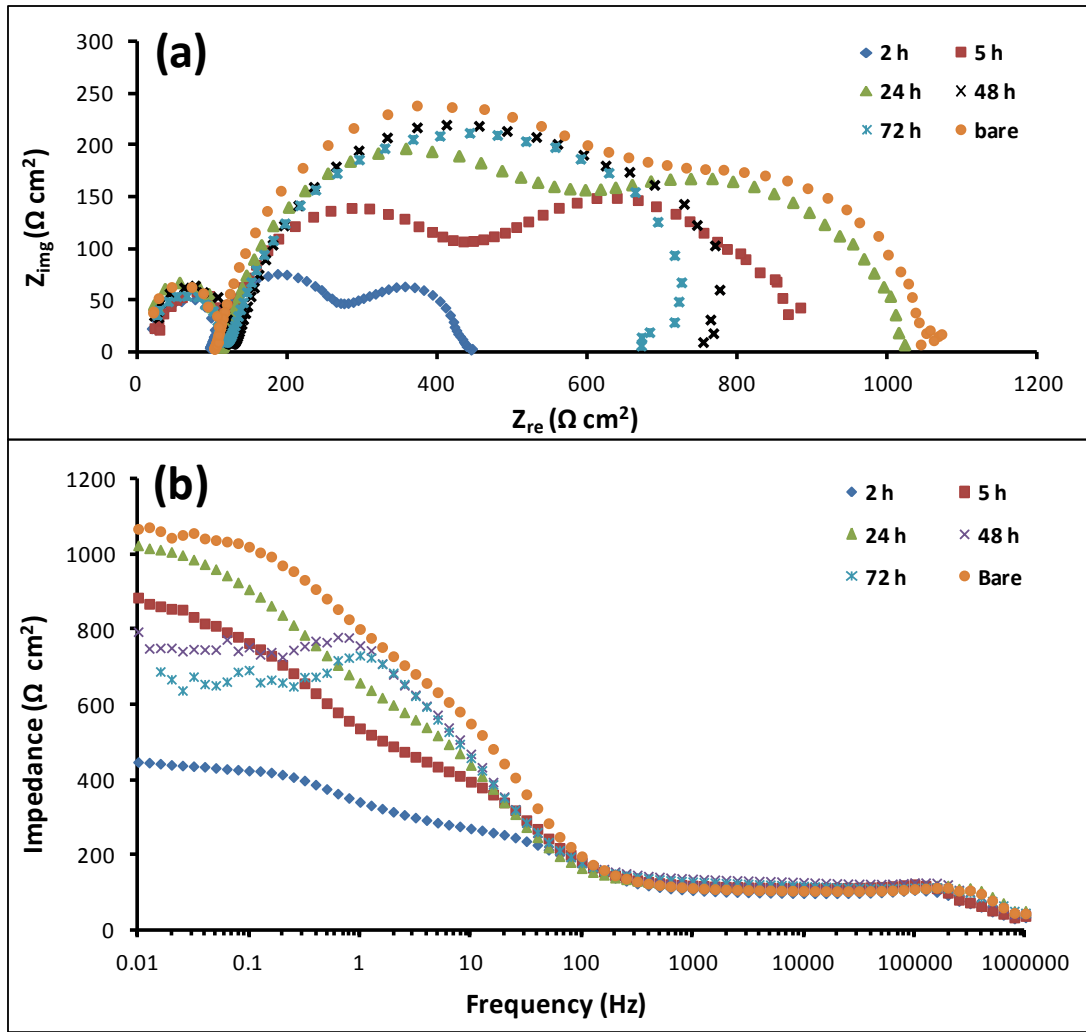


**Fig. 6.10.** Evolution of (a) Nyquist plots and (b) Bode impedance plots for the only-CaCO<sub>3</sub> coated AZ91D after different immersion periods in *m*-SBF at 37 °C

The potentiodynamic polarizations scans for bare AZ91D after 2 h of immersion and graphene-CaCO<sub>3</sub> coated specimens (after 2 h and 120 h of immersion in *m*-SBF) are shown in Fig. 6.11. The both cathodic and anodic current densities for graphene-CaCO<sub>3</sub> coated specimens are considerably lower as compared to the bare specimen for both 2 h and 120 h of immersions in *m*-SBF. A considerable decrease in cathodic current densities observed in case of the graphene-CaCO<sub>3</sub> coated specimen (for both 2 h and 120 h of immersion in *m*-SBF) suggests a reduced cathodic hydrogen evolution, which is one of the major concerns in using the magnesium alloys as implant materials [24, 76]. Moreover, the less hydrogen evolution during the initial period may allow implants to maintain their mechanical integrity in the

crucial initial bone healing phase. It is also noted that the corrosion potential for the graphene- $\text{CaCO}_3$  coated specimen after 120 h of immersion shifted considerably towards more noble direction (200 mV nobler than bare AZ91D), which could possibly be the result of formation of lath like hydroxyapatite after 120 h of immersion (discussed in Section 6.3.3). Potentiodynamic polarization results are in agreement with the EIS results shown in Nyquist and Bode plots (Fig. 6.5 and 6.6).

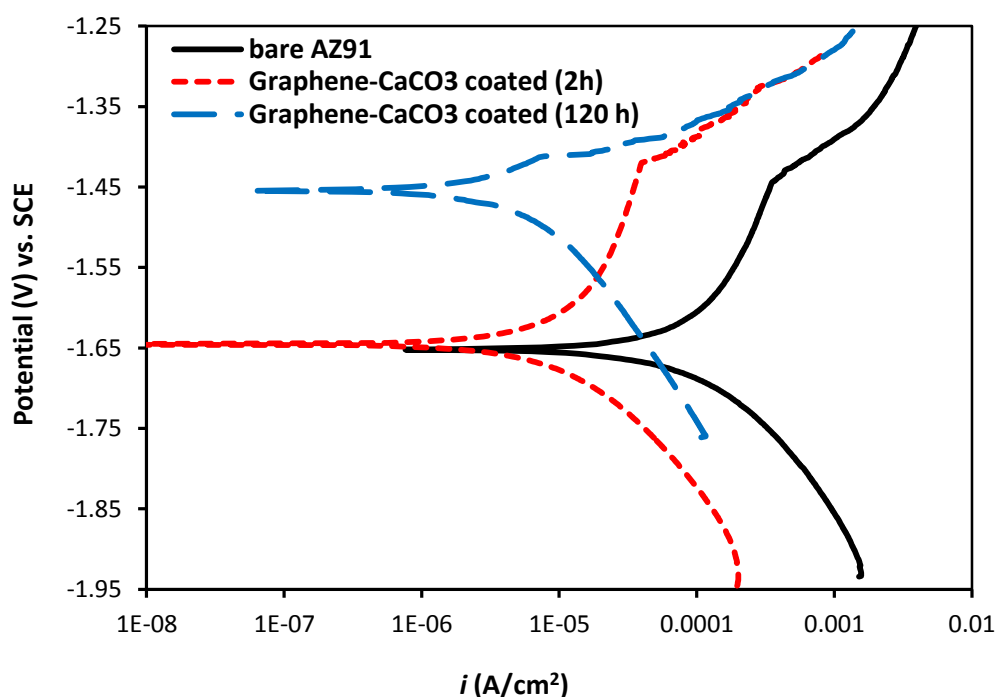


**Fig. 6.11.** Potentiodynamic polarization scans for the graphene- $\text{CaCO}_3$  coated and bare specimens tested in *m*-SBF at 37 °C

### 6.3.3 Post-corrosion morphologies

The macrographs of the coated specimens and bare alloy after a specific period of immersion are shown in Fig. 6.12. The surface of graphene- $\text{CaCO}_3$  coated specimen after 120 h of immersion in *m*-SBF appeared to be quite uniform and homogenous (Fig. 6.12a), whereas the only- $\text{CaCO}_3$  coated specimen showed a few localized corrosion attacks (arrows) after 72 h of immersion in *m*-SBF (Fig. 6.12b). Fig. 6.12c shows the corroded surface of bare AZ91D



specimen immersed in *m*-SBF for 120 h and revealed severe localized corrosion and pitting (indicated by an ellipse).

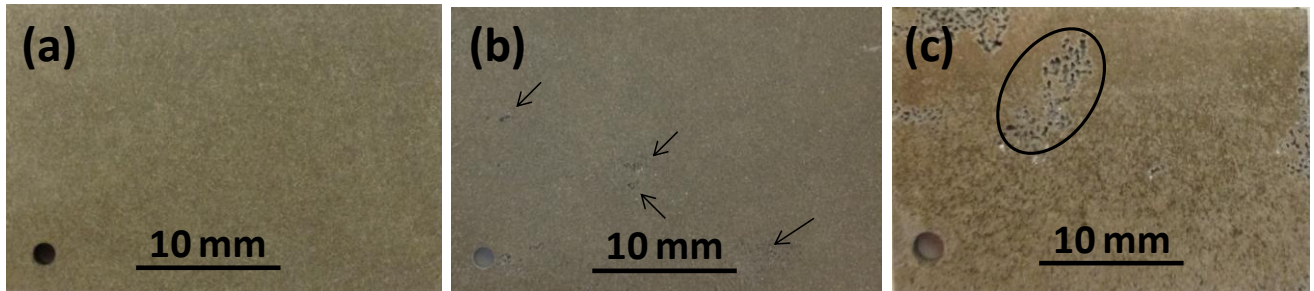


**Fig. 6.12.** Macrographs of: (a) graphene- $\text{CaCO}_3$  coated specimen after 120 h of immersion in *m*-SBF, (b) only- $\text{CaCO}_3$  coated specimen after 72 h of immersion in *m*-SBF, and (c) bare AZ91D after 120 h of immersion

The morphology of the graphene- $\text{CaCO}_3$  coated specimen immersed in *m*-SBF for 24 h revealed the transformation of vaterite microspheres (Fig. 6.2b) into needle shaped lath like structures (Fig. 6.13a). This lath like structure has been reported to be carbonated hydroxyapatite [178, 210, 211]. The higher polarization resistance achieved in case of graphene- $\text{CaCO}_3$  coated specimen during electrochemical testing after 24 h immersion in *m*-SBF could be attributed to this transformation of vaterite into carbonated hydroxyapatite. This morphology was maintained even after 120 h of immersion in *m*-SBF in the case of the graphene- $\text{CaCO}_3$  coated specimen (Fig. 6.13b). Furthermore, it is assumed that the in-vitro bone bioactivity with application of graphene- $\text{CaCO}_3$  coating will increase because of the transformation of graphene wrapped vaterite spheres into carbonated hydroxyapatite after exposure to the *m*-SBF. Since vaterite is highly soluble in aqueous solution ( $\log K_s = -7.91$ , at 25 °C) [209], it dissolves in the physiological environment according to the reaction:  $\text{CaCO}_3 = \text{Ca}^{2+} + \text{CO}_3^{2-}$ . The dissolution of vaterite is suggested to increase the concentration of  $\text{Ca}^{2+}$ , which combines with  $\text{PO}_4^{3-}$  available from the *m*-SBF, to nucleate hydroxyapatite on the sphere surface [210]. Carbonated hydroxyapatite is also reported to be highly biocompatible and similar to natural bone mineral [226]. Hence, the development of this coating on

magnesium alloys might be very promising in applications such as treatment of bone defects and bone degenerative diseases.

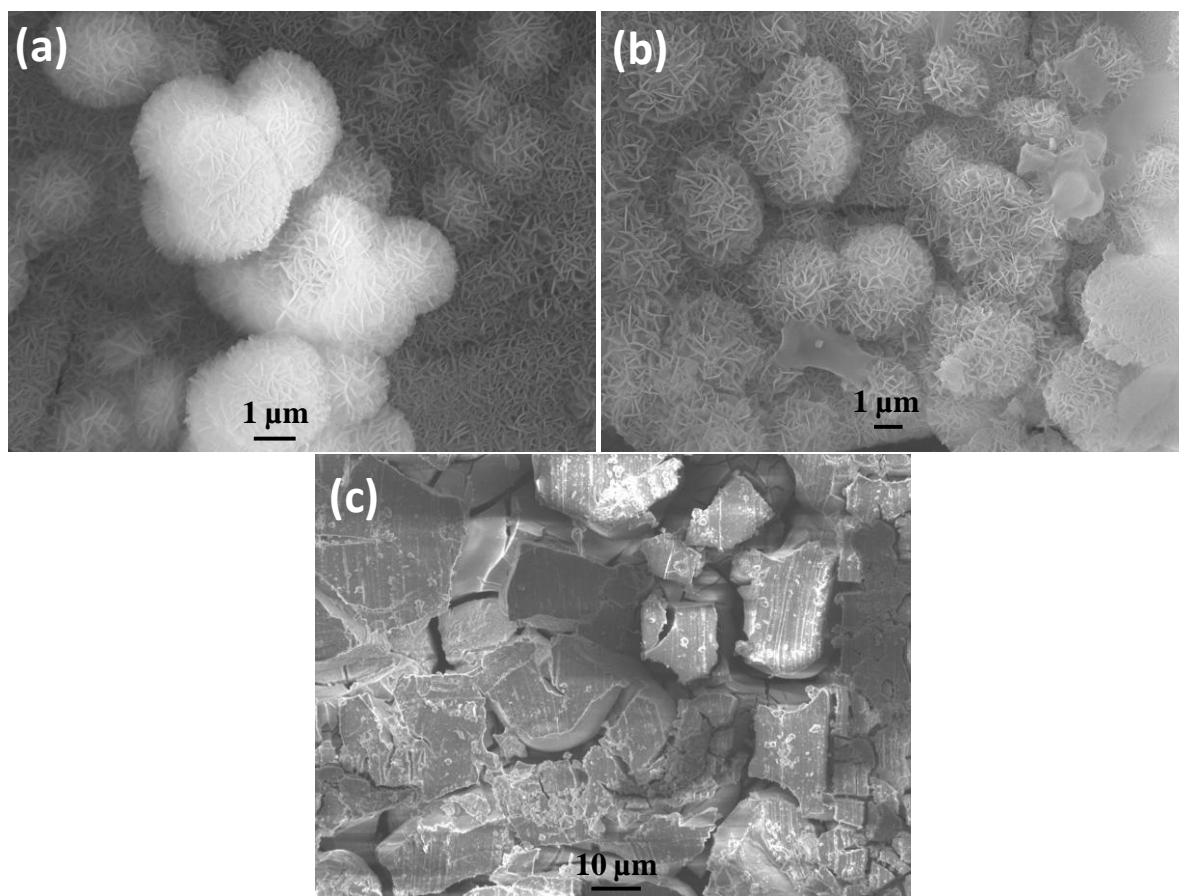


**Fig. 6.13.** Post-corrosion SEM morphology of: (a) graphene- $\text{CaCO}_3$  coated specimen after 24 h of immersion in *m*-SBF (b) graphene- $\text{CaCO}_3$  coated specimen after 120 h of immersion in *m*-SBF, and (c) only- $\text{CaCO}_3$  coated specimen after 72 h of immersion

In contrast, no apatite formation was observed in the only- $\text{CaCO}_3$  coating during incubation in *m*-SBF solution for 72 h (Fig. 6.13c), which could be attributed to the lower solubility and thermodynamic stability of rhombohedral calcite (the main component of only- $\text{CaCO}_3$  coating) that does not undergo any phase transformation in the physiological environment [209].

In order to have an appreciation for the long term corrosion protection provided by the graphene- $\text{CaCO}_3$  coating in *m*-SBF, the polarization resistances for the bare AZ91D, only- $\text{CaCO}_3$  and graphene- $\text{CaCO}_3$  coated specimens after different periods of immersion were

plotted in Fig. 6.14. At any given immersion time, the polarization resistance observed in the case of the graphene- $\text{CaCO}_3$  coated specimen was considerably higher than the other specimens (bare AZ91D and only- $\text{CaCO}_3$  coated specimen).

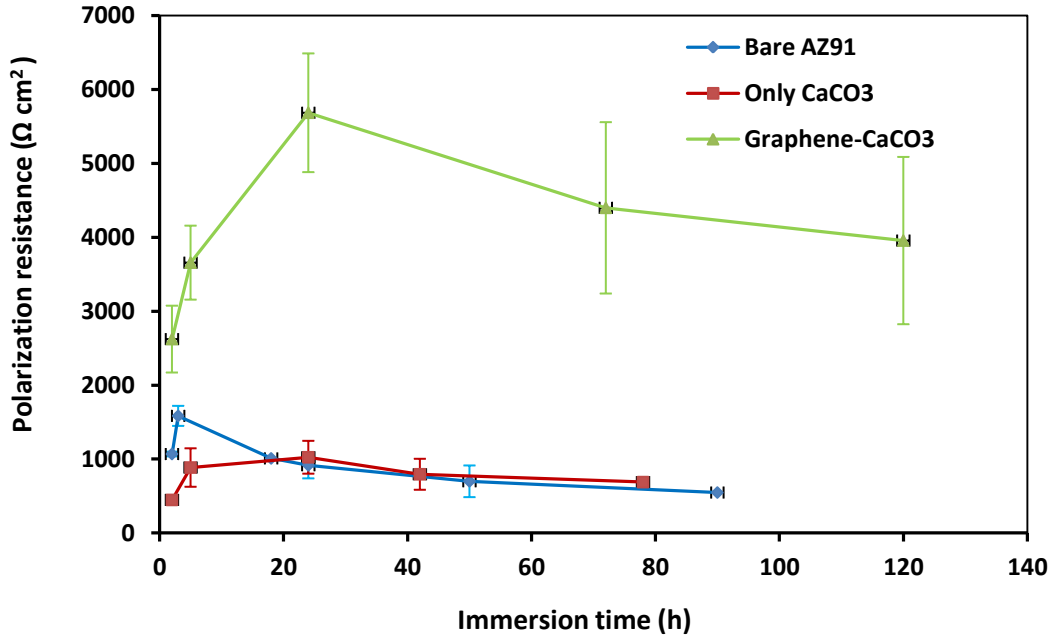


**Fig. 6.14.** Evolution of polarization resistance of graphene- $\text{CaCO}_3$  and only- $\text{CaCO}_3$  coated specimens in comparison to the bare AZ91D in *m*-SBF solution after different immersion durations

In general, the problem of localized corrosion/pitting is believed to be one of the major challenges in the use of magnesium alloys as biomaterials for construction of temporary implant devices [8]. Pitting is also known to initiate stress corrosion cracking in magnesium alloys [36]. However, as evident from Fig. 6.12 and 6.13, it is inferred that the application of graphene- $\text{CaCO}_3$  coating on AZ91D prevents the localized corrosion/pitting of the substrate after immersion in *m*-SBF solution, as a result of the formidable corrosion barrier effect of the coating (by inducing the carbonated apatite). The suppression of localized corrosion and pitting may also play a pivotal role in improving the mechanical integrity of the AZ91D in *m*-SBF solution.

#### 6.3.4 Mechanical integrity of the coating

As discussed in previous sections, the graphene-CaCO<sub>3</sub> coating not only induced the formation of phases that improve biocompatibility, such as carbonated hydroxyapatite during exposure to *m*-SBF, but also provided long term corrosion protection and suppressed localized pitting. Less probability of localized pitting due to application of this coating and presence of graphene network in the coating may also enhance mechanical integrity/SCC resistance of the AZ91D in load bearing conditions. In the present study, the mechanical integrity of the coating was evaluated by first immersing the coated tensile specimens in *m*-SBF for 120 h, followed by straining in the air at  $3.1 \times 10^{-7} \text{ s}^{-1}$ . As a control, two other experiments were also performed: (i) bare AZ91D was directly pulled in air and (ii) bare AZ91D was pre-immersed in *m*-SBF for 120 h followed by straining in air at the strain rate of  $3.1 \times 10^{-7} \text{ s}^{-1}$ .

The macrographs of the gauge lengths of the tensile specimens of graphene-CaCO<sub>3</sub> coated and uncoated alloy before and after the immersion in *m*-SBF are shown in Fig. 6.15. The uncoated sample after 120 h of immersion in *m*-SBF revealed significant localized corrosion attack and severe pitting, as identified within an ellipse in Fig. 6.15b. In contrast, the graphene-CaCO<sub>3</sub> coated specimens showed a homogenous/uniform degradation over the entire gauge length (Fig. 6.15d). These pre-immersion results also corroborated the electrochemical testing results as discussed in Section 6.3.2.

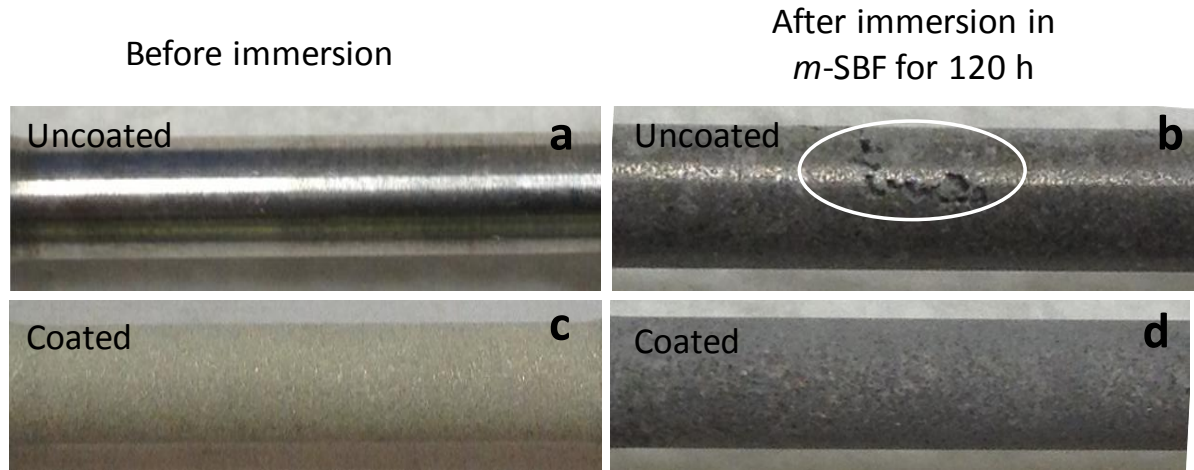


**Fig. 6.15.** Macrographs of the gauge length of the coated and uncoated tensile specimens before and after immersion in *m*-SBF solution

The UTS values of the graphene-CaCO<sub>3</sub> coated and uncoated samples pulled in air at strain rate of  $3.1 \times 10^{-7} \text{ s}^{-1}$  (after pre-immersion in *m*-SBF) are represented in Fig. 6.16. For comparison, the UTS of the uncoated specimen without pre-exposure was also determined. The unexposed specimens tested in air exhibited an average UTS value of 162 MPa. The coated specimens had an average UTS value of 126 MPa after pre-immersion, whereas the uncoated specimens after pre-immersion exhibited an average UTS of only 96 MPa. On the basis of the UTS data, the uncoated specimens after pre-immersion in *m*-SBF could only retain 58 % of the mechanical strength of the uncoated, unexposed alloy, whereas the graphene-CaCO<sub>3</sub> coated alloy retained ~18 % higher strength.

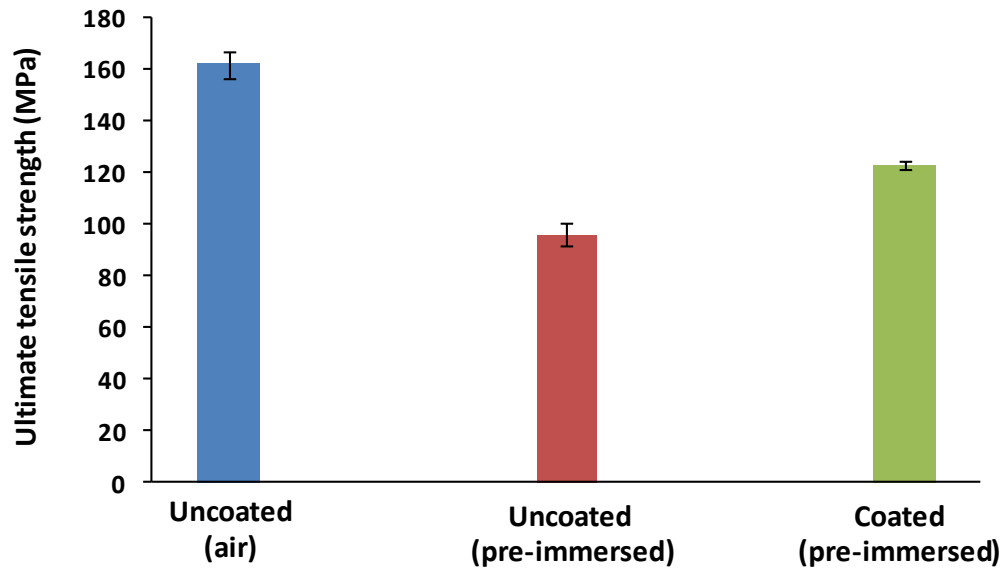


**Fig. 6.16.** Ultimate tensile strengths for the uncoated specimen pulled in air, pre-immersed uncoated specimen pulled in air, pre-immersed coated specimen pulled in air

As reported in Sections 2.5 and 2.6 of Chapter 2, localized corrosion, especially pitting, strongly influences the mechanical integrity of Mg alloys since the pits can act as stress risers and expose bare, film-free and active Mg surface [35, 36]. Moreover, as shown in Fig. 6.15b, Mg and its alloys undergo pitting corrosion in the physiological environment that has considerable chloride content [16, 72]. Localized Mg dissolution not only enhances the chances of anodic dissolution-assisted stress corrosion cracking but also paves the way for hydrogen to enter into the metal causing hydrogen embrittlement, as established in Chapter 4 and 5 as well as in the literature [36]. Nevertheless, graphene- $\text{CaCO}_3$  coating significantly reduced the susceptibility of the alloy towards localized corrosion/pitting (Fig. 6.12). Hence, the use of the biocompatible coating of graphene- $\text{CaCO}_3$  can considerably decrease the localized corrosion/pitting susceptibility of a Mg alloy and thereby decrease the probability of hydrogen entry into the matrix. Thus, the graphene- $\text{CaCO}_3$  coating can improve the resistance to SCC of Mg alloys in the physiological environment.

In summary, the results of this study suggest the use of graphene-CaCO<sub>3</sub> coating on AZ91D to be very promising in biomedical applications. This coating has potential not only for providing the long term corrosion protection in the physiological environment but also for improving the in-vitro bone biocompatibility by inducing the formation of bone apatite. Moreover, as discussed, the presence of strong graphene network and the suppression of localized corrosion may lead to the improved mechanical integrity/SCC behaviour in load bearing implant applications.

## 6.4 Conclusions

The application of graphene-CaCO<sub>3</sub> coating on AZ91D provided three-fold advantages of long term corrosion resistance, excellent biocompatibility and improved mechanical integrity as discussed below:

- The graphene-CaCO<sub>3</sub> coating was successfully synthesized on AZ91D using an economical conversion route at room temperature.
- The presence of dispersed graphene network facilitated the formation of thermodynamically unstable form of calcium carbonates, i.e. vaterite on the AZ91D surface.
- Electrochemical results indicated that the graphene-CaCO<sub>3</sub> coating acted as a corrosion barrier for AZ91D and provided a durable corrosion protection in *m*-SBF. The graphene-CaCO<sub>3</sub> coated specimens showed ~3 times higher corrosion resistance as compared to bare specimen even after 120 h of immersion in *m*-SBF.
- Post corrosion morphology revealed the transformation of graphene wrapped vaterite microspheres into the carbonated apatite after incubation in *m*-SBF, thus leading to an improved bone bioactivity of the graphene-CaCO<sub>3</sub> coated AZ91D.

- It was also observed that the application of graphene-CaCO<sub>3</sub> coating prevented localized corrosion/pitting of AZ91D in physiological environment.
- Mechanical integrity of the coated specimen was improved by ~18 %, mainly as a result of the suppression of localized corrosion/pitting of AZ91D due to application of the coating.





## Chapter 7

### 7. Overall conclusions and future work

#### 7.1 Overall conclusions

The major outcomes of this thesis are presented below:

- Magnesium alloys were found to be susceptible to SCC in the physiological environment of *m*-SBF. The significant reduction in mechanical integrity was observed in both AZ91D and Mg3Zn1Ca alloys when tested in *m*-SBF as compared to air. The SCC susceptibility increased with decreasing strain rate. The predominant mode for SCC crack propagation in both the alloys was transgranular cracking. The SSRT experiments under different environmental conditions suggested the SCC mechanism to be the combined effect of hydrogen assisted stress corrosion cracking (HASCC) and anodic dissolution. The Mg3Zn1Ca alloy was found to be more susceptible to the SCC at a given strain rate as compared to the AZ91D alloy, which was attributed to a greater propensity of the Mg3Zn1Ca alloy to generate cathodic hydrogen.
- The important design parameter for quantitative characterization of SCC (i.e.  $K_{ISCC}$ ) was determined for the AZ91D alloy in the physiological environment using circumferential notch tensile (CNT) testing. The threshold stress intensity for stress corrosion cracking ( $K_{ISCC}$ ) for AZ91D in *m*-SBF at 37 °C was determined to be 5.18 MPa m<sup>1/2</sup>. The crack growth rates were observed in the range of 10<sup>-9</sup> - 10<sup>-10</sup> m/s, and found to be increasing with the applied stress intensity. Common mode for SCC crack propagation in AZ91D during CNT testing was transgranular cracking, which was consistent with the literature on SCC of Mg alloys in chloride environments. As demonstrated in this study, it will be possible to calculate the life of implants of

magnesium alloys using the stress intensity-crack growth relation. The flaw-tolerant design assessment, such as by the CNT testing of the implant devices (that may have a pre-existing fine crack), will provide a crucial information on whether the existing crack will be tolerable for the given service time of the device.

- Recently developed novel biocompatible and biodegradable Al-free extruded Mg alloys, WZ21, ZX50 and WE43, were evaluated for their resistance to SCC in *m*-SBF using SSRT testing. All the alloys revealed excellent mechanical properties when tested in air, which was attributed to the fine grain size of the alloys. In contrast, each alloy suffered significant embrittlement when tested in *m*-SBF, as suggested by a considerably lower elongation-to-failure observed in *m*-SBF as compared to the air. The ZX50 alloy suffered greater SCC as compared to the WZ21 and WE43, which was attributed to its higher propensity towards localized corrosion/pitting in *m*-SBF. The SCC mechanism for these extruded alloys was the combined effect of HASCC and anodic dissolution, as was also reported for AZ91D and Mg<sub>3</sub>Zn<sub>1</sub>Ca. The major contribution of SCC in WE43 alloy was from HASCC due to higher magnitude of cathodic current density (i.e. greater cathodic hydrogen generation), while the major contribution of SCC in WZ21 alloy was due to anodic dissolution.
- A novel biocompatible graphene-CaCO<sub>3</sub> coating was successfully developed on AZ91D using an economical conversion route. The coating not only provided the long term corrosion protection (e.g. polarization resistance for the coated specimen was ~3 times higher than the uncoated specimen even after 120 h of immersion in *m*-SBF) but also generated the chemical features that are known to improve biocompatibility, i.e. formation of the carbonated apatite after incubation in *m*-SBF. The graphene-CaCO<sub>3</sub> coating also played an important role in reducing the localized corrosion and pitting of AZ91D in *m*-SBF, thus improving the mechanical integrity of the alloy.

## 7.2 Future work

There are many aspects of the evaluation of mechanical integrity and/or environmentally-assisted cracking of biomedical magnesium alloys, which were beyond the scope of this study, but are important to examine in order to obtain a more comprehensive understanding. Some of these are listed below:

- The premature failures of metallic biomaterials are frequently associated with the cyclic stresses that are often experienced by implant devices (e.g. cardiovascular stents). The synergistic presence of cyclic stresses and corrosive physiological environment can cause corrosion fatigue. The characterization of corrosion fatigue of such potential biodegradable Mg alloys would be of major importance before their actual use.
- There have been only a few studies on the phenomenological modelling for correlation of SCC and crack growth rate and various environmental, electrochemical and mechanical parameters for Mg alloys. In fact, the phenomenological understanding of hydrogen-assisted stress corrosion cracking based on hydrogen diffusivity and permeability data on the alloy surface and the hydrogen distribution around the crack tip will be necessary for a more complete understanding of SCC of Mg alloys.
- In addition to the crack growth rate determination (as conducted by CNT testing in the present study), SCC crack initiation studies could be performed with the help of other analytical techniques (such as direct current potential drop (DCPD)) in combination with CNT testing. CNT testing could also be performed on other biocompatible Mg alloys, i.e. WZ21 and ZX50.
- All the testing in this study was performed in the *m*-SBF, which contains only the inorganic portion of the blood plasma. However, it would be essential to evaluate the

influence of organic components such as glucose/proteins on corrosion behaviour of the alloys, and thus possibly the effect of such organic compounds on the SCC of the alloy. A systematic analysis of ion release into the physiological system during the corrosion process under stressed conditions could also be investigated.

- The application of graphene-CaCO<sub>3</sub> coating on the potential Al-free biodegradable magnesium alloys have not been investigated in this study. In addition, the cell culture and cytotoxicity analysis were also beyond the scope of the present study. A thorough characterisation of the graphene-CaCO<sub>3</sub> coating using X-ray photoelectron spectroscopy (XPS) may provide a deep mechanistic understanding of the corrosion processes of the coated alloy.

## 8. Bibliography

- [1] Staiger MP, Pietak AM, Huadmai J, Dias G. Magnesium and its alloys as orthopedic biomaterials: A review. *Biomaterials* 2006;27:1728-34.
- [2] Puleo DA, Huh WW. Acute toxicity of metal ions in cultures of osteogenic cells derived from bone marrow stromal cells. *J Appl Biomater* 1995;6:109-16.
- [3] Jacobs JJ, Hallab NJ, Skipor AK, Urban RM. Metal Degradation Products: A Cause for Concern in Metal-Metal Bearings? *Clinical Orthopaedics and Related Research* 2003;139-47.
- [4] Wang JY, Wicklund BH, Gustilo RB, Tsukayama DT. Titanium, chromium and cobalt ions modulate the release of bone-associated cytokines by human monocytes/macrophages in vitro. *Biomaterials* 1996;17:2233-40.
- [5] Witte F, Hort N, Vogt C, Cohen S, Kainer KU, Willumeit R, Feyerabend F. Degradable biomaterials based on magnesium corrosion. *Curr Opin Solid State Mater Sci* 2009;12:63-72.
- [6] Makar GL, Kruger J. Corrosion of magnesium. *Int Mater Rev* 1993;38:138-53.
- [7] Witte F. The history of biodegradable magnesium implants: A review. *Acta Biomaterialia* 2011;6:1680-92.
- [8] Xin Y, Hu T, Chu PK. In vitro studies of biomedical magnesium alloys in a simulated physiological environment: A review. *Acta Biomaterialia* 2011;7:1452-9.
- [9] Wolf FI, Cittadini A. Chemistry and biochemistry of magnesium. *Molecular Aspects of Medicine* 2003;24:3-9.
- [10] Saris N-EL, Mervaala E, Karppanen H, Khawaja JA, Lewenstam A. Magnesium: An update on physiological, clinical and analytical aspects. *Clin Chim Acta* 2000;294:1-26.
- [11] Hartwig A. Role of magnesium in genomic stability. *Mutation Research/Fundamental and Molecular Mechanisms of Mutagenesis* 2001;475:113-21.
- [12] Song G. Control of biodegradation of biocompatible magnesium alloys. *Corros Sci* 2007;49:1696-701.
- [13] Kirkland NT, Lespagnol J, Birbilis N, Staiger MP. A survey of bio-corrosion rates of magnesium alloys. *Corros Sci* 2010;52:287-91.
- [14] Heublein B, Rohde R, Kaese V, Niemeyer M, Hartung W, Haverich A. Biocorrosion of magnesium alloys: a new principle in cardiovascular implant technology? *Heart* 2003;89:651-6.
- [15] Kirkland N, Staiger M, Nisbet D, Davies C, Birbilis N. Performance-driven design of Biocompatible Mg alloys. *JOM Journal of the Minerals, Metals and Materials Society* 2011;63:28-34.
- [16] Kannan MB, Raman RKS. In vitro degradation and mechanical integrity of calcium-containing magnesium alloys in modified-simulated body fluid. *Biomaterials* 2008;29:2306-14.
- [17] Xin Y, Huo K, Tao H, Tang G, Chu PK. Influence of aggressive ions on the degradation behavior of biomedical magnesium alloy in physiological environment. *Acta Biomaterialia* 2008;4:2008-15.

- [18] Bobby Kannan M, Dietzel W, Blawert C, Atrens A, Lyon P. Stress corrosion cracking of rare-earth containing magnesium alloys ZE41, QE22 and Elektron 21 (EV31A) compared with AZ80. *Mater Sci Eng, A* 2008;480:529-39.
- [19] Ben-Hamu G, Eliezer D, Dietzel W, Shin KS. Stress corrosion cracking of new Mg-Zn-Mn wrought alloys containing Si. *Corros Sci* 2008;50:1505-17.
- [20] Bombara G, Cavallini M. Stress corrosion cracking of bone implants. *Corros Sci* 1977;17:77-85.
- [21] Sivakumar M, Rajeswari S. Investigation of failures in stainless steel orthopaedic implant devices: pit-induced stress corrosion cracking. *J Mater Sci Lett* 1992;11:1039-42.
- [22] Shadanbaz S, Dias GJ. Calcium phosphate coatings on magnesium alloys for biomedical applications: A review. *Acta Biomaterialia* 2012;8:20-30.
- [23] Wong HM, Yeung KWK, Lam KO, Tam V, Chu PK, Luk KDK, Cheung KMC. A biodegradable polymer-based coating to control the performance of magnesium alloy orthopaedic implants. *Biomaterials* 2010;31:2084-96.
- [24] Zberg B, Uggowitzer PJ, Löffler JF. MgZnCa glasses without clinically observable hydrogen evolution for biodegradable implants. *Nat Mater* 2009;8:887-91.
- [25] Song YW, Shan DY, Han EH. Electrodeposition of hydroxyapatite coating on AZ91D magnesium alloy for biomaterial application. *Mater Lett* 2008;62:3276-9.
- [26] Gu XN, Zhou WR, Zheng YF, Cheng Y, Wei SC, Zhong SP, Xi TF, Chen LJ. Corrosion fatigue behaviors of two biomedical Mg alloys - AZ91D and WE43 - In simulated body fluid. *Acta Biomaterialia* 2010;6:4605-13.
- [27] Bobby Kannan M, Singh Raman RK, Witte F, Blawert C, Dietzel W. Influence of circumferential notch and fatigue crack on the mechanical integrity of biodegradable magnesium-based alloy in simulated body fluid. *Journal of Biomedical Materials Research Part B: Applied Biomaterials* 2011;96B:303-9.
- [28] Gupta VB, Anitha S, Hegde ML, Zecca L, Garruto RM, Ravid R, Shankar SK, Stein R, Shanmugavelu P, Jagannatha Rao KS. Aluminium in Alzheimer's disease: are we still at a crossroad? *Cellular and Molecular Life Sciences* 2005;62:143-58.
- [29] Zhang S, Zhang X, Zhao C, Li J, Song Y, Xie C, Tao H, Zhang Y, He Y, Jiang Y, Bian Y. Research on an Mg-Zn alloy as a degradable biomaterial. *Acta Biomaterialia* 2010;6:626-40.
- [30] Li Z, Gu X, Lou S, Zheng Y. The development of binary Mg-Ca alloys for use as biodegradable materials within bone. *Biomaterials* 2008;29:1329-44.
- [31] Wang HX, Guan SK, Wang X, Ren CX, Wang LG. In vitro degradation and mechanical integrity of Mg-Zn-Ca alloy coated with Ca-deficient hydroxyapatite by the pulse electrodeposition process. *Acta Biomaterialia* 2010;6:1743-8.
- [32] Hänzi AC, Gerber I, Schinhammer M, Löffler JF, Uggowitzer PJ. On the in vitro and in vivo degradation performance and biological response of new biodegradable Mg-Y-Zn alloys. *Acta Biomaterialia* 2010;6:1824-33.
- [33] Kraus T, Fischerauer SF, Hänzi AC, Uggowitzer PJ, Löffler JF, Weinberg AM. Magnesium alloys for temporary implants in osteosynthesis: In vivo studies of their degradation and interaction with bone. *Acta Biomaterialia* 2012;8:1230-8.
- [34] Celarek A, Kraus T, Tschegg EK, Fischerauer SF, Stanzl-Tschegg S, Uggowitzer PJ, Weinberg AM. PHB, crystalline and amorphous magnesium alloys: Promising candidates for bioresorbable osteosynthesis implants? *Mater Sci Eng, C* 2012;32:1503-10.

- [35] Winzer N, Atrens A, Song G, Ghali E, Dietzel W, Kainer K, Hort N, Blawert C. A Critical Review of the Stress Corrosion Cracking (SCC) of Magnesium Alloys. *Adv Eng Mater* 2005;7:659-93.
- [36] Stampella RS, Procter RPM, Ashworth V. Environmentally-induced cracking of magnesium. *Corros Sci* 1984;24:325-41.
- [37] Niinomi M. Recent metallic materials for biomedical applications. *Metall Trans A* 2002;33:477-86.
- [38] Ratner BD, Hoffman AS, Schoen FJ, Lemons JE. *Biomaterials Science: An Introduction to Materials in Medicine*: Elsevier Science; 1996.
- [39] Williams DF. Corrosion of implant materials. *Annu Rev Mater Sci* 1976;6:237-66.
- [40] Grimm MJ. Selection of Materials for Biomedical Applications. *Handbook of Materials Selection*: John Wiley & Sons, Inc.; 2007. p. 1165-94.
- [41] Nielsen K. Corrosion of metallic implants. *Br Corros J* 1987;22:272-8.
- [42] Niinomi M. Metallic biomaterials. *Journal of Artificial Organs* 2008;11:105-10.
- [43] Joon B. Park YKK. *Biomaterials: Principles and Applications*. Boca Raton: CRC Press LLC; 2002.
- [44] Black J. *Orthopaedic biomaterials in research and practice*: Churchill Livingstone; 1988.
- [45] Lhotka C, Szekeres T, Steffan I, Zhuber K, Zweymuller K. Four-year study of cobalt and chromium blood levels in patients managed with two different metal-on-metal total hip replacements. *Journal of Orthopaedic Research* 2003;21:189-95.
- [46] Granchi D, Ciapetti G, Stea S, Savarino L, Filippini F, Sudanese A, Zinghi G, Montanaro L. Cytokine release in mononuclear cells of patients with Co-Cr hip prosthesis. *Biomaterials* 1999;20:1079-86.
- [47] Niki Y, Matsumoto H, Suda Y, Otani T, Fujikawa K, Toyama Y, Hisamori N, Nozue A. Metal ions induce bone-resorbing cytokine production through the redox pathway in synoviocytes and bone marrow macrophages. *Biomaterials* 2003;24:1447-57.
- [48] Wang ML, Nesti LJ, Tuli R, Lazatin J, Danielson KG, Sharkey PF, Tuan RS. Titanium particles suppress expression of osteoblastic phenotype in human mesenchymal stem cells. *Journal of Orthopaedic Research* 2002;20:1175-84.
- [49] Erne P, Schier M, Resink T. The Road to Bioabsorbable Stents: Reaching Clinical Reality? *CardioVascular and Interventional Radiology* 2006;29:11-6.
- [50] Zeng R, Dietzel W, Witte F, Hort N, Blawert C. Progress and Challenge for Magnesium Alloys as Biomaterials. *Adv Eng Mater* 2008;10:B3-B14.
- [51] Paital SR, Dahotre NB. Calcium phosphate coatings for bio-implant applications: Materials, performance factors, and methodologies. *Materials Science and Engineering: R: Reports* 2009;66:1-70.
- [52] Bobyn JD, Mortimer ES, Glassman AH, Engh CA, Miller JE, Brooks CE. Producing and avoiding stress shielding. Laboratory and clinical observations of noncemented total hip arthroplasty. *Clinical orthopaedics and related research* 1992:79-96.
- [53] Lucas G, Cooke F, Friis E. Stress Shielding of Bone. *A Primer of Biomechanics*: Springer New York; 1999. p. 79-88.
- [54] Song GL. *Corrosion of Magnesium Alloys*: Woodhead Pub Limited; 2011.



- [55] Bostman O. Osteolytic changes accompanying degradation of absorbable fracture fixation implants. *Journal of Bone & Joint Surgery, British Volume* 1991;73-B:679-82.
- [56] Cheung H-Y, Lau K-T, Lu T-P, Hui D. A critical review on polymer-based bio-engineered materials for scaffold development. *Composites Part B: Engineering* 2007;38:291-300.
- [57] Polmear IJ. *Light Alloys: Metallurgy of the Light Metals*: Edward Arnold; 1997.
- [58] Friedrich HE, Mordike BL. *Magnesium Technology: Metallurgy, Design Data, Applications*: Physica-Verlag; 2006.
- [59] Witte F, Kaese V, Haferkamp H, Switzer E, Meyer-Lindenberg A, Wirth CJ, Windhagen H. In vivo corrosion of four magnesium alloys and the associated bone response. *Biomaterials* 2005;26:3557-63.
- [60] McBride ED. Absorbable metal in bone surgery: A further report on the use of magnesium alloys. *Journal of the American Medical Association* 1938;111:2464-7.
- [61] Witte F, Fischer J, Nellesen J, Crostack H-A, Kaese V, Pisch A, Beckmann F, Windhagen H. In vitro and in vivo corrosion measurements of magnesium alloys. *Biomaterials* 2006;27:1013-8.
- [62] Bernhardt NE, Kasko AM. *Nutrition for Middle Aged and Elderly*: Nova Biomedical Books; 2008.
- [63] Vormann Jr. Magnesium: nutrition and metabolism. *Molecular Aspects of Medicine* 2003;24:27-37.
- [64] Song GL, Atrens A. Corrosion Mechanisms of Magnesium Alloys. *Adv Eng Mater* 1999;1:11-33.
- [65] Jones DA. *Principles and prevention of corrosion*: Prentice Hall; 1996.
- [66] Song GL. Corrosion electrochemistry of magnesium and its alloys. In: Song GL, editor. *Corrosion of magnesium alloys*. Cambridge, UK: Woodhead Publishing Limited; 2011.
- [67] Baker H, Avedesian MM. *Magnesium and magnesium alloys* /edited by M. Avedesian and Hugh Baker. Materials Park, OH :ASM International; 1999.
- [68] Kirkland NT. Magnesium biomaterials: past, present and future. *Corrosion Engineering, Science and Technology* 2012;47:322-8.
- [69] Song G, Atrens A, Stjohn D, Nairn J, Li Y. The electrochemical corrosion of pure magnesium in 1 N NaCl. *Corros Sci* 1997;39:855-75.
- [70] Zainal Abidin NI, Atrens AD, Martin D, Atrens A. Corrosion of high purity Mg, Mg2Zn0.2Mn, ZE41 and AZ91 in Hank's solution at 37 °C. *Corros Sci* 2011;53:3542-56.
- [71] Kirkland NT, Birbilis N, Staiger MP. Assessing the corrosion of biodegradable magnesium implants: A critical review of current methodologies and their limitations. *Acta Biomaterialia* 2012;8:925-36.
- [72] Singh Raman RK, Birbilis N, Efthimiadis J. Corrosion of Mg alloy AZ91 - the role of microstructure. *Corrosion Engineering, Science and Technology* 2004;39:346-50.
- [73] Blawert C, Fechner D, Hoche D, Heitmann V, Dietzel W, Kainer KU, Zivanovic P, Scharf C, Ditzel A, Grobner J, Schmid-Fetzer R. Magnesium secondary alloys: Alloy design for magnesium alloys with improved tolerance limits against impurities. *Corros Sci* 2010;52:2452-68.
- [74] Song G. Recent Progress in Corrosion and Protection of Magnesium Alloys. *Adv Eng Mater* 2005;7:563-86.

- [75] Yuen CK, Ip WY. Theoretical risk assessment of magnesium alloys as degradable biomedical implants. *Acta Biomaterialia* 2010;6:1808-12.
- [76] Ma E, Xu J. Biodegradable Alloys: The glass window of opportunities. *Nat Mater* 2009;8:855-7.
- [77] Atrens A, Liu M, Zainal Abidin NI. Corrosion mechanism applicable to biodegradable magnesium implants. *Mater Sci Eng, B* 2011;176:1609-36.
- [78] Williams D. New Interests in Magnesium. *Medical Device Technology* 2006;17:9-10.
- [79] Bobby Kannan M, Singh Raman RK. Evaluating the stress corrosion cracking susceptibility of Mg-Al-Zn alloy in modified-simulated body fluid for orthopaedic implant application. *Scripta Mater* 2008;59:175-8.
- [80] Perrault GG. Encyclopedia of Electrochemistry of the Elements. In: Bard AJ, editor. New York: Marcel Dekker; 1978.
- [81] Pourbaix M. Atlas of electrochemical equilibria in aqueous solutions: National Association of Corrosion Engineers; 1974.
- [82] Perrault GG. The potential-pH diagram of the magnesium-water system. *Journal of Electroanalytical Chemistry and Interfacial Electrochemistry* 1974;51:107-19.
- [83] Song G, Atrens A, John DS, Wu X, Nairn J. The anodic dissolution of magnesium in chloride and sulphate solutions. *Corros Sci* 1997;39:1981-2004.
- [84] Atrens A, Dietzel W. The Negative Difference Effect and Unipositive Mg<sup>+</sup>. *Adv Eng Mater* 2007;9:292-7.
- [85] Petty RL, Davidson AW, Kleinberg J. The anodic oxidation of magnesium metal: Evidence for the existence of unipositive magnesium. *JACS* 1954;76:363-6.
- [86] Przyluski J, Palka E. Investigation of the kinetics of the anodic oxidation of the magnesium in an ammonium chloride solution. *Electrochim Acta* 1970;15:853-64.
- [87] Williams G, Neil McMurray H. Localized Corrosion of Magnesium in Chloride-Containing Electrolyte Studied by a Scanning Vibrating Electrode Technique. *J Electrochem Soc* 2008;155:C340-C9.
- [88] Åswiątowska J, Volovitch P, Ogle K. The anodic dissolution of Mg in NaCl and Na<sub>2</sub>SO<sub>4</sub> electrolytes by atomic emission spectroelectrochemistry. *Corros Sci* 2010;52:2372-8.
- [89] Tunold R, Holtan H, Berge M-BHg, Lasson A, Steen-Hansen R. The corrosion of magnesium in aqueous solution containing chloride ions. *Corros Sci* 1977;17:353-65.
- [90] Petrova LM, Krasnoyarskii VV. Dissolution mechanisms for magnesium-lithium anodes in natural aqueous media Protection of Metals (English translation of Zashchita Metallov) 1987;23:342-4.
- [91] Makar GL, Kruger J. Corrosion studies of rapidly solidified magnesium alloys. *J Electrochem Soc* 1990;137:414-21.
- [92] Kirkland NT, Williams G, Birbilis N. Observations of the galvanostatic dissolution of pure magnesium. *Corros Sci* 2012;65:5-9.
- [93] Perrault GG. Potentiostatic study of the magnesium electrode in aqueous solution. *Journal of Electroanalytical Chemistry and Interfacial Electrochemistry* 1970;27:47-58.
- [94] Fontana MG. Corrosion engineering: McGraw-Hill; 1986.

- [95] Xu L, Zhang E, Yin D, Zeng S, Yang K. In vitro corrosion behaviour of Mg alloys in a phosphate buffered solution for bone implant application. *Journal of Materials Science: Materials in Medicine* 2008;19:1017-25.
- [96] Xu L, Yu G, Zhang E, Pan F, Yang K. In vivo corrosion behavior of Mg-Mn-Zn alloy for bone implant application. *Journal of Biomedical Materials Research Part A* 2007;83A:703-11.
- [97] Singh Raman R. The role of microstructure in localized corrosion of magnesium alloys. *Metall Trans A* 2004;35:2525-31.
- [98] Zhou W, Shen T, Aung NN. Effect of heat treatment on corrosion behaviour of magnesium alloy AZ91D in simulated body fluid. *Corros Sci* 2010;52:1035-41.
- [99] Zhang E, Yang L. Microstructure, mechanical properties and bio-corrosion properties of Mg-Zn-Mn-Ca alloy for biomedical application. *Mater Sci Eng, A* 2008;497:111-8.
- [100] Fischerauer SF, Kraus T, Wu X, Tangl S, Sorantin E, Hanzi AC, Löffler JF, Uggowitzer PJ, Weinberg AM. In vivo degradation performance of micro-arc-oxidized magnesium implants: A micro-CT study in rats. *Acta Biomaterialia* 2012.
- [101] Jones RH. Stress-corrosion cracking: ASM International; 1992.
- [102] Sieradzki K, Newman RC. Brittle behavior of ductile metals during stress-corrosion cracking. *Philos Mag A* 1985;51:95-132.
- [103] Parkins RN. Predictive approaches to stress corrosion cracking failure. *Corros Sci* 1980;20:147-66.
- [104] Winzer N, Atrens A, Dietzel W, Song G, Kainer KU. Comparison of the linearly increasing stress test and the constant extension rate test in the evaluation of transgranular stress corrosion cracking of magnesium. *Mater Sci Eng, A* 2008;472:97-106.
- [105] Winzer N, Atrens A, Dietzel W, Raja VS, Song G, Kainer KU. Characterisation of stress corrosion cracking (SCC) of Mg-Al alloys. *Mater Sci Eng, A* 2008;488:339-51.
- [106] Bala Srinivasan P, Liang J, Blawert C, Dietzel W. Environmentally assisted cracking behaviour of plasma electrolytic oxidation coated AZ31 magnesium alloy. *Corrosion Engineering, Science and Technology* 2011;46:706-11.
- [107] Bobby Kannan M, Dietzel W, Raman RKS, Lyon P. Hydrogen-induced-cracking in magnesium alloy under cathodic polarization. *Scripta Mater* 2007;57:579-81.
- [108] Bobby Kannan M, Dietzel W. Pitting-induced hydrogen embrittlement of magnesium-aluminium alloy. *Materials & Design* 2012;42:321-6.
- [109] Kannan MB, Dietzel W, Blawert C, Riekehr S, Koçak M. Stress corrosion cracking behavior of Nd:YAG laser butt welded AZ31 Mg sheet. *Mater Sci Eng, A* 2007;444:220-6.
- [110] Dietzel W, Pfuff M, Winzer N. Testing and mesoscale modelling of hydrogen assisted cracking of magnesium. *Engineering Fracture Mechanics* 2010;77:257-63.
- [111] Winzer N, Atrens A, Dietzel W, Song G, Kainer KU. Fractography of Stress Corrosion Cracking of Mg-Al Alloys. *Metall Trans A* 2008;39:1157-73.
- [112] Chen J, Ai M, Wang J, Han E-H, Ke W. Stress corrosion cracking behaviors of AZ91 magnesium alloy in deicer solutions using constant load. *Mater Sci Eng, A* 2009;515:79-84.
- [113] Ebtehaj K, Hardie D, Parkins RN. The influence of chloride-chromate solution composition on the stress corrosion cracking of a Mg-Al alloy. *Corros Sci* 1988;28:811-21.
- [114] Fairman L, Bray HJ. Transgranular see in Mg-Al alloys. *Corros Sci* 1971;11:533-41.

- [115] Lynch SP, Trevena P. Stress Corrosion Cracking and Liquid Metal Embrittlement in Pure Magnesium. *Corrosion* 1988;44:113-24.
- [116] Meletis EI, Hochman RF. Crystallography of Stress Corrosion Cracking in Pure Magnesium. *Corrosion* 1984;40:39-45.
- [117] Makar GL, Kruger J, Sieradzki K. Stress corrosion cracking of rapidly solidified magnesium-aluminum alloys. *Corros Sci* 1993;34:1311-42.
- [118] Uematsu Y, Kakiuchi T, Nakajima M. Stress corrosion cracking behavior of the wrought magnesium alloy AZ31 under controlled cathodic potentials. *Mater Sci Eng, A* 2012;531:171-7.
- [119] H. Uchida MY, S. Hanaki, T. Nozaki. Stress corrosion cracking of magnesium alloy with slow strain rate technique. *Chemistry, mechanics, and mechanisms*;1:323-32.
- [120] Srinivasan PB, Blawert C, Dietzel W, Kainer KU. Stress corrosion cracking behaviour of a surface-modified magnesium alloy. *Scripta Mater* 2008;59:43-6.
- [121] Miller WK. Stress corrosion cracking: Materials Performance and Evaluation, ASM International, USA; 1992. p. 251.
- [122] Perryman ECW. Stress-corrosion of magnesium alloys. *Journal of Institute of Metals* 1951; 78:621-42
- [123] Timonova MA. Intercrystalline corrosion and corrosion of metals under stress. Great Britain: Consultants Bureau; 1962.
- [124] Singh Raman RK, Rihan R, Ibrahim RN. A novel approach to the determination of the threshold for stress corrosion cracking ( $K_{ISCC}$ ) using round tensile specimens. *Metall Trans A* 2006;37:2963-73.
- [125] Dietzel W, Srinivasan PB, Atrens A. Testing and evaluation methods for stress corrosion cracking (SSC) in metals. In: Raja VS, Shoji T, editors. *Stress corrosion cracking: Theory and practice*, Cambridge: Woodhead Publishing Limited; 2011.
- [126] Ugiansky GM, Payer JH. *Stress Corrosion Cracking: The Slow Strain-Rate Technique*: American Society for Testing & Materials; 1979.
- [127] Singh Raman R. Evaluation of caustic embrittlement susceptibility of steels by slow strain rate testing. *Metall Trans A* 2005;36:1817-23.
- [128] Wearmouth WR, Dean GP, Parkins RN. Role of stress in the stress corrosion cracking of a Mg-Al Alloy. *Corrosion* 1973;29:251-8.
- [129] Singh Raman RK, Pal S. A Simple Approach to the Determination of Threshold Stress Intensity for Stress Corrosion Cracking ( $K_{ISCC}$ ) and Crack Growth of Sensitized Austenitic Stainless Steel. *Metall Trans A* 2011;42:2643-51.
- [130] Rihan R, Raman RKS, Ibrahim RN. Circumferential notched tensile (CNT) testing of cast iron for determination of threshold ( $K_{ISCC}$ ) for caustic crack propagation. *Mater Sci Eng, A* 2005;407:207-12.
- [131] Ibrahim RN, Rihan R, Raman RKS. Validity of a new fracture mechanics technique for the determination of the threshold stress intensity factor for stress corrosion cracking ( $K_{ISCC}$ ) and crack growth rate of engineering materials. *Engineering Fracture Mechanics* 2008;75:1623-34.
- [132] Pal S, Ibrahim RN, Singh Raman RK. Threshold stress intensity factor and crack growth rate for stress corrosion cracking of simulated heat affected zone in caustic solution. *Engineering Fracture Mechanics* 2011;78:13-26.

- [133] Pal S, Singh Raman RK. Determination of threshold stress intensity for chloride stress corrosion cracking of solution-annealed and sensitized austenitic stainless steel by circumferential notch tensile technique. *Corros Sci* 2010;52:1985-91.
- [134] Pal S, Ibrahim RN. Role of Bayer solution concentration and temperature in stress corrosion cracking susceptibility of steel. *Corros Sci* 2012;53:2660-9.
- [135] Singh Raman RK, Pal S. Investigations using smooth and notched specimens into validity of caustic cracking susceptibility diagram. *Metall Mater Trans A* 2010;41:2328-36.
- [136] R.N.Ibrahim, H.L.Stark. Validity requirements for fracture toughness measurements obtained from small circumferentially notched cylindrical specimens. *Engineering Fracture Mechanics* 1987;28:455-60.
- [137] H.L.Stark, R.N.Ibrahim. Crack propagation in aluminium gas cylinder neck material at constant load and room temperature. *Engineering Fracture Mechanics* 1992;41:569-75.
- [138] R.N. Ibrahim, A.Kotousov. Eccentricity correction for the evaluation of fracture toughness from cylindrical notched test small specimens. *Engineering Fracture Mechanics* 1999;64:49-58.
- [139] Pal S. Role of microstructure and environment in stress corrosion cracking susceptibility, PhD thesis: Monash University; 2010.
- [140] Chakrapani D, Pugh E. The transgranular SCC of a Mg-Al alloy: Crystallographic, fractographic and acoustic-emission studies. *Metall Trans A* 1975;6:1155-63.
- [141] Chakrapani DG, Pugh EN. Hydrogen embrittlement in a Mg-Al alloy. *Metall Trans A* 1976;7:173-8.
- [142] Gangloff RP. 6.02 - Hydrogen-assisted Cracking. In: Milne I, Ritchie RO, Karihaloo B, editors. *Comprehensive Structural Integrity*. Oxford: Pergamon; 2003. p. 31-101.
- [143] Chen J, Wang J, Han E, Ke W. Effect of hydrogen on stress corrosion cracking of magnesium alloy in 0.1 M Na<sub>2</sub>SO<sub>4</sub> solution. *Mater Sci Eng, A* 2008;488:428-34.
- [144] McCormack BAO, Walsh CD, Wilson SP, Prendergast PJ. A statistical analysis of microcrack accumulation in PMMA under fatigue loading: applications to orthopaedic implant fixation. *Int J Fatigue* 1998;20:581-93.
- [145] Sivakumar M, Kamachi Mudali U, Rajeswari S. Investigation of failures in stainless steel orthopaedic implant devices: fatigue failure due to improper fixation of a compression bone plate. *J Mater Sci Lett* 1994;13:142-5.
- [146] Yokoyama Ki, Ichikawa T, Murakami H, Miyamoto Y, Asaoka K. Fracture mechanisms of retrieved titanium screw thread in dental implant. *Biomaterials* 2002;23:2459-65.
- [147] Kononen MHO, Lavonius ET, Kivilahti JK. SEM observations on stress corrosion cracking of commercially pure titanium in a topical fluoride solution. *Dent Mater* 1995;11:269-72.
- [148] Bundy KJ, Vogelbaum MA, Desai VH. The influence of static stress on the corrosion behavior of 316L stainless steel in Ringer's solution. *Journal of Biomedical Materials Research* 1986;20:493-505.
- [149] Bundy KJ, Marek M, Hochman RF. In vivo and in vitro studies of the stress-corrosion cracking behavior of surgical implant alloys. *Journal of Biomedical Materials Research* 1983;17:467-87.
- [150] Gray-Munro JE, Seguin C, Strong M. Influence of surface modification on the in vitro corrosion rate of magnesium alloy AZ31. *Journal of Biomedical Materials Research Part A* 2009;91A:221-30.

- [151] Liu GY, Hu J, Ding ZK, Wang C. Bioactive calcium phosphate coating formed on micro-arc oxidized magnesium by chemical deposition. *Appl Surf Sci* 2011;257:2051-7.
- [152] Lei T, Ouyang C, Tang W, Li L-F, Zhou L-S. Enhanced corrosion protection of MgO coatings on magnesium alloy deposited by an anodic electrodeposition process. *Corros Sci* 2010;52:3504-8.
- [153] Gunde P, Hänzi AC, Sologubenko AS, Uggowitzer PJ. High-strength magnesium alloys for degradable implant applications. *Mater Sci Eng, A* 2010;528:1047-54.
- [154] Liu C, Xin Y, Tian X, Chu PK. Corrosion behavior of AZ91 magnesium alloy treated by plasma immersion ion implantation and deposition in artificial physiological fluids. *Thin Solid Films* 2007;516:422-7.
- [155] Tian XB, Wei CB, Yang SQ, Fu RKY, Chu PK. Corrosion resistance improvement of magnesium alloy using nitrogen plasma ion implantation. *Surf Coat Technol* 2005;198:454-8.
- [156] da Conceicao TF, Scharnagl N, Dietzel W, Hoeche D, Kainer KU. Study on the interface of PVDF coatings and HF-treated AZ31 magnesium alloy: Determination of interfacial interactions and reactions with self-healing properties. *Corros Sci* 2011;53:712-9.
- [157] Chen XB, Birbilis N, Abbott TB. A simple route towards a hydroxyapatite-Mg(OH)<sub>2</sub> conversion coating for magnesium. *Corros Sci* 2011 53:2263-8.
- [158] Yu BL, Pan XL, Uan JY. Enhancement of corrosion resistance of Mg-9 wt.% Al-1 wt.% Zn alloy by a calcite (CaCO<sub>3</sub>) conversion hard coating. *Corros Sci* 2010;52:1874-8.
- [159] Zhou W, Shan D, Han E-H, Ke W. Structure and formation mechanism of phosphate conversion coating on die-cast AZ91D magnesium alloy. *Corros Sci* 2008;50:329-37.
- [160] Ng WF, Wong MH, Cheng FT. Stearic acid coating on magnesium for enhancing corrosion resistance in Hanks' solution. *Surf Coat Technol* 2010;204:1823-30.
- [161] da Conceicao TF, Scharnagl N, Dietzel W, Kainer KU. Controlled degradation of a magnesium alloy in simulated body fluid using hydrofluoric acid treatment followed by polyacrylonitrile coating. *Corros Sci* 2012;62:83-9.
- [162] Zheng YF, Gu XN, Xi YL, Chai DL. In vitro degradation and cytotoxicity of Mg/Ca composites produced by powder metallurgy. *Acta Biomaterialia* 2010;6:1783-91.
- [163] Ye X, Chen M, Yang M, Wei J, Liu D. In vitro corrosion resistance and cytocompatibility of nano-hydroxyapatite reinforced Mg-Zn-Zr composites. *Journal of Materials Science: Materials in Medicine* 2010;21:1321-8.
- [164] Feng A, Han Y. The microstructure, mechanical and corrosion properties of calcium polyphosphate reinforced ZK60A magnesium alloy composites. *J Alloys Compd* 2010;504:585-93.
- [165] Guan YC, Zhou W, Zheng HY. Effect of laser surface melting on corrosion behaviour of AZ91D Mg alloy in simulated-modified body fluid. *J Appl Electrochem* 2009;39:1457-64.
- [166] Song Y, Zhang S, Li J, Zhao C, Zhang X. Electrodeposition of Ca-P coatings on biodegradable Mg alloy: In vitro biomineralization behavior. *Acta Biomaterialia* 2010;6:1736-42.
- [167] Choudhary L, Raman RKS, Nie JF. In Vitro Evaluation of Degradation of a Calcium Phosphate Coating on a Mg-Zn-Ca Alloy in a Physiological Environment. *Corrosion* 2012;68:499-506.
- [168] Narayanan R, Dutta S, Seshadri SK. Hydroxy apatite coatings on Ti-6Al-4V from seashell. *Surf Coat Technol* 2006;200:4720-30.

- [169] Hanawa T, Ota M. Calcium phosphate naturally formed on titanium in electrolyte solution. *Biomaterials* 1991;12:767-74.
- [170] Koutsoukos P, Amjad Z, Tomson MB, Nancollas GH. Crystallization of calcium phosphates. A constant composition study. *JACS* 1980;102:1553-7.
- [171] LeGeros RZ. Apatites in biological systems *Progress in Crystal Growth and Characterization* 1981;4:1-45.
- [172] Geim AK, Novoselov KS. The rise of graphene. *Nat Mater* 2007;6:183-91.
- [173] Stolyarova E, Stolyarov D, Bolotin K, Ryu S, Liu L, Rim KT, Klima M, Hybertsen M, Pogorelsky I, Pavlishin I, Kusche K, Hone J, Kim P, Stormer HL, Yakimenko V, Flynn G. Observation of Graphene Bubbles and Effective Mass Transport under Graphene Films. *Nano Lett* 2008;9:332-7.
- [174] Leenaerts O, Partoens B, Peeters FM. Water on graphene: Hydrophobicity and dipole moment using density functional theory. *Physical Review B* 2009;79:235440.
- [175] Kirkland NT, Schiller T, Medhekar N, Birbilis N. Exploring graphene as a corrosion protection barrier. *Corros Sci* 2012;56:1-4.
- [176] Singh Raman RK, Chakraborty Banerjee P, Lobo DE, Gullapalli H, Sumandasa M, Kumar A, Choudhary L, Tkacz R, Ajayan PM, Majumder M. Protecting copper from electrochemical degradation by graphene coating. *Carbon* 2012;50:4040-5.
- [177] Prasai D, Tuberquia JC, Harl RR, Jennings GK, Bolotin KI. Graphene: Corrosion-Inhibiting Coating. *ACS Nano* 2012;6:1102-8.
- [178] Kim S, Ku SH, Lim SY, Kim JH, Park CB. Graphene–Biomaterial Hybrid Materials. *Adv Mater* 2011;23:2009-14.
- [179] Kim S, Park CB. Bio-Inspired Synthesis of Minerals for Energy, Environment, and Medicinal Applications. *Adv Funct Mater* 2012;23:10-25.
- [180] Zatta P, Giordano R, Corain B, Bombi GG. Alzheimer dementia and the aluminum hypothesis. *Medical Hypotheses* 1988;26:139-42.
- [181] Hanzi AC, Sologubenko AS, Uggowitzer PJ. Design strategy for new biodegradable Mg–Y–Zn alloys for medical applications. *Int J Mater Res* 2009;100:1127–36.
- [182] Oyane A, Kim HM, Furuya T, Kokubo T, Miyazaki T, Nakamura T. Preparation and assessment of revised simulated body fluids. *Journal of Biomedical Materials Research Part A* 2003;65A:188-95.
- [183] Kokubo T, Kushitani H, Sakka S, Kitsugi T, Yamamuro T. Solutions able to reproduce in vivo surface-structure changes in bioactive glass-ceramic A-W3. *Journal of Biomedical Materials Research* 1990;24:721-34.
- [184] Ambat R, Aung NN, Zhou W. Studies on the influence of chloride ion and pH on the corrosion and electrochemical behaviour of AZ91D magnesium alloy. *J Appl Electrochem* 2000;30:865-74.
- [185] Liang J, Srinivasan PB, Blawert C, Dietzel W. Influence of chloride ion concentration on the electrochemical corrosion behaviour of plasma electrolytic oxidation coated AM50 magnesium alloy. *Electrochim Acta* 2010;55:6802-11.
- [186] Jalota S, Bhaduri SB, Tas AC. Using a synthetic body fluid (SBF) solution of 27 mM  $\text{HCO}_3^-$  to make bone substitutes more osteointegrative. *Mater Sci Eng, C* 2008;28:129-40.

- [187] Ibrahim RN, Stark HL. Validity requirements for fracture toughness measurements obtained from small circumferentially notched cylindrical specimens. *Engineering Fracture Mechanics* 1987;28:455-60.
- [188] Barsoukov E, Macdonald JR. *Impedance Spectroscopy: Theory, Experiment, and Applications* (second ed.): John Wiley & Sons Inc., Hoboken, New Jersey; 2005.
- [189] Lawson L, Chen EY, Meshii M. Near-threshold fatigue: a review. *Int J Fatigue* 1999;21:15-34.
- [190] James BA, Sire RA. Fatigue-life assessment and validation techniques for metallic vascular implants. *Biomaterials* 2010;31:181-6.
- [191] Singh Raman R, Rihan R, Ibrahim R. A novel approach to the determination of the threshold for stress corrosion cracking ( $K_{ISCC}$ ) using round tensile specimens. *Metall Trans A* 2006;37:2963-73.
- [192] T. Hassel F-WB, A. Golovko, C. Krause. Investigation of the mechanical properties and the corrosion behaviour of low alloyed magnesium-calcium alloys for use as absorbable biomaterial in the implant technique. *Magnesium Technology in the Global Age, 45th Annual Conference of Metallurgists of CIM*, Montreal, Quebec, Canada 2006. p. 359–70.
- [193] Shepelev D, Bamberger M, Katsman A. Precipitation hardening of Zr-modified Mg–Ca–Zn alloy. *Journal of Materials Science* 2009;44:5627-35.
- [194] Tong LB, Zheng MY, Xu SW, Kamado S, Du YZ, Hu XS, Wu K, Gan WM, Brokmeier HG, Wang GJ, Lv XY. Effect of Mn addition on microstructure, texture and mechanical properties of Mg–Zn–Ca alloy. *Mater Sci Eng, A* 2011;528:3741-7.
- [195] Crapper DR, Krishnan SS, Quittkat S. Aluminium, neurofibrillary degeneration and Alzheimer's disease. *Brain : a journal of neurology* 1976;99:67-80.
- [196] Erbel R, Di Mario C, Bartunek J, Bonnier J, de Bruyne B, Eberli FR, Erne P, Haude M, Heublein B, Horrigan M, Ilesley C, Böse D, Koolen J, Lüscher TF, Weissman N, Waksman R. Temporary scaffolding of coronary arteries with bioabsorbable magnesium stents: a prospective, non-randomised multicentre trial. *The Lancet* 2007;369:1869-75.
- [197] Hanzi AC, Dalla Torre FH, Sologubenko AS, Gunde P, Schmid-Fetzer R, Kuehlein M, Löffler JF, Uggowitzer PJ. Design strategy for microalloyed ultra-ductile magnesium alloys. *Philos Mag Lett* 2009;89:377-90.
- [198] Kaiser MM, Zachert G, Wendlandt R, Eggert R, Stratmann C, Gros N, Schulze-Hessing M, Rapp M. Increasing stability by pre-bending the nails in elastic stable intramedullary nailing: A biomechanical analysis of a synthetic femoral spiral fracture model. *Journal of Bone & Joint Surgery, British Volume* 2012;94-B:713-8.
- [199] Di Mario C, Griffiths HUW, Goktekin O, Peeters N, Verbist JAN, Bosiers M, Deloose K, Heublein B, Rohde R, Kasese V, Ilesley C, Erbel R. Drug-Eluting Bioabsorbable Magnesium Stent. *Journal of Interventional Cardiology* 2004;17:391-5.
- [200] Arrabal R, Matykina E, Viejo F, Skeldon P, Thompson GE. Corrosion resistance of WE43 and AZ91D magnesium alloys with phosphate PEO coatings. *Corros Sci* 2008;50:1744-52.
- [201] Koike J, Kobayashi T, Mukai T, Watanabe H, Suzuki M, Maruyama K, Higashi K. The activity of non-basal slip systems and dynamic recovery at room temperature in fine-grained AZ31B magnesium alloys. *Acta Mater* 2003;51:2055-65.
- [202] Baril G, Pébère N. The corrosion of pure magnesium in aerated and deaerated sodium sulphate solutions. *Corros Sci* 2001;43:471-84.



- [203] Best SM, Porter AE, Thian ES, Huang J. Bioceramics: Past, present and for the future. *J Eur Ceram Soc* 2008;28:1319-27.
- [204] Kim S, Park CB. Dopamine-Induced Mineralization of Calcium Carbonate Vaterite Microspheres. *Langmuir* 2010;26:14730-6.
- [205] Geim AK. Graphene: Status and Prospects. *Science* 2009;324:1530-4.
- [206] Nayak TR, Andersen H, Makam VS, Khaw C, Bae S, Xu X, Ee P-LR, Ahn J-H, Hong BH, Pastorin G, Azyilmaz B. Graphene for Controlled and Accelerated Osteogenic Differentiation of Human Mesenchymal Stem Cells. *ACS Nano* 2011;5:4670-8.
- [207] Novoselov KS, Geim AK, Morozov SV, Jiang D, Zhang Y, Dubonos SV, Grigorieva IV, Firsov AA. Electric Field Effect in Atomically Thin Carbon Films. *Science* 2004;306:666-9.
- [208] Stankovich S, Dikin DA, Dommett GHB, Kohlhaas KM, Zimney EJ, Stach EA, Piner RD, Nguyen ST, Ruoff RS. Graphene-based composite materials. *Nature* 2006;442:282-6.
- [209] Gal J-Y, Bollinger J-C, Tolosa H, Gache N. Calcium carbonate solubility: a reappraisal of scale formation and inhibition. *Talanta* 1996;43:1497-509.
- [210] Maeda H, Kasuga T, Nogami M. Apatite formation on titania-vaterite powders in simulated body fluid. *J Eur Ceram Soc* 2004;24:2125-30.
- [211] Kim S, Park CB. Mussel-inspired transformation of  $\text{CaCO}_3$  to bone minerals. *Biomaterials* 2010;31:6628-34.
- [212] Ryu J, Ku SH, Lee H, Park CB. Mussel-Inspired Polydopamine Coating as a Universal Route to Hydroxyapatite Crystallization. *Adv Funct Mater* 2010;20:2132-9.
- [213] Hummers WS, Offeman RE. Preparation of Graphitic Oxide. *JACS* 1958;80:1339-.
- [214] Xu Y, Bai H, Lu G, Li C, Shi G. Flexible Graphene Films via the Filtration of Water-Soluble Noncovalent Functionalized Graphene Sheets. *JACS* 2008;130:5856-7.
- [215] Neil WC, Forsyth M, Howlett PC, Hutchinson CR, Hinton BRW. Corrosion of magnesium alloy ZE41 - The role of microstructural features. *Corros Sci* 2009;51:387-94.
- [216] Mann S. *Biom mineralization: Principles and Concepts in Bioinorganic Materials Chemistry*: Oxford University Press; 2001.
- [217] Li W, Gao C. Efficiently Stabilized Spherical Vaterite  $\text{CaCO}_3$  Crystals by Carbon Nanotubes in Biomimetic Mineralization. *Langmuir* 2007;23:4575-82.
- [218] Gao W, Alemany LB, Ci L, Ajayan PM. New insights into the structure and reduction of graphite oxide. *Nat Chem* 2009;1:403-8.
- [219] Park S, Ruoff RS. Chemical methods for the production of graphenes. *Nat Nano* 2009;4:217-24.
- [220] Ferrari AC, Meyer JC, Scardaci V, Casiraghi C, Lazzeri M, Mauri F, Piscanec S, Jiang D, Novoselov KS, Roth S, Geim AK. Raman Spectrum of Graphene and Graphene Layers. *Phys Rev Lett* 2006;97:187401.
- [221] Ooi J WJv, Zhu D. Electrochemical impedance spectroscopy of Bis-[Triethoxysilylpropyl] Tetrasulfide on Al 2024-T3 substrates. *Corrosion* 2001;57:413.
- [222] Chakraborty Banerjee P, Singh Raman RK. Electrochemical impedance spectroscopic investigation of the role of alkaline pre-treatment in corrosion resistance of a silane coating on magnesium alloy, ZE41. *Electrochim Acta* 2011;56:3790-8.

- [223] Montemor MF, Ferreira MGS. Electrochemical study of modified bis-[triethoxysilylpropyl] tetrasulfide silane films applied on the AZ31 Mg alloy. *Electrochim Acta* 2007;52:7486-95.
- [224] Palomino LEM, Suegama PH, Aoki IV, Pászti Z, de Melo HG. Investigation of the corrosion behaviour of a bilayer cerium-silane pre-treatment on Al 2024-T3 in 0.1 M NaCl. *Electrochim Acta* 2007;52:7496-505.
- [225] Palomino LM, Suegama PH, Aoki IV, Montemor MF, De Melo HG. Electrochemical study of modified cerium-silane bi-layer on Al alloy 2024-T3. *Corros Sci* 2009;51:1238-50.
- [226] Suchanek WL, Shuk P, Byrappa K, Riman RE, TenHuisen KS, Janas VF. Mechanochemical - hydrothermal synthesis of carbonated apatite powders at room temperature. *Biomaterials* 2002;23:699-710.